

Structural and Climatic Effects of Large-Scale Basaltic Magmatism:
Constraints and Insights from Geodynamic Models

Xiaochuan Tian

Submitted in partial fulfillment of the
requirements for the degree of
Doctor of Philosophy
under the Executive Committee
of the Graduate School of Arts and Sciences

COLUMBIA UNIVERSITY

2021

© 2021

Xiaochuan Tian

All Rights Reserve

Abstract

Structural and Climatic Effects of Large-Scale Basaltic Magmatism:

Constraints and Insights from Geodynamic Models

Xiaochuan Tian

This thesis concerns the causes and consequences of magma emplacement in the Earth's lithosphere during the formation of Large Igneous Provinces (LIPs) and continental rifts. Motivated by geological, geophysical, geochemical and paleoclimate data, I formulate geodynamic models to address the following questions: (1) How were the massive volumes of subaerially erupted lava, described in multi-channel seismic data as seaward-dipping reflectors (SDRs), formed and what can SDRs tell us about the rifting processes? (2) What thermal and rheological conditions are required to produce the contrast in topography of the two youngest LIPs: namely that the Columbia Plateau sits ~0.7 km lower than the surrounding region while the Ethiopian Plateau is ~1.5 km higher than its surroundings? (3) Why does significant global warming occur a few hundred-thousand years prior to the main phase of eruptions of the Columbia River Basalts and the Deccan Traps? The major results of my thesis are: (1) The first two-dimensional thermo-mechanical treatment of SDR formation shows how the lithosphere thickness affects the deformation in response to magmatic loads during volcanic margin formation. I provide a quantitative mapping between the shape of SDRs and the strength of the lithosphere and this mapping reveals weak continental margin lithosphere during the initial continental breakup. (2) Cold and strong crust results in slow lower crustal flow and a persistent high plateau like the Ethiopian Plateau. In contrast, a combination of three things can produce a low plateau like the Columbia Plateau. First, hot and weak lower crust that flows fast in response to topographic and magmatic loads. Second, a significant fraction of the magma intruded in the

crust freezes onto and becomes part of the strong upper crust. Finally, the bulk of the intrusions occur before the main phase of extrusion to explain the geometry of the Columbia River Basalt lava flows. (3) I argue that the major eruptions of continental flood basalts may require densification of the crust by intrusion of larger volumes of magma than are extruded. Simple models show that magma crystallization and release of CO₂ from such intrusions could produce global warming before the main phase of flood basalt eruptions on the observed timescale

Table of Contents

Acknowledgments	iv
Dedication	v
Preface.....	1
Chapter 1: Lithospheric Thickness of Volcanic Rifting Margins: Constraints from Seaward Dipping Reflectors	5
1.1 Introduction.....	6
1.2 Models and Results	12
1.2.1 Review of Analytic elastic thin plate (ATP) model and its linkage to SDRs observations	13
1.2.2 Numerical elastic thin plate model (NTP)	15
1.2.3 Two Dimensional Numerical Models.....	16
1.2.3.1 Numerical Convergence of Elastic and Elastic Plastic thick plate cases.....	17
1.2.3.2 Elastic-Plastic (EP) thick plate with long-term plate extension.....	18
1.2.3.3 Elasto-visco-plastic (EVP) thick plate with constant thermal structure	21
1.2.3.4 Elasto-visco-plastic thick plate with thermal evolution.....	24
1.3 Analysis of data.....	30
1.4 Discussion and Conclusions	31
Acknowledgments.....	34
References:.....	34
Appendix 1:.....	40
A1-1 Review of Analytic elastic thin plate model and its linkage to SDRs observations....	40
A1-2. Numerical Thin plate (NTP) description	45

A1-3. Tracer implementation in FLAC	49
A1-4. Benchmark between FLAC models and NTP models	50
A1-5. The published MCS profiles used for calculating the Te based on the SDRs geometries	53
A1-References:	54
Chapter 2: How Intrusion and Crustal Flow Control the Topography of Continental Large Igneous Provinces.....	56
2.1 Introduction.....	57
2.2 Models and Results:.....	60
2.2.1 Schematic model.....	61
2.2.2 Semi-analytic model	63
2.2.3 Two-dimensional thermo-mechanical model	69
2.3 Discussion and Conclusions	80
References:.....	85
Chapter 3: Intrusion Induced Global Warming Preceding Continental Flood Basalt Volcanism.....	89
3.1 Main Text.....	90
References:.....	102
Appendix 3: Methods.....	105
A3-1. Common Model Features	106
A3-2. LOSCAR climate model.....	108
A3-3. Analytic sill intrusion model	109

A3-4. Multi-sill intrusion model.....	112
Appendix 3 References:	121

Acknowledgments

This thesis is not possible without the support of my advisors and friends.

I am very grateful to my PhD thesis advisor Roger Buck. It has been a long and tough journey. For a few times, I almost gave up but Roger never gave up on me. With his great patience and good will, I am finally here, starting to appreciate the beauty of simplicity in Geodynamic modeling. I also want to thank Suzanne Carbotte and Marc Spiegelman for their encouragements and advice throughout every milestone of this thesis. Bill Ryan's daily presence at Lamont with his kind words and actions demonstrate to me what a great scientist is like. I owe a debt of gratitude to my master's thesis advisor Eunseo Choi who has introduced me to this fascinating field of study and has been encouraging me and giving me advice for half a decade.

Thank you to my peers and friends. I appreciate Nick Frearson's help for reviving the Ping Pong table at Lamont and Ching-Yao Lai for playing with me. I hope to thank Elizabeth Fischer's great help and encouragements during my toughest final year. I also want to thank Bar Oryan for being a great officemate who has organized my favorite field trip to Peru. Thanks must also go to Josh Russell who has been the best roommate for me for three years in NYC. Josh never complains about me but always brings me laughter and helps me prepare all my important presentations. Mr. Tom Tarduongo has revived my genuine good will as an Earth science researcher through his genuine kindness and great ability to communicate. I am especially grateful to Doyeon Park, who has been a great mentor, guiding and encouraging me to evolve and bring goodness to the world.

My mother has brought me to the world and reared me up by herself with unconditional love. I dedicate this thesis to my mother.

Dedication

To my mother.

Preface

Large igneous provinces (LIPs) form when voluminous magma ($\sim 10^6 \text{ km}^3$) is emplaced as crustal intrusions and lava flows within a relatively short time ($<\sim 1 \text{ Myrs}$) ^{1,2}. Their formation contributes to the initiation of continental rifting ^{3,4} and closely correlate with climatic excursions and mass extinctions ^{5–7}. LIPs span the Earth’s Phanerozoic history and are of global significance ⁸, shaping a great portion of the Earth’s surface topography and near-surface structures of nearly every continent and ocean by adding voluminous basaltic rocks either as flood basalt lava flows onto continental and oceanic regions or as mafic intrusions within the crust. Examples of continental flood basalt provinces include the Siberian plateau in Central Asia, the Deccan plateau in South Asia, the Ethiopian plateau in Africa, and the Columbia plateau in North America. There are basaltic oceanic plateaus including the Ontong Java plateau in the Pacific Ocean, the Rio Grande Rise in the Atlantic Ocean or the Kerguelen Plateau in the Indian ocean. Many rifted continental margins associated with subaerial LIPs are characterized by buried, but subaerially emplaced, massive volcanic lava flows seismically imaged as seaward dipping reflectors (SDRs) ⁹.

This thesis considers the tectonic and climatic effects of large-scale magma emplacement during the formation of LIPs using numerical geodynamic models. Chapter 1 investigates the causes of the structure of the subaerially emplaced “Seaward Dipping Reflector” packages that define volcanic rifted margins, which are possibly the most voluminous volcanic lava flows on the Earth. Chapter 2 studies how crustal magma intrusions and lower crustal flow affect the surface topography of continental LIPs. Inspired by insights gained from Chapter 2, Chapter 3 addresses the recent surprising data that significant global warming occurred prior to the main phase flood basalt eruptions.

In Chapter 1, I look at the effects of lithospheric strength on subaerial emplacement of flood basalt lava during the transition from continental rifting to seafloor spreading. The research question is: how were the massive volume of subaerially erupted lava (observed in offshore multi-channel seismic data as seaward-dipping reflectors (SDRs)) formed and what can SDRs tell about the rifting processes? A series of analytic to numerical models are formulated to provide quantitative mapping between SDR geometries and lithospheric strength at rifted margins during rifting. This mapping sheds light on mechanics of rift-to-drift processes by revealing the strength of lithosphere during rifting that resists separation of the plates. This chapter has been published in *Journal of Geophysical Research*.

In Chapter 2, I focus on effects of deeper crustal magma emplacement and try to address why the two most recent large igneous provinces, the Ethiopian and Columbian Plateaus, have contrasting topographies. A series of analytic and numerical models were formulated to simulate lower crustal flow as well as loading from sill intrusions during a LIP event. Model results indicate that the strong versus weak lower crusts may be responsible for the observed contrast. In addition, the model results also show that large-scale intrusion prior to flood basalt eruption may be responsible for the observed synchronicity of Columbia basin subsidence and Columbia River Basalt Group (CRBG) eruptions. This chapter is under preparation for submission to *Journal of Geophysical Research*.

In Chapter 3, I study the climatic effects of large-scale crustal magma emplacements. The insights and results from Chapter 2 prepare me to address the recent surprising observation that significant global warming might have happened hundreds of thousands of years prior to the main phase of Deccan Traps and Columbia River Basalts eruptions. These observations are not consistent with the general hypothesis that massive LIP volcanism causes global climate change.

Inspired by the results of Chapter 2, I formulate simple models that can reconcile the seeming inconsistency. I argue that large-scale flood basalt eruption on continents may require replacement and densification of the crust by a volume of crustal magma intrusion that is larger than eruptions. Models show how it may take several hundred-thousand years from initial intrusion to eventual flood basalt eruptions. The degassing of significant amounts of CO₂ from solidifying crustal intrusions into the atmosphere could have led to significant global warming. As global warming becomes one of the most urgent problems of the 21st century, understanding the drivers of past climate changes can improve quantitative projections of the future effects of anthropogenic CO₂. This chapter is under review at Nature Geoscience.

References:

1. Coffin, M. F. & Eldholm, O. Large igneous provinces: Crustal structure, dimensions, and external consequences. *Rev. Geophys.* **32**, 1 (1994).
2. Bryan, S. E. & Ferrari, L. Large igneous provinces and silicic large igneous provinces: Progress in our understanding over the last 25 years. *Geol. Soc. Am. Bull.* **125**, 1053–1078 (2013).
3. Buck, W. R. The role of magma in the development of the Afro-Arabian Rift System. *Geol. Soc. London, Spec. Publ.* **259**, 43–54 (2006).
4. Courtillot, V., Jaupart, C., Manighetti, I., Tapponnier, P. & Besse, J. On causal links between flood basalts and continental breakup. *Earth Planet. Sci. Lett.* **166**, 177–195 (1999).
5. Courtillot, V. E. & Renne, P. R. On the ages of flood basalt events. *Comptes Rendus Geosci.* **335**, 113–140 (2003).
6. Wignall, P. B. Large igneous provinces and mass extinctions. *Earth-Science Rev.* **53**, 1–33 (2001).
7. Jones, M. T., Jerram, D. A., Svensen, H. H. & Grove, C. The effects of large igneous provinces on the global carbon and sulphur cycles. *Palaeogeogr. Palaeoclimatol. Palaeoecol.* **441**, 4–21 (2016).

8. Bryan, S. E. & Ernst, R. E. Revised definition of Large Igneous Provinces (LIPs). *Earth-Science Rev.* **86**, 175–202 (2008).
9. Tian, X. & Buck, W. R. Lithospheric Thickness of Volcanic Rifting Margins: Constraints From Seaward Dipping Reflectors. *J. Geophys. Res. Solid Earth* **124**, 3254–3270 (2019).

Chapter 1: Lithospheric Thickness of Volcanic Rifting Margins:

Constraints from Seaward Dipping Reflectors*

Seaward Dipping Reflectors (SDRs) are large piles of seaward-thickening volcanic wedges imaged seismically along most rifted continental margins. Despite their global ubiquity, it is still debated whether the primary cause of SDR formation is tectonic faulting or magmatic loading. To study how SDRs might form we developed the first two-dimensional thermo-mechanical model that can account for both tectonics and magmatism development of SDRs during rifting. We focus here on the magmatic loading mechanism and show that the shape of SDRs may provide unprecedented constraints on lithospheric strength at volcanic rifting margins. For mapping SDRs geometries to lithospheric strength, a sequence of model lithospheric rheologies are treated, ranging from analytic thin elastic plates to numerical thick elasto-visco-plastic crust and mantle layers with temperature and stress dependent viscosity. We then analyzed multi-channel seismic depth-converted images of SDRs from Vøring and Argentinian rifted margins in terms of geometric parameters that can be compared to our model results. This results in estimates for the lithospheric thickness during rifting at the two margins of 3.4 and 5.7 km. The plate thickness correlates inversely with mantle potential temperature at these margins during rifting, as estimated by independent studies.

* This Chapter has been published in the following paper:
Tian, X., & Buck, W. R. (2019). Lithospheric thickness of volcanic rifting margins: Constraints from seaward dipping reflectors. *Journal of Geophysical Research: Solid Earth*, 124(4), 3254-3270.

1.1 Introduction

Mounting evidence indicates that intensive volcanism occurs during most continental breakup events and before seafloor spreading (Buiter & Torsvik, 2014; Courtillot et al., 1999; Hinz, 1981; Kendall et al., 2005). As voluminous as continental flood basalts, seaward dipping reflectors, or SDRs, are large igneous wedges emplaced at continent-ocean boundaries that are now buried under kilometers of post-rift sediments. They are seen in multi-channel seismic (MCS) reflection profiles as reflectors dipping seaward. Drilling indicates SDRs consist of thin layers of sediments interbedded within thicker layers of lava (Eldholm et al., 1995). SDR wedges generally feature down-dip thickening and their dip angle increases with depth (Jackson et al., 2000; Mutter et al., 1982; Paton et al., 2017)(Figure 1).

Globally SDRs appear to be several to tens of kilometers thick, up to hundreds of kilometers wide (across margin) and several thousand kilometers long (along margin)(McDermott et al., 2018).

Hinz, (1981) first presented a global compilation of MCS profiles with SDRs. Following him, many authors have reported observations of SDRs including along North Atlantic margins (e.g. Mutter et al., 1982; Planke & Eldholm, 1994), South Atlantic margins (e.g. Elliott et al., 2009; Franke et al., 2010; Gladczenko et al., 1998), Indian margins (e.g. Calvès et al., 2011), Australian margins (e.g. Direen & Crawford, 2003)) and Antarctica margins (e.g. Kalberg & Gohl, 2014; Kristoffersen et al., 2014)). Tilted lava packages on Iceland (Bodvarsson & Walker, 1964) and parts of the Deccan traps (Watts & Cox, 1989) are on-land SDRs analogues.

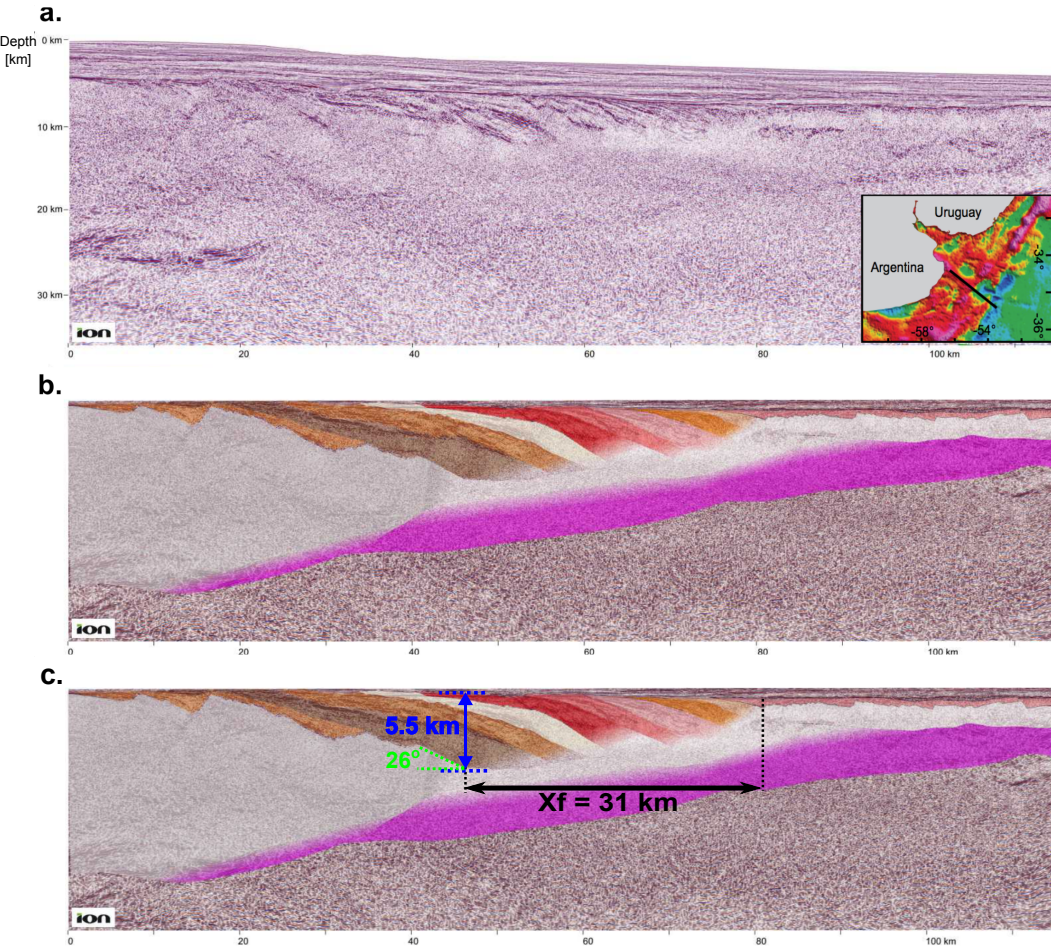


Figure 1: Multi-channel Seismic data of SDRs example off-shore Argentina at 55W, 35S (a and b from Paton *et al.*, 2017). a. Un-interpreted pre-stack depth migrated data image. b. from a, but with sediment layers removed and the SDRs surface flattened. Each SDR wedge is colored. c. marked version of panel b. X_f is 31 km and is the horizontal distance between the tip of the flat SDR and tip of the SDR that has the largest dip angle of 26 degree. The SDR wedges are 5.5 km thick.

There are two very different hypotheses for the formation of SDRs: tectonic faulting or magmatic loading. The major difference is how to make the accommodation space for infilling volcanic lava flows to form the SDRs. Many authors interpret SDRs as bounded by landward-dipping, large-offset normal faults with the downward deflection of the hanging wall producing the “accommodation space” for syn-tectonic volcanics (Becker *et al.*, 2016; Geoffroy, 2005; Gibson & Love, 1989; Pindell *et al.*, 2014; Planke *et al.*, 2000; Quirk *et al.*, 2014). Most on-land

regions with massive volcanic piles show little evidence of large offset normal faulting. Also, in most areas of continental and oceanic plate separation the normal faults dip ocean-ward. However, in an effort to numerically simulate SDR formation Geoffroy et al., (2015) produce landward dipping faults with a particular set of pre-existing weak zones, and not including effects of magma intrusion or lava infilling.

Magmatic loading to produce dipping lava beds was first proposed by Bodvarsson and Walker, (1964), who suggested that subsidence due to volcanic loading combined with crustal drift can explain the geometry of flow units on Iceland. Within the framework of plate tectonics, Palmason, (1973) proposed a kinematic model for crustal generation at Iceland assuming parabolic functions for describing the extension and subsidence velocities of lava piles. Paton et al., (2017) suggests variable SDR packages indicates changing magma supply. Buck, (2017) developed an analytical model of SDR formation assuming the elastic thin plate approximation for plate flexure due to the volcanic and magmatic loading. With reasonable values of flexural wavelength and dike height, the model produces SDRs that are shaped much like those observed (Figure 2&3). With either jumps in the axis of diking or oscillations in extrusion, the model can generate the kinds of multiple SDRs wedges sometimes observed (e.g. Becker et al., 2016).

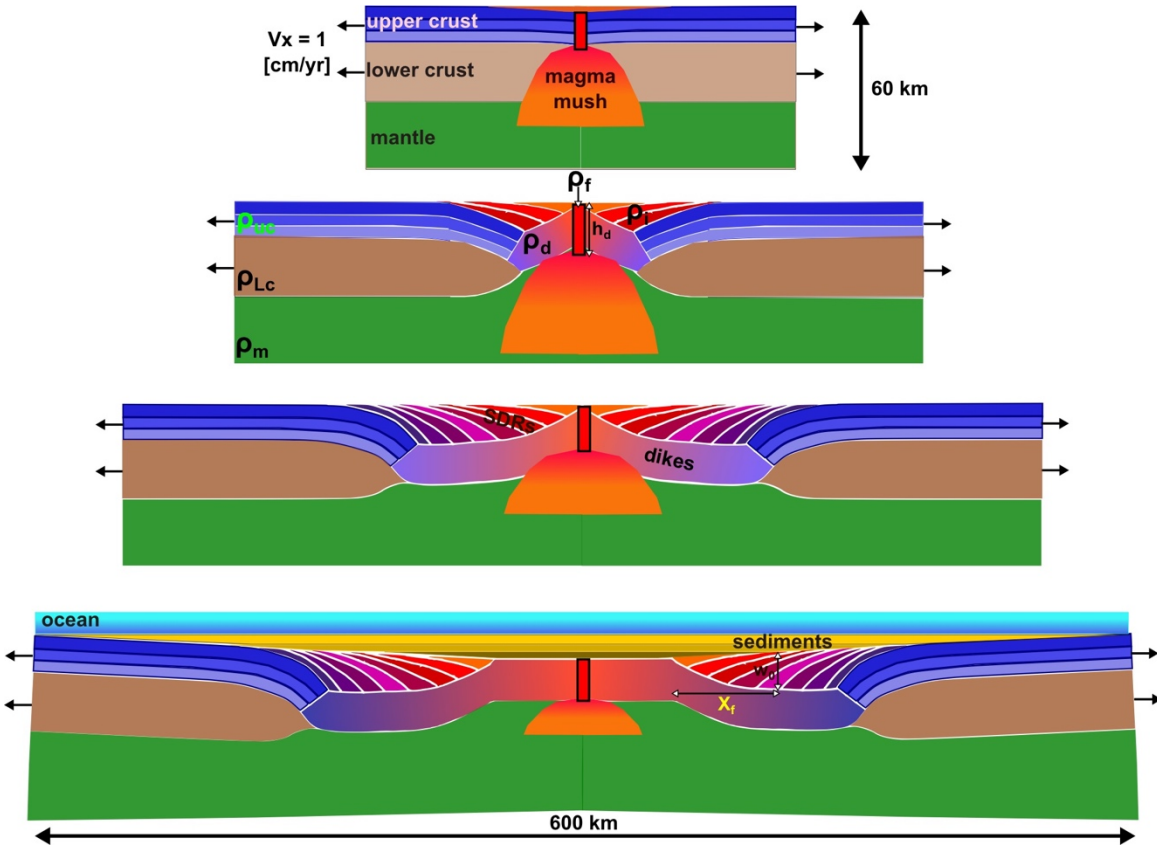


Figure 2. Cartoon illustration of SDRs formation processes. The SDRs geometries are extracted from results of 2D numerical models. The intrusion of magma as a dike in the top panel provides a load on the lithosphere as the dike solidifies and so increases in density. Volcanic flows fill in the region of subsidence driven by the dike load and further loads the lithosphere. The middle panel shows the effect of multiple cycles of dike intrusion, solidification and volcanic infill. The bottom panel shows how the volcanics eventually subside and are covered with sediment as more normal seafloor spreading occurs.

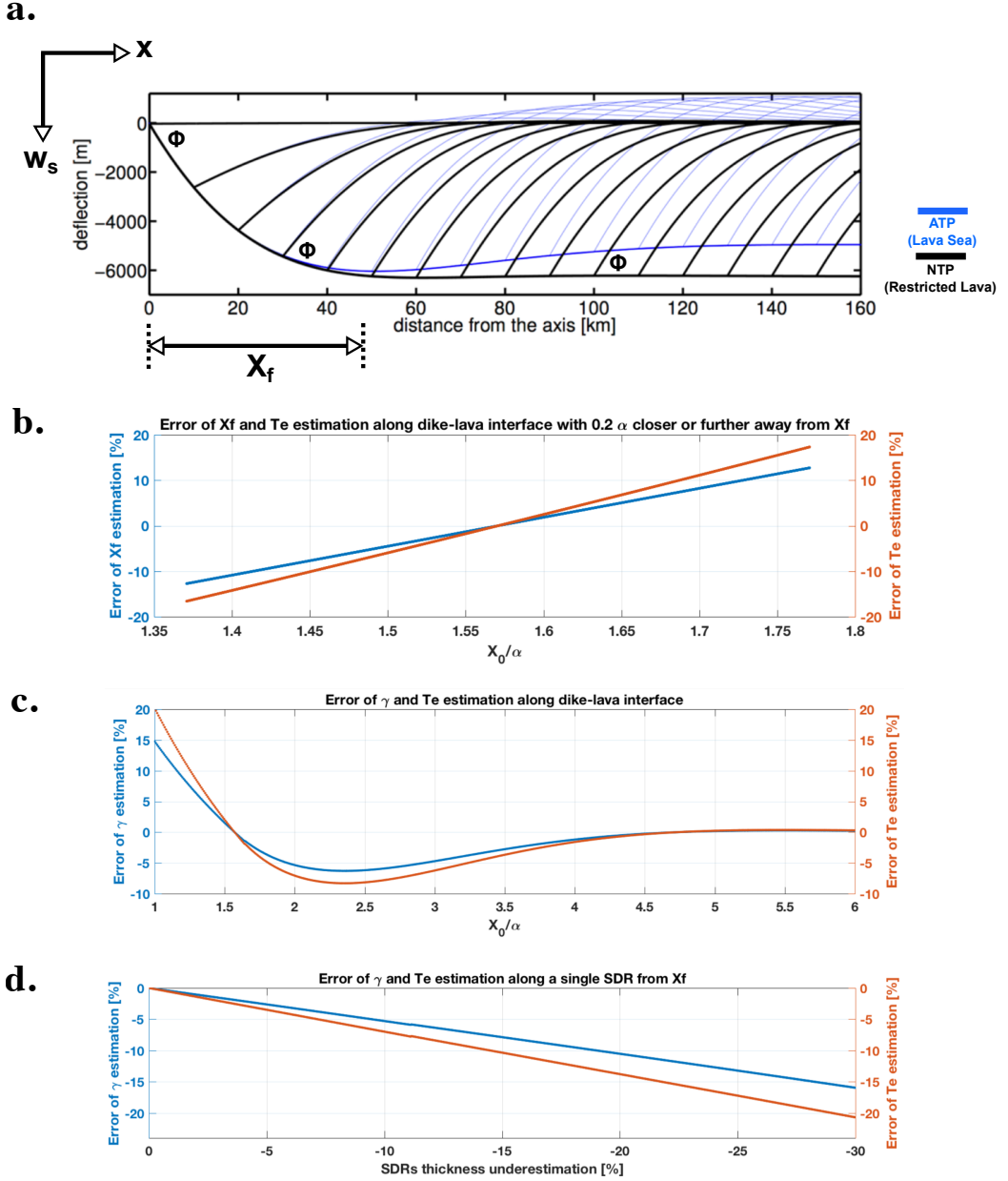


Figure 3. a. Direct comparison between ATP and NTP with $h_d = Te = 5 \text{ km}$. Blue lines are for ATP “lava sea” results. X_f is the horizontal distance between the tip of flat SDR and the SDR that has developed to a steady shape. ϕ is the angle between the tip of each SDR and the dike-lava interface. The vertical exaggeration is 7 to highlight the difference in the models. b. Analytic error estimation of X_f and Te if measuring along the dike-lava interface. c. analytic error estimation of γ and Te if measuring along the dike-lava interface. d. analytic error estimation if missing lower part of the SDR wedges.

The analytic model successfully explains many observations, yet it makes several simplifying approximations. To permit a closed form solution, it assumes the lava covers the

whole plate surface. However, lava flows should be restricted spatially to low lying regions adjacent to the spreading center. Morgan & Watts, (2018) model SDR formation by applying finite difference method (FDM) to solve the general thin plate flexure equation that allows spatial and temporal variability in plate strength and magmatic loading. They constrain their model results with seismic and gravity anomaly data and find that it requires a broken plate boundary condition and temporally decreasing effective elastic plate thickness to fit such observations. Both the analytic and the FDM models assume elastic thin plate and cannot consider the lithosphere as a thick plate composed of realistic materials with evolving density and thermal-mechanical structures.

Here, we develop two-dimensional numerical models to simulate SDRs formation in the context of continental rifting. The model formulation allows spatially varying lava infill (Abdelmalak et al., 2016), lower crustal underplating (Saikia et al., 2017; White et al., 2008) and elasto-visco-plastic rheology (Brace & Kohlstedt, 1980; Goetze & Poirier, 1978; Shelton & Tullis, 1981) both with and without thermal evolution.

Lithospheric strength at a rifting center is likely to exert a major control on the crustal structures formed during continental break up. It is also essential for determining whether or not a rift will succeed to seafloor spreading (e.g. Bialas et al., 2010; Buck, 2006). Common methods for studying lithospheric strength using gravity and topography data that gives current plate strength may not be accurate for plate boundaries during ancient rifting (e.g. Ebinger & Hayward, 1996; Pérez-Gussinyé et al., 2007) because those signals could have changed since rifting as the plate cools down and is loaded with post-rift sediments. However, as we will show, the shape of magmatic loading formed SDRs is a direct expression of the plate strength during rifting and should change little following their formation. Recent workers (McDermott et al.,

2018; Paton et al., 2017) argue that near-shore (or type 1) SDRs result from tectonic processes while off-shore (or type 2) SDRs are formed by magmatic processes. The numerical models we develop can treat both tectonic and magmatic processes, but here we focus on the effects of magmatic loading and leave the complexities of faulting for future investigations. The major goal of this study is to provide a mapping between the geometry of magmatic loading-controlled SDRs and lithospheric strength, or thickness, during their formation at volcanic rifted margins.

1.2 Models and Results

We build a sequence of models that begin with the simplest possible treatments for lithospheric response under magmatic loadings during the last stage of continental rifting, at which SDR forming transitions to seafloor spreading (Figure 2). We progressively reduce assumptions and show the effects of those changes, beginning with a brief description of an existing analytic model and culminating with a fully 2D thermal-mechanical model of volcanic margin evolution. This effort is divided into six steps: First, we review the analytic thin plate flexure formulation and describe how its prediction can be related to observations; Second, we apply finite difference methods to numerical thin plate (NTP) models with spatially restricted lava flow; Third, we show how 2D thick plate models converge with increasing numerical resolution and the results are compared with NTP models; Fourth, we develop long-term 2D numerical models with Elastic-Plastic (EP) rheology to quantify the effects of plasticity; Fifth, we use the long-term 2D numerical models with constant thermal structure to quantify the effects of Elasto-Visco-Plastic (EVP) rheology; Sixth, we describe fully models which the thermal evolution affect the strength of the lithosphere and show the effects of different crustal rheologies and amounts of underplating.

1.2.1 Review of Analytic elastic thin plate (ATP) model and its linkage to SDRs observations

According to a number of workers (e.g. Bodvarsson & Walker, 1964; Morgan & Watts, 2018; Watts & Cox, 1989) SDRs geometries are an expression of the flexural response of a lithosphere due to magmatic loads. An analytic description of the magma loading model, derived by Buck, (2017), depends on two length scales. The vertical scale is:

$$w_0 = h_d \frac{(\rho_d - \rho_f)}{(\rho_c - \rho_i)}$$

Where, h_d is the height of the dike, ρ_d is the density of the solidified dike, ρ_f is the density of the fluid magma filling the dike, ρ_c is the density of the compensating lower crustal or mantle material that flows in response to lateral load variations, and ρ_i is the density of the volcanic or sedimentary material infilling the depression produced by the load of the dike. The fluid magma filled dike is assumed to rise so that it is in local isostatic equilibrium. For simplicity, in the analytic model, the upper crust is taken to have an initial thickness of h_d and have the same density ρ_f as the fluid magma in the dike. This insures that the dike rises to the level of the initial top of the crust. The horizontal scale of bending of the model flows depends on the flexure parameter α , and for a thin elastic plate this is proportional to $Te^{3/4}$ where Te is the effective elastic plate thickness.

The analytic description of magmatic loading produces model geometries that are similar to real SDR packages. To relate real SDR geometry to the effective elastic thickness of this model we define three simple and potentially observable parameters. First, we define X_f as the horizontal distance between the tip of the last deposited lava infill and the first place where the dike-lava interface is flat (Figure 2, 3a). As derived in the Supplement this distance is $\pi\alpha / 2$. It may be difficult to accurately determine in data either the place of the last axis of diking before seafloor spreading or the place where the dike-lava interface becomes flat. Uncertainty in this

horizontal position of $\pm 0.2\alpha$ ($\pm 13\%$ of X_f) results in a T_e estimation error of less than 20% (Figure 3b).

We also consider the ratio γ between the thickness of the SDR and the slope of the flows intersecting with the dike-lava interface. As noted in the appendix this ratio varies slowly with distance from the axis of diking and equals $\alpha/2[1 + \exp(-\pi/2)]$ at a distance X_f away from the seaward tip of the last deposited SDR. Uncertainty in the horizontal position of X_f from α to 5α away from the tip of the flat SDR results in an estimation error of T_e ranges from +20% to -10% (Figure 3c). The effect of underestimating the depth to the base of the SDRs, due to difficulties in imaging the deeper SDRs, by 30% produces an underestimate of T_e of ~20% (Figure 3d). The last way of relating SDR geometry to model parameters is through the angle ϕ between the dike-flow interface and the intersecting flow (SDR) (see Figure 3). This is the easiest measurement to make on seismic depth sections and has the advantage that the analytic model predicts that the angle is nearly constant with distance from the axis of diking. As described in the supplement, it depends on both w_0 and α . As long as we can estimate the thickness of the entire SDR package ($\sim w_0$) we can relate this angle to the effective elastic thickness of the lithosphere.

Before we relate seismic data on SDRs to model predictions we will consider how the approximations that go into the analytic model affect the parameters X_f , γ and ϕ . We will show that these parameters are useful for comparing the analytic model geometry to that predicted by less approximate numerical models. Using these three observables: X_f , γ and ϕ , we can reliably link SDRs geometries from MCS data to the plate strength that supports the SDRs in terms of effective elastic thickness T_e and lithospheric thickness H_L .

1.2.2 Numerical elastic thin plate model (NTP)

To get a closed-form description of the model geometry the analytic model treats the flexural response to magmatic loads as if lava flows cover the whole surface. However, lava should only fill in the region deeper than the top of the axial dike (Figure 2). To remove this inconsistency, we show the effects of more realistic lava loading on SDRs geometries while still using the thin plate flexure approximation. The finite difference method is used to solve for the vertical deflections due to the load of a half -dike added to the end of a thin elastic plate. The region adjacent to the axis that are deflected below their initial positions are then effectively filled with volcanic lava. The load of that infilling lava is then added to the plate and the resulting deflections computed. New lava is added to keep the volcanic surface at the initial surface level and the process is iterated until a steady-state is achieved. The accretion of additional dikes produces the same plate deflections and infill as the first dike and so the shape of model volcanic packages can be easily calculated (see supporting material for details (Turcotte & Schubert, 2002).

This numerical thin plate (NTP) model depends only on the flexure parameter α and the dike load that can be expressed as w_0 . The NTP model results in a much smaller off-axis bulge than for the analytic model with the same values of α and w_0 (Figure 3). This occurs because when the plate is flexed upward off-axis into the air, compensating mantle or lower crust resists being pulled up more than it would if the surface moved up into fluid with the density of lava. Compared to the analytic models with the same parameters, the NTP models predict that X_f is ~20% larger, γ is ~6% larger and ϕ is about the same.

1.2.3 Two Dimensional Numerical Models

The large magnitude curvature of SDRs implies that the elastic tensional stress near the surface can cause plastic yielding and the elastic thin plate approximation may be inaccurate. We simulate deformation of finite thickness lithosphere in response to magmatic loads using the numerical code FLAC (Fast Lagrangian Analysis of Continua)(*Cundall*, 1989; *Buck et al.*, 2005). This approach also allows us to consider the effects of elastic and non-elastic deformation including viscous flow and brittle-plastic deformation. FLAC is a two-dimensional explicit hybrid finite element-finite difference code that solves continuity, momentum balance and heat equations. This code has been used to model strain localization for faulting in both two- and three-dimensions with and without sedimentation (*Choi et al.*, 2013; *Tian & Choi*, 2017) and to track heat advection and diffusion (*Lavier and Buck*, 2002). In order to simulate and quantify lava infill, we modify the code to track surface deflections and add lava elements accordingly. Higher resolution tracers (described in the supplement) are deployed at the surface at set time intervals and move according to the velocity field. These tracers allow more precise quantification of the SDR geometry.

We only simulate the right half of a symmetric volcanic rift to save computation time. The bottom boundary is a Winkler foundation with the compensation pressure defined at the bottom of the rightmost column. Both the right and left boundaries are shear stress free. The horizontal velocity of the right boundary is set to be 1 cm/yr. The left boundary is treated in either of two ways that approximate a broken plate. For elastic plastic thick plate models, we set a lithostatic normal stress and new dike material is accreted during periodic remeshing. For elasto-visco-plastic models that account for variable viscosity, a column of low viscosity ‘dike elements’ is made to widen steadily while the horizontal boundary velocity is set to zero.

For the simpler cases we use either a single Elastic or Elastic-Plastic layer with density of upper crust of 2800 kg/m^3 supported by Winkler foundation of lower crust with density of 3000 kg/m^3 .

In the Elasto-Visco-Plastic cases, layers with both upper and lower crust are assumed to float on an underlying mantle layer. Brittle deformation is calculated with a Mohr-Coulomb failure criterion with a constant friction angle of 30° , and cohesion of 20 or 40 MPa. Ductile deformation follows Newtonian or non-Newtonian rheology with flow rules of dry quartz (Brace & Kohlstedt, 1980; Davis & Lavier, 2017) or dry plagioclase (Shelton & Tullis, 1981) for the crust and dry Olivine (Goetze & Poirier, 1978) for the mantle. Constant thermal structure models assume linearly increasing temperature with depth. We vary initial crustal thickness and bottom boundary temperature conditions for simulating different mechanical thickness and dike loads. The crustal thickness controls effects of dike loads while bottom temperature affects initial mechanical thickness and thus the plate strength.

For thermally evolving models, we include a mantle layer underlying the crust. Diking brings in heat by intruding 1300°C fluid dikes that has latent heat of solidification of 500 kJ/kg following Behn & Ito, (2008). Meanwhile, cooling due to hydrothermal circulation is approximated by enhancing the thermal conductivity via Nusselt number in regions shallower than 10 km and colder than 600°C . Nusselt number is assumed to increase linearly from 5 to 8 with plastic strain from 0 to 1.

1.2.3.1 Numerical Convergence of Elastic and Elastic Plastic thick plate cases

We first show how the 2D model results depend on grid size and number of numerical iterations. Due to the non-linearity of the problem and for the purpose of benchmarking, we only consider cases with a single large (i.e. 1 km wide) dike load (Figure S3a). The parameters used in the FLAC models are shown in Tables S1 and S2. The results obtained after sufficient numerical

iterations that the deflection changes are insignificant (Figure S3 b&c) show that elastic thick plate results are within 1% of the deflection of the numerical thin plate results. The slightly larger deflection for the thick plate cases are anticipated due to vertical compression (Comer, 1983). Results indicate (see figure S3d & S4d) that decreasing the grid size below 1 km makes a negligible difference even for our thinnest lithospheric thickness of ~6 km. For simplicity, we keep this 1 km grid size for all our models. When subjected to this narrow load the EP thick plate model behaves much like its elastic thick plate counterpart (figure S4) in terms of convergence but shows a relatively larger curvature due to plastic yielding (figure S4 b&c).

1.2.3.2 Elastic-Plastic (EP) thick plate with long-term plate extension

The analytic and numerical thin plate models assume invariable plate strength and lithospheric response with repeating magmatic loads. However, the system may have spatial and temporal changes in density structure, plate strength and magmatic loads. We here allow long-term plate motion away from the axis of dike accretion with plastic deformation and try to quantify these effects by considering the evolution of effective plate strength with geological time-averaged repeated small dike (i.e. Qin & Buck, 2008) and related volcanic loads.

In contrast to the previous benchmark, we treat constant dike widening at the rift axis and a constant horizontal velocity at the right boundary (Figure 4a). The low-density upper crust and volcanic infill dynamically changes. The plastic strain pattern (Figure 4b) follows the overall shape of the SDRs because new lava added to the surface with initially zero plastic strain deforms near the surface due to the plate bending and is advected with the plate. The major result of a range of model cases (Figure 5) is that the predicted flow geometry is similar to that of the analytic model, predicted by steady-state deflection. Measuring X_f , γ , described in section 2.1, allows us to estimate the effective plate elastic thickness T_e for the analytic model that best fits

the thick plate results. We vary the brittle layer thickness H_L and estimate the corresponding T_e (Figure 5b). Varying the layer cohesion from 20 to 40 MPa has little effect on the relation between H_L and T_e . The average effective elastic thickness from both X_f and γ varies with H_L according to the best linear fitting function $T_e = 0.49 H_L$ for models with cohesion of 20 MPa.

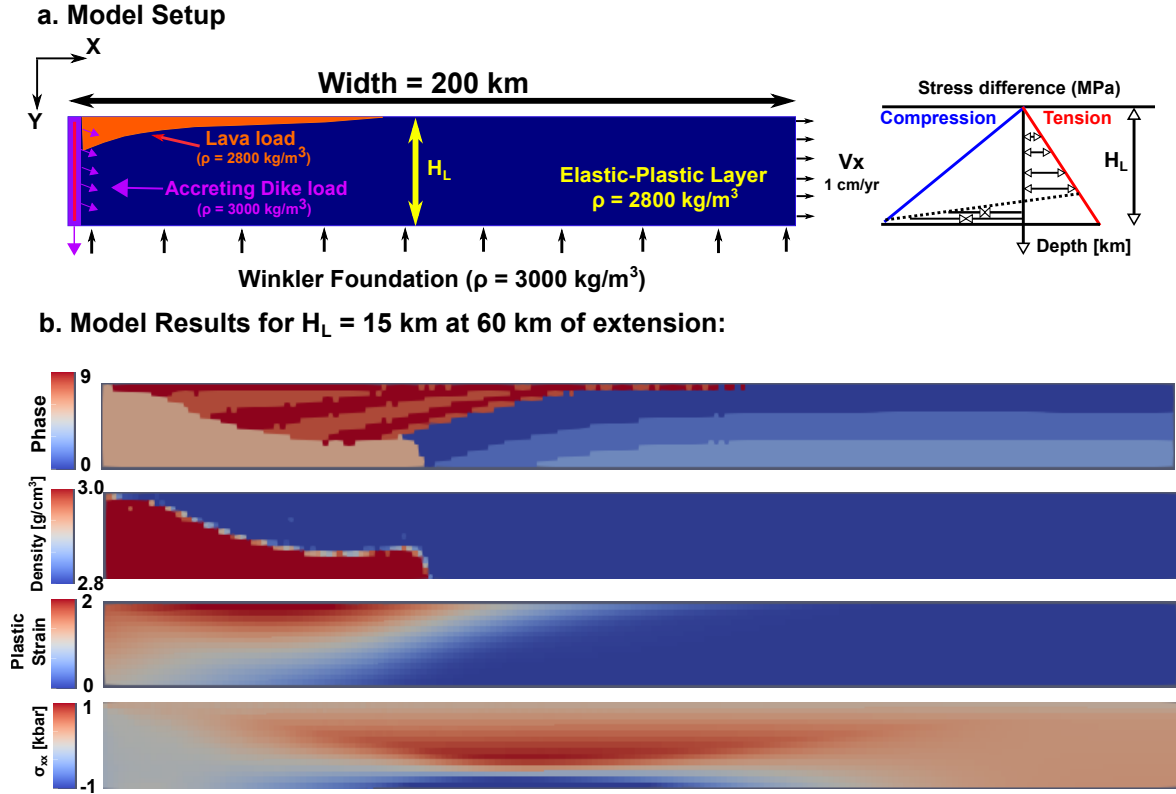
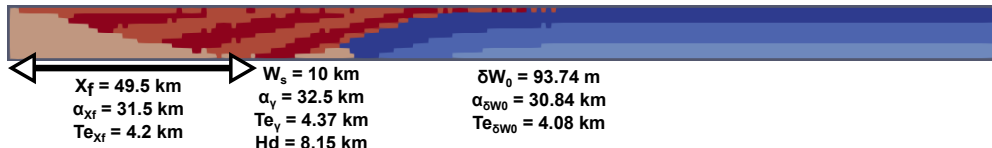


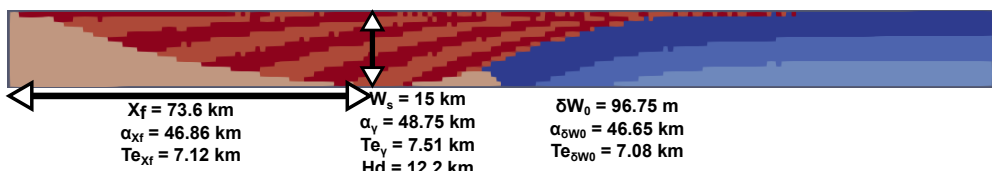
Figure 4. Model results for elasto-plastic thick plate with long-term extension. **a.** Model setup: model domain is H_L thick and 200 km wide. The elastic and plastic properties are defined in the text. **b.** SDRs geometries (phase numbers are for different model materials, 1~3 are for upper crust; 4 for lower crust; 5 for mantle; 6 and 7 for dikes; 8 and 9 are for lava flows), density, plastic strain and deviatoric horizontal stress at 60 km of extension.

a. EP thick Plate with different H_L

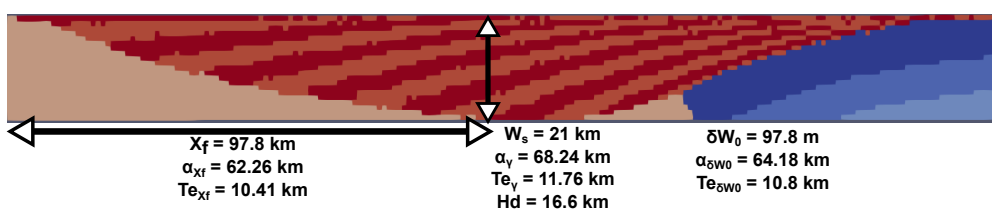
$H_L = 10 \text{ km at } 70 \text{ km of extension:}$



$H_L = 15 \text{ km at } 100 \text{ km of extension:}$



$H_L = 21 \text{ km at } 140 \text{ km of extension:}$



b. Model results for EP effective Te from X_f and γ

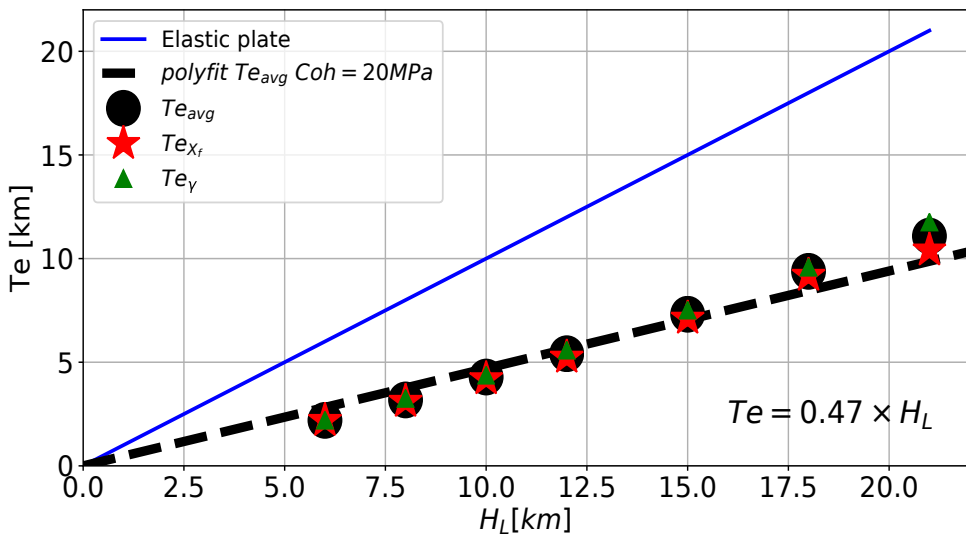


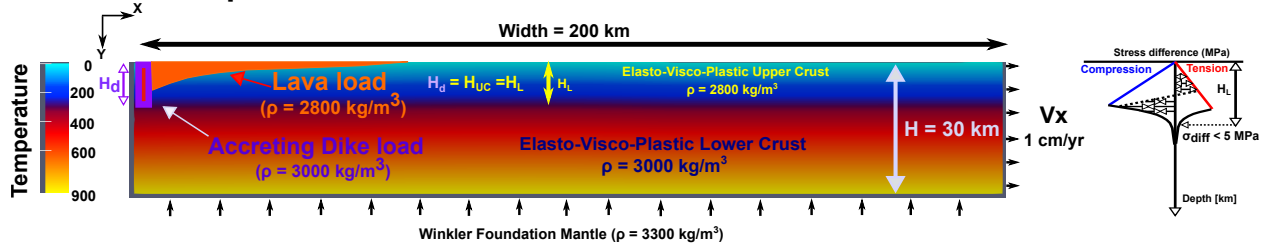
Figure 5. Model results for elasto-plastic (EP) thick plates with different layer thickness H_L .
a. Predicted geometries at model times when the volcanic infill reaches the bottom boundary. $\phi \approx 30^\circ$ b. Estimated effective elastic thickness Te for cases with different initial plate thicknesses H_L . The red stars are Te estimated from X_f measurements, the green triangles are from γ measurements from the models and the black dots are the average of the two estimations. The black dashed line is the best linear fit ($Te = 0.49H_L$ with $R^2 = 0.97$) to the average Te (black dots) that passes the origin.

1.2.3.3 Elasto-visco-plastic (EVP) thick plate with constant thermal structure

The EP thick plate models neglect the effects of viscous flow that could alter the plate bending behavior (e.g. Olive et al., 2016). In this section, we assume a laterally uniform thermal structure with strain rate independent Newtonian rheology to quantify the effects of visco-plastic deformation. The viscosity η ($Pa \cdot s$) is given by $\eta = \dot{\varepsilon}_n^{1-n} A^{-1/n} \cdot \exp(E/nRT) \cdot 10^6$ where $A = 500 (MPa^{-n} \cdot s^{-1})$, $E = 2 \times 10^5 (J/mol)$, $n = 1$ for Newtonian rheology, R is the universal gas constant of $8.31448 (J \cdot mol^{-1} K^{-1})$, T is the temperature in degree Celsius.

Compared to the previous single layer EP model, the EVP model with both upper and lower crust (Figure 6) allows us to treat a more realistic density structure where the lower density upper crust subsides into the higher density lower crust (Figure 6b). The lower density root exerting a local upward buoyancy force away from the axis, together with the downward loads from dikes near the axis, produces a bending moment that could further rotate the SDRs. The neutral plane where the stress difference due to bending is zero deepens significantly because of plasticity near the surface. The angle between the flows and the dike flow interface, ϕ , varies from 43° to 54° (Figure 7) are about 10° larger than the analytically predicted angle ϕ that ranges from 30° to 43° (Figure S2). The torque due to upper crustal root along with viscous relaxation might contribute to this extra SDR rotation.

a. Model Setup



b. Model Results for $H_L = 10 \text{ km}$ at 80 km of extension:

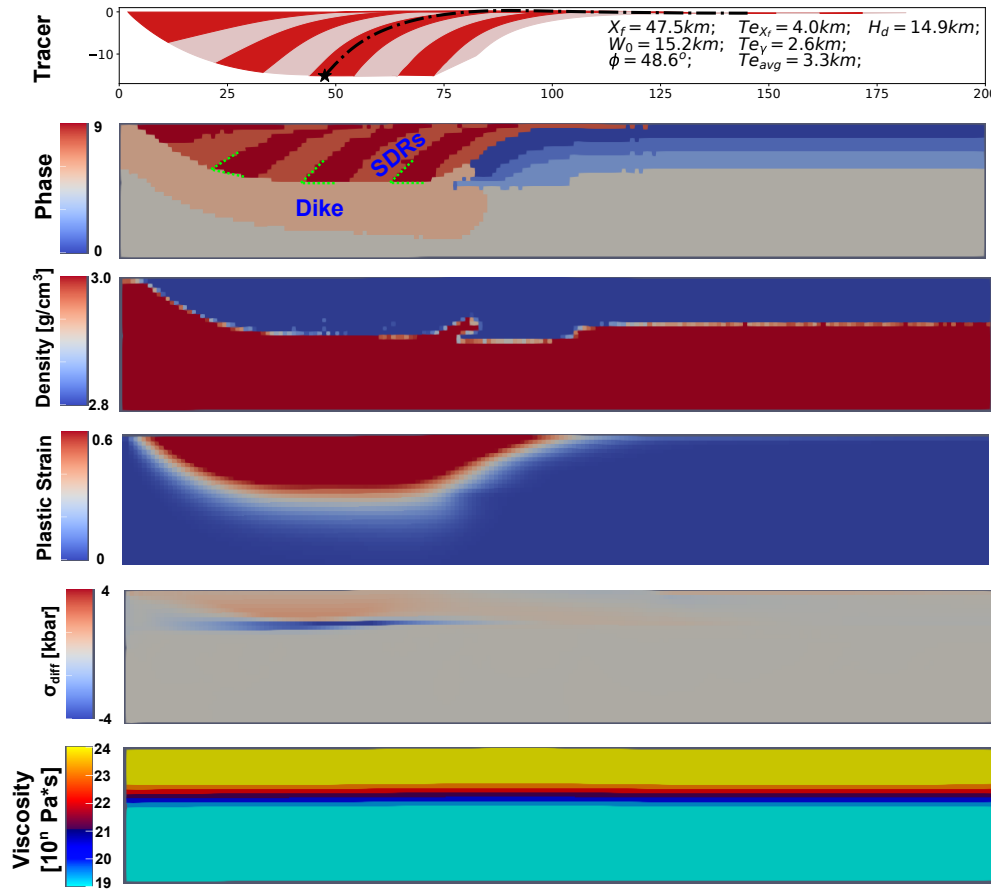
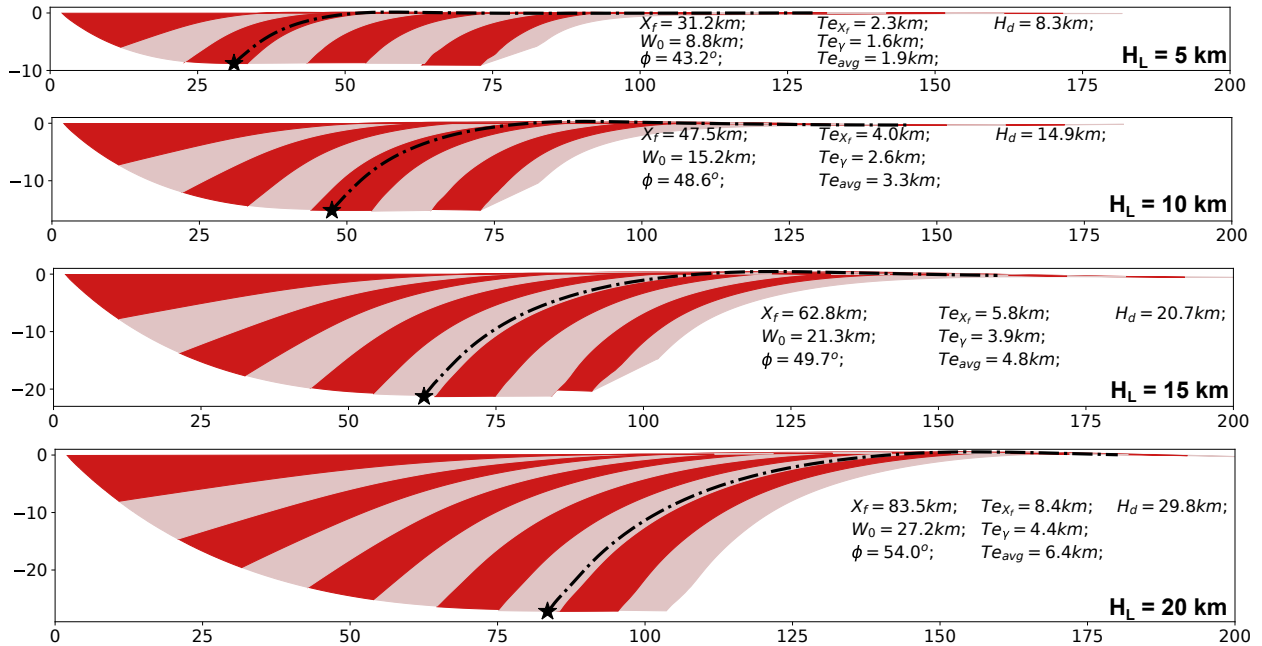


Figure 6. Model results for an Elasto-visco-plastic (EVP) thick plate case with constant thermal structure and Newtonian dry quartz rheology. a. Model setup: The viscosity structure is a function of temperature that linearly increases from surface to bottom and is laterally uniform. b. Model results for a case with a bottom boundary temperature of 900 °C that gives $H_L = 10 \text{ km}$. $\phi = 48.6^\circ$.

a. EVP Model tracer results with different H_L



b. Te from X_f and γ as a function of H_L

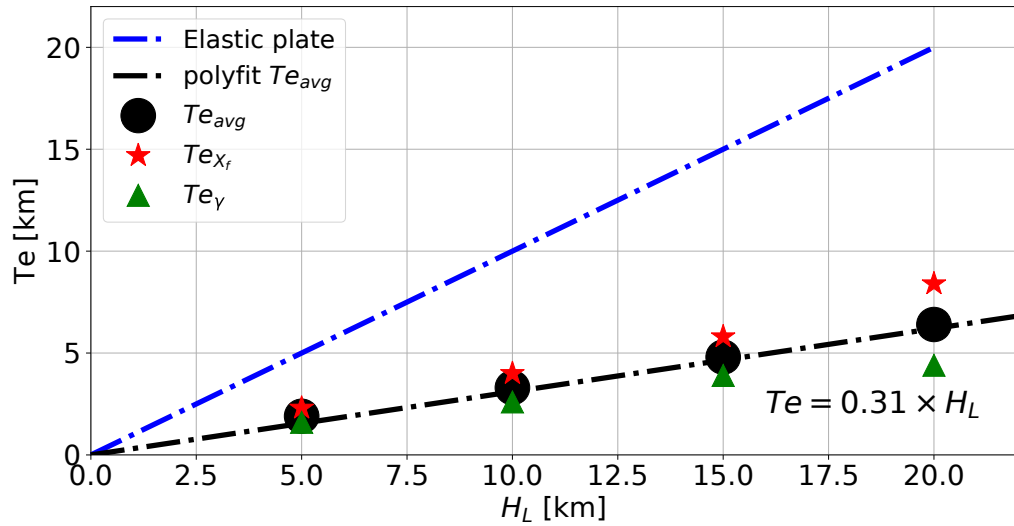


Figure 7. Model tracer results from Newtonian EVP cases. a. SDRs geometries with different values of H_L . b. Effective Te versus lithospheric thickness H_L . The red stars are Te estimated from X_f measurements, the green triangles are from γ measurements from the models and the black dots are the average of the two estimations. The blue dashed line is the best linear fit ($Te = 0.32H_L$ with $R^2 = 0.99$) to the average Te (black dots) that passes the origin.

When the model reaches steady state, in that the pattern of deflections per amount of dike opening becomes stable, we measure X_f and γ to estimate effective α and T_e . We found systematic larger T_e from X_f estimation. The lithospheric thickness is defined as the distance from the surface to the depth where compressional horizontal deviatoric stress decreases to 5 MPa, similar to the base of the “mechanical boundary layer” when deformation transitions from elastic-brittle to viscous domination (Artemieva, 2011). The average effective elastic thickness from both X_f and γ varies with H_L according to the best linear fitting function $T_e = 0.32 H_L$ (Figure 7b), which is much less than that of the EP thick plate results (Figure 5b). This results from the rheology difference between the two. For the EP case, the maximum compression appears at the bottom of the plate (Figure 4b) whereas for the EVP case, the maximum differential stress (effectively the brittle ductile transition) is within the modeled layer and its depth depends on the curvature of the bending plate (Figure 6a). The integrated bending moment for EVP model with same H_L is thus much less than its EP model counterpart. Note that in the cases illustrated here the lower crust flows to compensate the magmatic loads. The overall trend of larger T_{e_X} than T_{e_γ} might be due to the extra bending moment exerted from the lower density upper crustal root which gives a larger dip angle without changing other parameters.

1.2.3.4 Elasto-visco-plastic thick plate with thermal evolution

Thermal structure is taken as a control variable in previous models. However, magmatism brings heat to the rifting center, changing the thermal structure and plate strength. Here we show results of models that include heating due to dike intrusion of magma with an initial temperature of 1300°C and latent heat of solidification as well as cooling from parameterized hydrothermal circulation. We test two crustal rheologies (Figure 8): dry quartz (Brace & Kohlstedt, 1980) and dry plagioclase (Shelton & Tullis, 1981). We also study the effects of magma intrusion into the

lower crust that may approximate magmatic underplating. For these cases, a mantle layer is included. The lava is deposited with a surface temperature of 0°C because flows should cool within years.

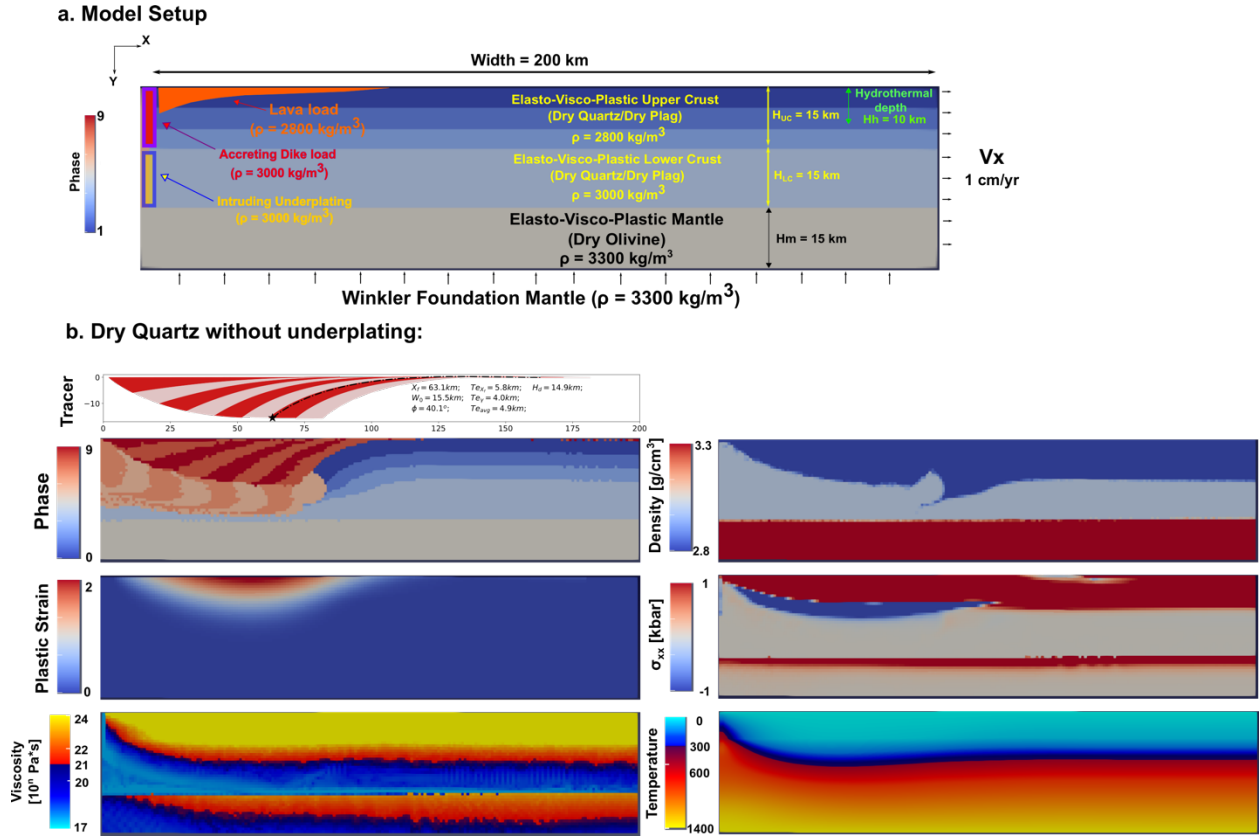


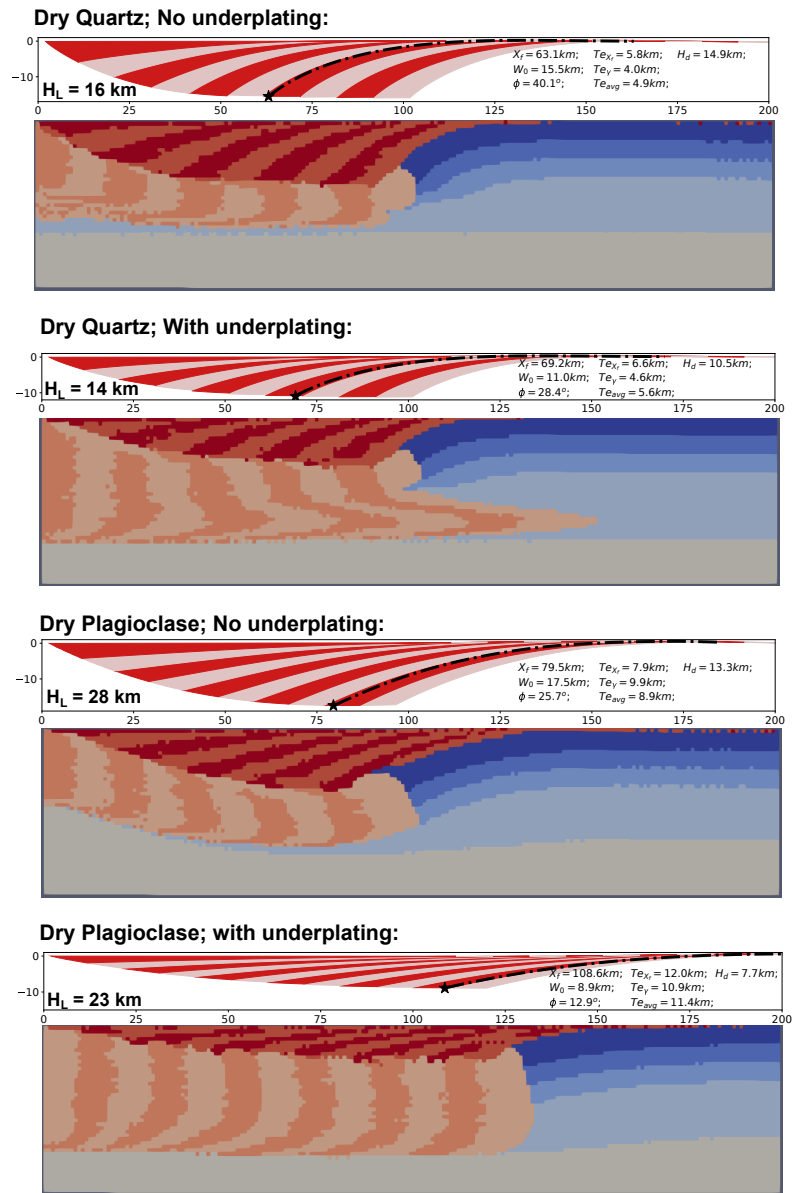
Figure 8. Elasto-visco-plastic (EVP) thick plate with thermal evolution and effects of underplating. a. Model setup: Upper crust 15 km thick with density of 2800 kg/m^3 underlying lower crust 15 km thick with a density of 3000 kg/m^3 and 15 km thick mantle of density 3300 kg/m^3 and rheology of dry olivine (Goetze & Poirier, 1978). Model domain is 45 km thick and 200 km wide. Bottom boundary is supported by Winkler foundation with mantle density of 3300 kg/m^3 . The left boundary is fixed with one column of widening dike with viscosity of $1 \times 10^{17} \text{ Pas}$ simulating a broken plate condition. The accreting solidified dike has a density of 3000 kg/m^3 and provides a downward load near the rift axis. The right boundary is stretched with half spreading rate of $V_x = 1 \text{ cm/yr}$. The hydrothermal circulation is approximated with enhanced conductivity via Nusselt number described in text. Lava is filled according to the surface deflections. b. Model results at 80 km of extension with dry quartz rheology and without underplating.

The overall behavior is qualitatively similar to the previous constant thermal structure EVP models but varies in detail (Figures 8&9). The biggest difference is that diking provides

heat that weakens the plate near the rifting center (figure 8b). This leads to a reduction in brittle thickness on axis and thus the effective dike load near the axis decreases. However, this does not generate a large difference in the total thickness of the SDR package because as dense solidified dikes move off axis, they accrete to the colder off-axis lithosphere providing a downward load. The downward advection of cold volcanic infill produces minor thickening of lithosphere within a flexural wavelength the axis (figure 8b).

Changing the rheology from dry quartz to dry plagioclase effectively increases the lithospheric thickness H_L (Figure 9) from 16 to 28 km (no underplating) and 14 to 23 km (with underplating). Because T_e and H_L again share linear relationship that T_e is about 37% of H_L , the change of rheology also increases T_e . Note that the linear relation between T_e and H_L for the EVP thermally evolving model lies in between EP and EVP models with constant thermal structure (Figure 10). We use this relation for the mapping between T_e and H_L in data as described below.

a. Model results with thermal evolution



b. T_e from X_f and γ as a function of H_L

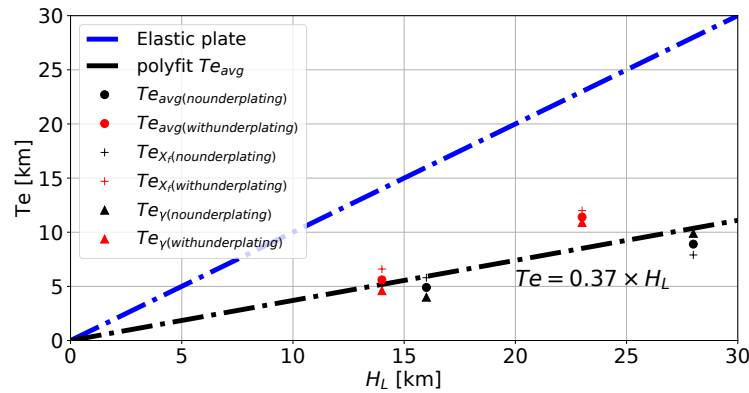


Figure 9. Thermally evolving model results summary. a. SDRs geometries and phase distribution with the indicated lower crustal rheology both with and without intrusion into the lower crust (underplating). b. Effective Te versus lithospheric thickness H_L . The red color symbols are for models with underplating and the black color symbols are for models without underplating. The red dashed line is the best linear fit ($Te = 0.38H_L$ with $R^2 = 0.84$) to the average Te (circles and squares) that passes the origin.

We also study the effects of underplating. With the same model setup except for whether there is lower crustal intrusion or not, the models show different SDRs shapes. The models with underplating (Figure 9) have thinner SDRs and relatively higher Te compared to that of the models without underplating. The models with underplating also have lower H_L than models without underplating. The extra intrusion from underplating brings in more heat and leads to a slightly weaker lithosphere (lower H_L). On the other hand, when there is no underplating, SDRs subside faster and the increased rate of downward advection of cool material results in higher H_L . Without underplating, the model resembles the EVP constant thermal structure models (Figures 6&7) and the magmatic loads are compensated in the lower crust. With underplating, the lower crustal intrusion takes up the space for SDRs to subside and mantle partially becomes the compensating layer depending on how strong the crust and mantle are coupled. For strong crust-mantle coupling (as they are here for dry plagioclase), the lower crustal intrusion acts as a bridge for mantle to fully compensate the magmatic loads and this leads to a 49% reduction in SDRs thickness and 22% increase in Te than that for models with compensation in the lower crust. For our results where crust and mantle are partially coupled, the lower crustal intrusion is “squeezed” out by the subsiding magmatic loading (dry quartz). This “squeezing” behavior induces resistance to the SDRs subsidence and causes 29% reduction in SDRs thickness and 12% increase in Te. Despite the complexity induced by underplating, namely, decreasing H_L and increasing Te, the Te estimations derived from the two observables (X_f and γ) are still consistent with each other and the results fall within the narrow range of EP thick plate and EVP thick plate

cases (Figure 10). This means that the effects of underplating to X_f and γ are not weighted significantly differently. Thus, even with underplating, it is still valid to use the average T_e derived from X_f and γ to estimate H_L from T_e . When information about underplating and the degree of crust-mantle coupling is available, slight adjustments would yield more accurate estimations: decrease H_L by 12% for partial crust-mantle coupling to 18% for fully coupled crust and mantle.

We summarize all the model results in Figure 10 (Model parameters are summarized in Table S3; Model videos are uploaded on <https://doi.org/10.6084/m9.figshare.4573510.v1>). EP thick plate models with long-term extension show a linear relationship of $T_e = 0.49H_L$. Increasing cohesion from 20 MPa to 40 MPa induces little increase in plate strength. EVP thick plate models with Newtonian rheology and constant thermal structure realistically simulate the density structure evolution by allowing low density roots in the denser lower crust. Concerning effective plate strength, EVP constant thermal models predict $T_e = 0.32H_L$. The EVP thermally evolving models fall in between with $T_e = 0.38H_L$.

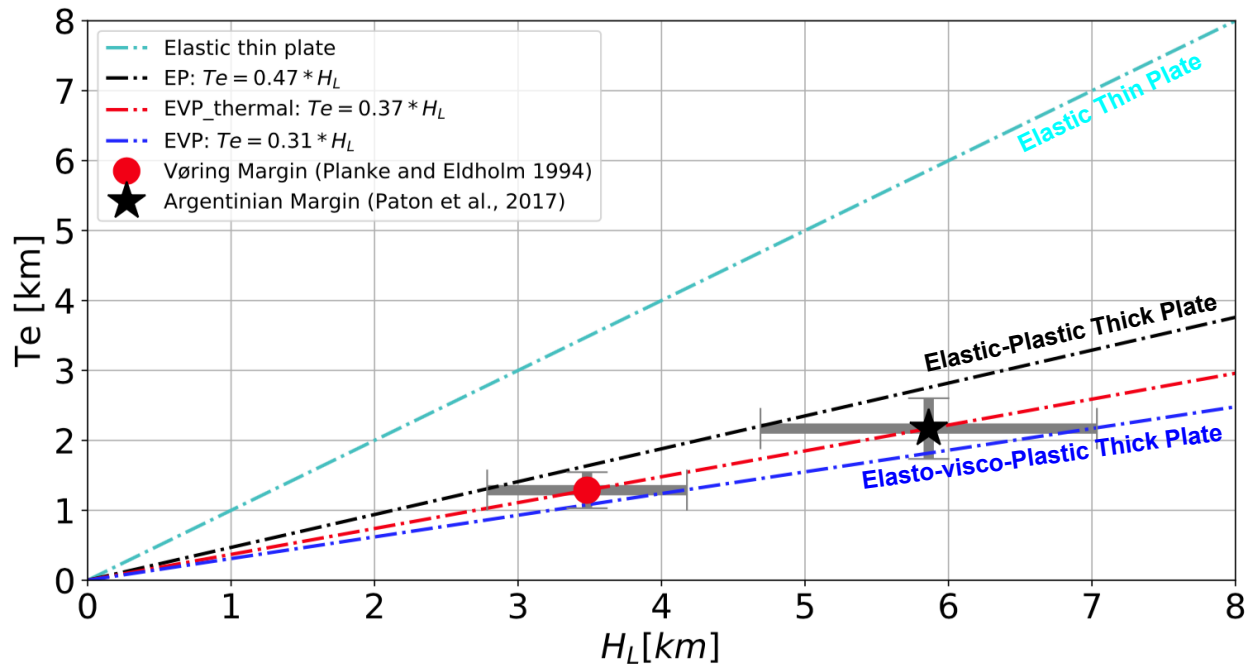


Figure 10. Final model results compilation: Mapping effective Te to lithospheric thickness H_L . Two depth converted images from the Vøring Margin (Planke & Eldholm, 1994) and the Argentinian Margin (Paton et al., 2017) are shown with error estimation as described in the text and illustrated in Figure 3.

1.3 Analysis of data

The major goal of this study is to link the seismically observed SDR geometries to lithospheric thickness H_L . Previous sections build a framework for achieving this goal. Essentially, the analytic model (ATP) indicates X_f and γ are two useful and observable parameters that can be related to the effective elastic thickness Te in both models and data. Numerical models build a quantitative relationship between Te and H_L . Using this relationship and measuring X_f and γ for real SDRs, we can quantify the lithospheric thickness for volcanic rifted margins. When considering the three-dimensional nature of rifting, the dip angle of SDR for calculating γ is assumed to be the true dip in our 2D cross-sectional models. However, if the strike of the data profile is not parallel to the spreading direction, the apparent dip measured is smaller than the true dip. But the effect is small for profiles away from fracture zones according to McDermott et al., (2018).

For the numerical model results, in order to estimate Te and H_L with minimum subjective bias, we automate the data processing for retrieving the values of X_f and γ . We first estimate X_f by finding the distance from the seaward end of the SDRs to where there is a transition from negative to positive slope of the dike-lava interface. Then we find the reflecting layer intersecting the dike-lava interface at X_f , from which we calculate the dip angle ϕ at the tip of the SDR. The thickness of the SDR package at $x = X_f$ is W_0 and γ is the ratio of W_0 and $\tan(\phi)$. Using X_f and γ , we calculate two values of Te and average those estimates.

Because the EVP thermally evolving models have the least assumptions, we use its derived Te-H_L relationship for mapping Te to H_L in data. The approach is justified because the geometry of the numerical model SDRs is very similar to that predicted by the analytic model. Thus, we use the parameters X_f and γ to estimate the value of Te that describes the numerical model geometry. The lithospheric layer thickness H_L is taken to be the depth below the surface where the horizontal deviatoric stress decreases to 5 MPa. We then use this Te to H_L mapping, to relate the Te values estimated from the seismic sections with SDRs to the lithospheric thickness of plate margins at the time of rifting. From the analytic thin plate models, we analyze two depth-converted SDR profiles to yield effective elastic thickness Te of 1.3 km and 2.2 km for Vøring Margin (Figure S5) and Argentinian Margin (Figure S6), which are then mapped to lithospheric thickness during rifting of 3.4 km and 5.7 km (Figure 10).

1.4 Discussion and Conclusions

In this paper we considered how fairly simple magmatic processes might produce the observed geometry of volcanic rifted margins and then showed how such geometries depend on lithospheric thickness. The basic assumption is that the ‘space’ or depression that is filled by lava is generated by the load of solidifying magmatic intrusions and extrusives. A recently published treatment of such magmatic origin gives a simple analytic description of SDR geometry as a function of only two parameters, one of which is the effective elastic thickness Te of the lithosphere. We showed that these parameters, relating to the thickness and dip of analytic model SDRs, can easily be related to the model Te. The same parameters can be measured using seismic images of real SDRs. We went on to show how these geometric parameters could be used to constrain lithospheric thickness at the time of volcanic rifting.

We quantify the effects of simplifying approximations used in the analytic model on the model geometry. We first described a numerical thin-elastic plate model with more realistic spatial distribution of lava flows compared to the analytic model. For the same value of T_e more reasonable lava distribution produced a $\sim 20\%$ larger X_f , a $\sim 5\%$ larger γ and negligible change in ϕ .

We went on to develop the first two-dimensional thermal-mechanical models that simulate the geometry of SDRs formed by magmatic loads. The model allowed us to show that the thin elastic plate assumption had a modest effect on the model geometry. But, before we could do that a thorough study of the effect of numerical grid size and time steps had to be undertaken. We also showed that the use of tracers of volcanic layers greatly increased the reliability of model predicted structures. A test of a purely elastic layer against the numerical thin plate model counterpart shows that resulting geometric differences were negligible.

Following the benchmark, we develop the 2D models with realistic rheology and we summarize the model results in Figure 10. EP thick plate models with long term extension show close to linear trend of $T_e = 0.49H_L$. Increasing cohesion from 20 MPa to 40 MPa induces little increase in plate strength. EVP thick plate models with Newtonian rheology and constant thermal structure realistically calculate density structure evolution and predict a mapping of $T_e = 0.32H_L$. Effective plate strengths of the thermal evolving models fall between the narrow range of EP and EVP constant thermal model and predicts that the effective elastic thickness of the lithosphere is 37% of the actual thickness. Changing crustal material from dry quartz to dry plagioclase increases H_L and T_e by $\sim 60\%$. Underplating reduces SDRs thickness by $\sim 25\%$ (dry quartz without crust mantle coupling) and $\sim 50\%$ (dry plagioclase with crust mantle coupling). Using the

two observable parameters X_f and γ is still viable even for highly non-linear thermally evolving models and show consistent results.

From an analytic elastic thin plate model formulation, we derive Te-dependent observables X_f and γ that can be directly measured in MCS data. For SDRs that have not reached steady-state deflection, we consider another observable ϕ that represents the relationship between plate strength and dike loads. ϕ is useful because it is almost extension-independent; namely, ϕ remains nearly constant during SDRs evolution as long as plate strength remains the same. Measuring thickness between the bottom of SDRs package and the Moho depth gives an approximation of dike height h_d . Using ϕ and h_d together we can estimate Te. When all three observables are all available for the data, calculating Te separately from each observable gives confidence in the results. For example, from a depth converted SDRs profile offshore Argentina at 35° South (Figure 1), X_f measurement gives Te = 2.2 km, γ results in a Te of 2.1 km. Given the uncertainties in the MCS data, these results are highly consistent with each other.

The results indicate that the thickness of rifting lithosphere inversely correlates with estimated mantle potential temperature (Tp) of corresponding large igneous province (LIP). Based on petrological analysis (Herzberg & Gazel, 2009) estimate that for North Atlantic Igneous Province the values of Tp is ~1650 °C. Our estimate of the lithospheric thickness at the time of rifting was 3.4 km. For the Paraná-Etendeka large igneous province Hawkesworth et al. (2000) estimate that Tp is ~1450 °C. In the nearby Argentinian basin we find that the lithospheric thickness at the time of rifting was 5.7 km. This suggests that the hotter the mantle under an LIP the thinner the adjacent lithosphere.

Many questions about the formation of volcanic rifted margins remain. These include whether the formation of some SDRs is affected by large-offset normal faulting; what inner and

outer SDRs imply about temporal and spatial variations in magmatism and crustal structures (Franke et al., 2010; McDermott et al., 2018); and how subaerially formed SDRs subside significantly below current sea level. We hope the methods developed here and the results of our analysis of lithospheric strength during rifting will aid in future efforts to resolve some of these questions.

Acknowledgments

Authors would like to thank constructive reviews from Jenny Collier and Douglas Paton as well as discussion with Tony Watts, Rebecca Morgan, Joshua Davis, Jean Arthur Olive, Bar Oryan, Suzanne Carbotte, Marc Spiegelman and William Ryan; XT is grateful for discussion and code sharing from Eunseo Choi and would like to thank Dr. Liu Jie and Dr. Zhang Ke for granting access to the Tianhe 2 super-computer. Please find all model videos from <https://doi.org/10.6084/m9.figshare.4573510.v1>. Codes can be found from https://github.com/kelchuan/Tian_Buck_2019_JGR_SDR.git. The MCS data analysis are described in the supporting information file. This study is supported by the National Science Foundation [Awards OCE-1654745 and EAR-1650166].

References:

- Abdelmalak, M. M., Meyer, R., Planke, S., Faleide, J. I., Gernigon, L., Frieling, J., et al. (2016). Pre-breakup magmatism on the Vøring Margin: Insight from new sub-basalt imaging and results from Ocean Drilling Program Hole 642E. *Tectonophysics*, 675, 258–274. <https://doi.org/10.1016/j.tecto.2016.02.037>
- Artemieva, I. (2011). The lithosphere: An interdisciplinary approach. Cambridge University Press.
- Barberi, F., & Varet, J. (1970). The Erta Ale volcanic range (Danakil depression, northern afar, ethiopia). *Bulletin Volcanologique*, 34(4), 848–917. <https://doi.org/10.1007/BF02596805>

- Becker, K., Tanner, D. C., Franke, D., & Krawczyk, C. M. (2016). Fault-controlled lithospheric detachment of the volcanic southern South Atlantic rift. *Geochemistry, Geophysics, Geosystems*, 17(3), 887–894. <https://doi.org/10.1002/2015GC006081>
- Behn, M. D., & Ito, G. (2008). Magmatic and tectonic extension at mid-ocean ridges: 1. Controls on fault characteristics. *Geochemistry, Geophysics, Geosystems*, 9(8), <https://doi.org/10.1029/2008GC001965>
- Bialas, R. W., Buck, W. R., & Qin, R. (2010). How much magma is required to rift a continent? *Earth and Planetary Science Letters*, 292(1–2), 68–78. <https://doi.org/10.1016/j.epsl.2010.01.021>
- Bodvarsson, G., & Walker, G. P. L. (1964). Crustal Drift in Iceland. *Geophysical Journal of the Royal Astronomical Society*, 8(3), 285–300. <https://doi.org/10.1111/j.1365-246X.1964.tb06295.x>
- Brace, W. F., & Kohlstedt, D. L. (1980). Limits on lithospheric stress imposed by laboratory experiments. *Journal of Geophysical Research: Solid Earth*, 85(B11), 6248–6252. <https://doi.org/10.1029/JB085iB11p06248>
- Buck, W. R. (2006). The role of magma in the development of the Afro-Arabian Rift System. *Geological Society, London, Special Publications*, 259(1), 43–54. <https://doi.org/10.1144/GSL.SP.2006.259.01.05>
- Buck, W. R. (2017). The role of magmatic loads and rift jumps in generating seaward dipping reflectors on volcanic rifted margins. *Earth and Planetary Science Letters*, 466, 62–69. <https://doi.org/10.1016/j.epsl.2017.02.041>
- Buck, W. R., Lavier, L. L., & Poliakov, A. N. B. (2005). Modes of faulting at mid-ocean ridges. *Nature*, 434(7034), 719–723. <https://doi.org/10.1038/nature03358>
- Buiter, S. J. H., & Torsvik, T. H. (2014). A review of Wilson Cycle plate margins: A role for mantle plumes in continental break-up along sutures? *Gondwana Research*, 26(2), 627–653. <https://doi.org/10.1016/j.gr.2014.02.007>
- Calvès, G., Schwab, A. M., Huuse, M., Clift, P. D., Gaina, C., Jolley, D., et al. (2011). Seismic volcanostratigraphy of the western Indian rifted margin: The pre-Deccan igneous province. *Journal of Geophysical Research*, 116(B1), B01101. <https://doi.org/10.1029/2010JB000862>
- Choi, E., Buck, W. R., Lavier, L. L., & Petersen, K. D. (2013). Using core complex geometry to constrain fault strength. *Geophysical Research Letters*, 40(15), 3863–3867. <https://doi.org/10.1002/grl.50732>

- Clerc, C., Ringenbach, J.-C., Jolivet, L., & Ballard, J.-F. (2017). Rifted margins: Ductile deformation, boudinage, continentward-dipping normal faults and the role of the weak lower crust. *Gondwana Research*, (2016). <https://doi.org/10.1016/j.gr.2017.04.030>
- Comer, R. P. (1983). Thick plate flexure. *Geophysical Journal International*, 72(1), 101–113. <https://doi.org/10.1111/j.1365-246X.1983.tb02807.x>
- Courtillot, V., Jaupart, C., Manighetti, I., Tappognier, P., & Besse, J. (1999). On causal links between flood basalts and continental breakup. *Earth and Planetary Science Letters*, 166(3–4), 177–195. [https://doi.org/10.1016/S0012-821X\(98\)00282-9](https://doi.org/10.1016/S0012-821X(98)00282-9)
- Cundall, P. A. (1989). Numerical experiments on localization in frictional materials. *Ingenieur-Archiv*, 59(2), 148–159. <https://doi.org/10.1007/BF00538368>
- Davis, J. K., & Lavier, L. L. (2017). Influences on the development of volcanic and magma-poor morphologies during passive continental rifting. *Geosphere*, 13(5), 1524–1540. <https://doi.org/10.1130/GES01538.1>
- Direen, N. G., & Crawford, A. J. (2003). Fossil seaward-dipping reflector sequences preserved in southeastern Australia: a 600 Ma volcanic passive margin in eastern Gondwanaland. *Journal of the Geological Society*, 160(6), 985–990. <https://doi.org/10.1144/0016-764903-010>
- Ebinger, C. J., & Hayward, N. J. (1996). Soft plates and hot spots: Views from Afar. *Journal of Geophysical Research: Solid Earth*, 101(B10), 21859–21876. <https://doi.org/10.1029/96JB02118>
- Eldholm, O., Skogseid, J., Planke, S., & Gladczenko, T. P. (1995). Volcanic Margin Concepts. In *Rifted Ocean-Continent Boundaries* (pp. 1–16). Dordrecht: Springer Netherlands. https://doi.org/10.1007/978-94-011-0043-4_1
- Elliott, G. M., Berndt, C., & Parson, L. M. (2009). The SW African volcanic rifted margin and the initiation of the Walvis Ridge, South Atlantic. *Marine Geophysical Researches*, 30(3), 207–214. <https://doi.org/10.1007/s11001-009-9077-x>
- Franke, D., Ladage, S., Schnabel, M., Schreckenberger, B., Reichert, C., Hinz, K., et al. (2010). Birth of a volcanic margin off Argentina, South Atlantic. *Geochemistry, Geophysics, Geosystems*, 11(2). <https://doi.org/10.1029/2009GC002715>
- Geoffroy, L. (2005). Volcanic passive margins. *Comptes Rendus - Geoscience*, 337(16), 1395–1408. <https://doi.org/10.1016/j.crte.2005.10.006>
- Geoffroy, L., Burov, E. B., & Werner, P. (2015). Volcanic passive margins: another way to break up continents. *Scientific Reports*, 5(14828), 14828. <https://doi.org/10.1038/srep14828>

- Gibson, I. L., & Love, D. (1989). A Listric Fault Model for the Formation of the Dipping Reflectors Penetrated during the Drilling of Hole 642E, ODP Leg 104. In Proceedings of the Ocean Drilling Program, 104 Scientific Results. Ocean Drilling Program. <https://doi.org/10.2973/odp.proc.sr.104.195.1989>
- Gladczenko, T. P., Skogseid, J., & Eldhom, O. (1998). Namibia volcanic margin. *Marine Geophysical Researches*, 20(4), 313–341. <https://doi.org/10.1023/A:1004746101320>
- Goetze, C., & Poirier, J. P. (1978). The Mechanisms of Creep in Olivine [and Discussion]. *Philosophical Transactions of the Royal Society A: Mathematical, Physical and Engineering Sciences*, 288(1350), 99–119. <https://doi.org/10.1098/rsta.1978.0008>
- Hawkesworth, C. J., Gallagher, K., Kirstein, L., Mantovani, M. S. M., Peate, D. W., & Turner, S. P. (2000). Tectonic controls on magmatism associated with continental break-up: an example from the Paraná–Etendeka Province. *Earth and Planetary Science Letters*, 179(2), 335–349. [https://doi.org/10.1016/S0012-821X\(00\)00114-X](https://doi.org/10.1016/S0012-821X(00)00114-X)
- Herzberg, C., & Gazel, E. (2009). Petrological evidence for secular cooling in mantle plumes. *Nature*, 458(7238), 619–622. <https://doi.org/10.1038/nature07857>
- Hinz. (1981). A hypothesis on terrestrial catastrophes. Retrieved from <http://www.schweizerbart.de/publications/detail/artno/186082200/A-Hypothesis-on-Terrestrial-Catastrophes>
- Jackson, M. P. , Cramez, C., & Fonck, J.-M. (2000). Role of subaerial volcanic rocks and mantle plumes in creation of South Atlantic margins: implications for salt tectonics and source rocks. *Marine and Petroleum Geology*, 17(4), 477–498. [https://doi.org/10.1016/S0264-8172\(00\)00006-4](https://doi.org/10.1016/S0264-8172(00)00006-4)
- Kalberg, T., & Gohl, K. (2014). The crustal structure and tectonic development of the continental margin of the Amundsen sea embayment, West Antarctica: Implications from geophysical data. *Geophysical Journal International*, 198(1), 327–341. <https://doi.org/10.1093/gji/ggu118>
- Kendall, J.-M., Stuart, G. W., Ebinger, C. J., Bastow, I. D., & Keir, D. (2005). Magma-assisted rifting in Ethiopia. *Nature*, 433(7022), 146–148. <https://doi.org/10.1038/nature03161>
- Kristoffersen, Y., Hofstede, C., Diez, A., Blenkner, R., Lambrecht, A., Mayer, C., & Eisen, O. (2014). Reassembling Gondwana: A new high quality constraint from vibroseis exploration of the sub-ice shelf geology of the East Antarctic continental margin. *Journal of Geophysical Research: Solid Earth*, 119(12), 9171–9182. <https://doi.org/10.1002/2014JB011479>
- Lavier, L. L., & Buck, W. R. (2002). Half graben versus large-offset low-angle normal fault: Importance of keeping cool during normal faulting, 107, 1–16.

- Lavier, L. L., Buck, W. R., & Poliakov, A. N. B. (2000). Factors controlling normal fault offset in an ideal brittle layer. *Journal of Geophysical Research: Solid Earth*, 105(B10), 23431–23442. <https://doi.org/10.1029/2000JB900108>
- McDermott, C., Lonergan, L., Collier, J. S., McDermott, K. G., & Bellingham, P. (2018). Characterization of seaward-dipping reflectors along the S. American Atlantic margin and implications for continental breakup. *Tectonics*. <https://doi.org/10.1029/2017TC004923>
- Morgan, R., & Watts, A. (2018). Seismic and gravity constraints on flexural models for the origin of seaward dipping reflectors. *Geophysical Journal International*, 214(3), 2073–2083. <https://doi.org/10.1093/gji/ggy243>
- Morgan, R., & Watts, A. B. (2017). Isostatic Gravity Anomalies, Flexure and the Origin of Seaward Dipping Reflectors at Volcanic Rifted Margins. 2016 Fall AGU Meeting.
- Mutter, J. C., Talwani, M., & Stoffa, P. L. (1982). Origin of seaward-dipping reflectors in oceanic crust off the Norwegian margin by “subaerial sea-floor spreading.” *Geology*, 10(7), 353. [https://doi.org/10.1130/0091-7613\(1982\)10<353:OOSRIO>2.0.CO;2](https://doi.org/10.1130/0091-7613(1982)10<353:OOSRIO>2.0.CO;2)
- Olive, J.-A., Behn, M. D., Mittelstaedt, E., Ito, G., & Klein, B. Z. (2016). The role of elasticity in simulating long-term tectonic extension. *Geophysical Journal International*, 205(2), 728–743. <https://doi.org/10.1093/gji/ggw044>
- Palmason, G. (1973). Kinematics and Heat Flow in a Volcanic Rift Zone, with Application to Iceland. *Geophysical Journal International*, 33(4), 451–481. <https://doi.org/10.1111/j.1365-246X.1973.tb02379.x>
- Paton, D. A., Pindell, J., McDermott, K., Bellingham, P., & Horn, B. (2017). Evolution of seaward-dipping reflectors at the onset of oceanic crust formation at volcanic passive margins: Insights from the South Atlantic. *Geology*, G38706.1. <https://doi.org/10.1130/G38706.1>
- Pérez-Gussinyé, M., Lowry, A. R., & Watts, A. B. (2007). Effective elastic thickness of South America and its implications for intracontinental deformation. *Geochemistry, Geophysics, Geosystems*, 8(5). <https://doi.org/10.1029/2006GC001511>
- Pindell, J., Graham, R., & Horn, B. (2014). Rapid outer marginal collapse at the rift to drift transition of passive margin evolution, with a Gulf of Mexico case study. *Basin Research*, 26(6), 701–725. <https://doi.org/10.1111/bre.12059>
- Planke, S., & Eldholm, O. (1994). Seismic response and construction of seaward dipping wedges of flood basalts: Vøring volcanic margin. *Journal of Geophysical Research: Solid Earth*, 99(B5), 9263–9278. <https://doi.org/10.1029/94JB00468>

- Planke, S., Symonds, P. A., Alvestad, E., & Skogseid, J. (2000). Seismic volcanostratigraphy of large-volume basaltic extrusive complexes on rifted margins. *Journal of Geophysical Research*, 105(B8), 19335–19351. <https://doi.org/10.1029/1999JB900005>
- Poliakov, A. N. B., & Roger Buck, W. (1998). Mechanics of stretching elastic-plastic-viscous layers: Applications to slow-spreading mid-ocean ridges. In *Geophysical Monograph Series* (Vol. 106, pp. 305–323). <https://doi.org/10.1029/GM106p0305>
- Quirk, D. G., Shakerley, A., & Howe, M. J. (2014). A mechanism for construction of volcanic rifted margins during continental breakup. *Geology*, 42(12), 1079–1082. <https://doi.org/10.1130/G35974.1>
- Saikia, U., Das, R., & Rai, S. S. (2017). Possible magmatic underplating beneath the west coast of India and adjoining Dharwar craton: Imprint from Archean crustal evolution to breakup of India and Madagascar. *Earth and Planetary Science Letters*, 462, 1–14. <https://doi.org/10.1016/j.epsl.2017.01.004>
- Schnabel, M., Franke, D., Engels, M., Hinz, K., Neben, S., Damm, V., et al. (2008). The structure of the lower crust at the Argentine continental margin, South Atlantic at 44°S. *Tectonophysics*, 454(1–4), 14–22. <https://doi.org/10.1016/j.tecto.2008.01.019>
- Shelton, G. L., & Tullis, J. (1981). Experimental flow laws for crustal rocks. In *EOS Trans. Am. Geophys. Union* (Vol. 62, p. 396). Retrieved from <http://ci.nii.ac.jp/naid/10010125720/en/>
- Skogseid, J. (1994). Dimensions of the Late Cretaceous-Paleocene Northeast Atlantic rift derived from Cenozoic subsidence. *Tectonophysics*, 240(1–4), 225–247. [https://doi.org/10.1016/0040-1951\(94\)90274-7](https://doi.org/10.1016/0040-1951(94)90274-7)
- Tian, X., & Choi, E. (2017). Effects of axially variable diking rates on faulting at slow spreading mid-ocean ridges. *Earth and Planetary Science Letters*, 458, 14–21. <https://doi.org/10.1016/j.epsl.2016.10.033>
- Turcotte, D. L., & Schubert, G. (2002). *Geodynamics*. Cambridge: Cambridge University Press. <https://doi.org/10.1017/CBO9780511807442>
- Watts, A. B., & Cox, K. G. (1989). The Deccan Traps: an interpretation in terms of progressive lithospheric flexure in response to a migrating load. *Earth and Planetary Science Letters*, 93(1), 85–97. [https://doi.org/10.1016/0012-821X\(89\)90186-6](https://doi.org/10.1016/0012-821X(89)90186-6)
- White, R. S., Smith, L. K., Roberts, a W., Christie, P. a F., Kusznir, N. J., Roberts, a M., et al. (2008). Lower-crustal intrusion on the North Atlantic continental margin. *Nature*, 452(7186), 460–464. <https://doi.org/10.1038/nature06687>

Appendix 1:

A1-1 Review of Analytic elastic thin plate model and its linkage to SDRs observations

According to a number of workers (e.g. Bodvarsson & Walker, 1964; Morgan & Watts, 2018; Watts & Cox, 1989) SDRs geometries are an expression of the flexural response of lithosphere to magmatic loads. An analytic description of the magma loading model was derived by Buck, (2017), who considers a series of dike and lava loads. For one dike load, the surface of the plate deflects as (see Figure A1-1):

$$\delta w(x) = \delta w_0 \exp\left(-\frac{x}{\alpha}\right) \cos\left(\frac{x}{\alpha}\right) \quad (1)$$

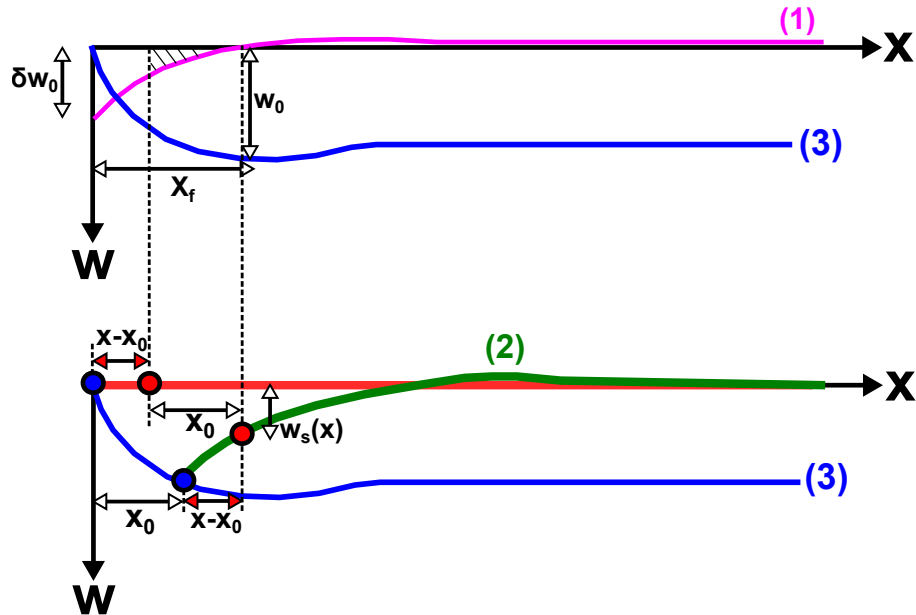


Figure S1. Cartoon illustration of the analytical equations for SDRs geometry. Magenta line is the plate deflection due to one dike load, quantified by equation (1). Green line evolves from the red line and is the deflected SDR that has experienced x_0 amount of plate extension and dike widening, quantified by equation (2). Following the motion of an arbitrary particle (red dot), integrating equation (1) (magenta line) from $\Delta x = x - x_0$ to x gives its current location at $(x, w_s(x))$. The value of $w_s(x)$ is also represented by the shaded area indicated between the magenta line and the X axis. Integrating equation (1) with $\Delta x = x - x_0 = 0$ gives the motion of the blue dot that moves on the dike lava interface (blue line), quantified by equation (3). Here, the distance between the blue and red dots are assumed to be invariant.

Where δw_0 is the maximum deflection at the rifting center, x is the distance away from diking center, α is the flexural wavelength. $\delta w_0 = 2\delta V_0/\alpha g \Delta \rho_s$ where $\delta V_0 = \delta x g h_d \Delta \rho_d$, is the downward load provided by a solidified dike with width of δx , height of h_d and density increase of $\Delta \rho_d = (\rho_d - \rho_f)$, where ρ_f is the density of fluid magma and ρ_d is the density of the solidified dike. g is the gravitational acceleration. $\Delta \rho_s = \rho_i - \rho_c$, is the density difference between the infilling volcanic or sedimentary materials with density of ρ_i and the compensating layer with density ρ_c of lower crust or mantle. Infilling of either lava flow, sediment, water or air provides a spatially variable downward load of $q(x) = \Delta \rho_s g w(x)$. $\alpha = (4D/\Delta \rho_s g)^{1/4}$, where D is flexural rigidity and $D = E T e^3 / 12(1 - \mu^2)$. E is Young's modulus, $T e$ is effective elastic thickness and μ is Poisson's ratio.

In order to keep track of the motion of each SDR due to continuous diking and plate extension, we consider the movement of an arbitrary lava flow particle originally at the surface a distance $\Delta x = x - x_0$ from the axis. As the plate undergoes loading from x_0 amount of repeated dike widening, the particle is translated to a horizontal distance x from the rifting axis, the total amount of subsidence $w_s(x)$ is obtained by integrating the deflection due to one dike load (equation 1) from its initial location Δx to its final location x where

$$w_s(x) = \int_{\Delta x}^x \delta w(x) = w_0 \left\{ e^{-\frac{x}{\alpha}} \left(\sin\left(\frac{x}{\alpha}\right) - \cos\left(\frac{x}{\alpha}\right) \right) - e^{-\frac{x-x_0}{\alpha}} \left(\sin\left(\frac{x-x_0}{\alpha}\right) - \cos\left(\frac{x-x_0}{\alpha}\right) \right) \right\} \quad (2)$$

Here $w_0 = h_d (\Delta \rho_d / \Delta \rho_s)$ is the maximum accumulated downward subsidence due to repeated magmatic loading and lateral translation. It is also the maximum thickness of an SDRs wedge. Using equation 2 we plot the deflection of initial surface points with a range of plate extension x_0 to generate the model SDRs geometry (Figure 3). Note that setting $\Delta x = x - x_0 = 0$ gives the trajectory of the SDR particle that was originally on axis and at the surface:

$$w_t(x) = \int_{\Delta x=0}^x \delta w(x) = w_0 \left\{ e^{-\frac{x}{\alpha}} \left(\sin\left(\frac{x}{\alpha}\right) - \cos\left(\frac{x}{\alpha}\right) \right) + 1 \right\} \quad (3)$$

so that $w_t(x)$ delineates the shape of the dike-SDR interface.

From these simple equations, we derive three geometric parameters that are functions of Te and that we later use to compare model and seismic data. First, we term the distance between the rifting center and the flat dike-lava interface (eq3) as X_f (Figure S1 & 3). We find X_f from Equation 3 where the derivative of $w_t(x)$ with x equals zero at the closest point to the axis as:

$$X_f = \frac{\pi}{2} \alpha \quad (4)$$

By measuring X_f of SDRs from the MCS profile, we estimate α and so can estimate Te with $Te = \{3\alpha^4 \Delta \rho_s g (1 - \mu^2)/E\}^{1/3}$. The advantage of using X_f is its independence of the vertical velocity structure used or assumed in the MCS data. When a SDR experiences X_f amount of extension, the shape of the SDR becomes stable because magmatic loading at the rifting center has little effects on the plate deflection X_f away from the axis.

Second, the ratio γ between the depth $w_s(X_f)$ and the slope $dw_s/dx(X_f)$ of the SDR lava surface at the dike-lava interface, is also a function of α :

$$\gamma = \frac{w_s(X_f)}{dw_s/dx(X_f)} = -\frac{\alpha}{2} \left(1 + \exp\left(-\frac{\pi}{2}\right) \right) \quad (5)$$

Because both w_s and dw_s/dx depend on vertical velocity structure of the lava and sediments, though in different ways, taking the ratio of them might reduce uncertainties. Applying both X_f and γ to the same MCS profile for estimating Te gives us confidence when the difference is less than 30%.

X_f and γ have limitations when the SDRs experienced less than X_f amount of extension. In searching early signals before SDRs evolve to steady state, we found that the difference

between the slope of the dike-SDR interface $k_t = dw_t/dx(x_0)$ and each SDR slope $k_s = dw_s/dx(x_0)$ at the interface ($x = x_0$) is constant as a function of plate strength Te and dike load h_d or two length scales mentioned controlling the analytic model geometry (i.e. w_0 and α) such that :

$$k_t - k_s = \frac{dw_t}{dx}(x_0) - \frac{dw_s}{dx}(x_0) = \frac{2w_0}{\alpha} = \frac{2\Delta\rho_d}{\Delta\rho_s^{3/4}} \left[\frac{E}{3g(1-\mu^2)} \right]^{-\frac{1}{4}} \frac{h_d}{Te^{3/4}} \quad (6)$$

This constant value gives rise to the third observable: the angle ϕ (Figure 3) between the tip of each SDR and the dike-SDR interface. It is related to the gradients by:

$$\tan(\phi) = \frac{k_s - k_t}{1 + k_s k_t} \quad (7)$$

Because dike-SDR interface is relatively flat when a SDR has steep slope and vice versa, $k_s k_t$ is negligibly small in most cases. For simplicity, we approximate $\tan(\phi) \approx k_s - k_t$. As shown in Figure S2, the observable ϕ reflects the relationship between h_d and Te that ϕ increases with a larger dike load and a weaker plate. h_d is limited by the initial crustal thickness. For simplicity, we use upper crustal thickness as the value of h_d along with the measured averaged Te for estimating the angle ϕ . For EP models, the predicted angle ϕ are around $30\text{--}35^\circ$ and are consistent with the model results. For EVP models with constant thermal structure, the predicted angle ϕ ranges from 30° to 43° and are about 10° less than the model results that ranges from 43° to 54° . The torque due to upper crustal root along with viscous relaxation might contribute to this extra SDR rotation. For EVP models with thermal evolution, the angle ϕ prediction are consistent for models without underplating (40° (dry quartz) and 28° (dry plagioclase) vs. 40.1° and 25.7°). Compared to EVP constant thermal models, they have less angle underestimation. The upward thermally eroding lithosphere near rifting center results in a smaller effective dike load h_d and thus reduces the effects from the extra rotation. For EVP

models with thermal evolution, underplating and dry plagioclase rheology, the angle ϕ prediction significantly overestimates by a factor of two (i.e. 25° vs. 12.9°) because of the strong crust-mantle coupling. Whereas for the dry quartz case with weak lower crust, the angle ϕ prediction is closed to the results, counter balanced between effects of extra-rotation and resistance of lava flow subsidence from the underplating materials in the lower crust.

Using these three observables: X_f , γ and ϕ , we can reliably link SDRs geometries from MCS data to the plate strength that supports the SDRs in terms of effective elastic thickness T_e .

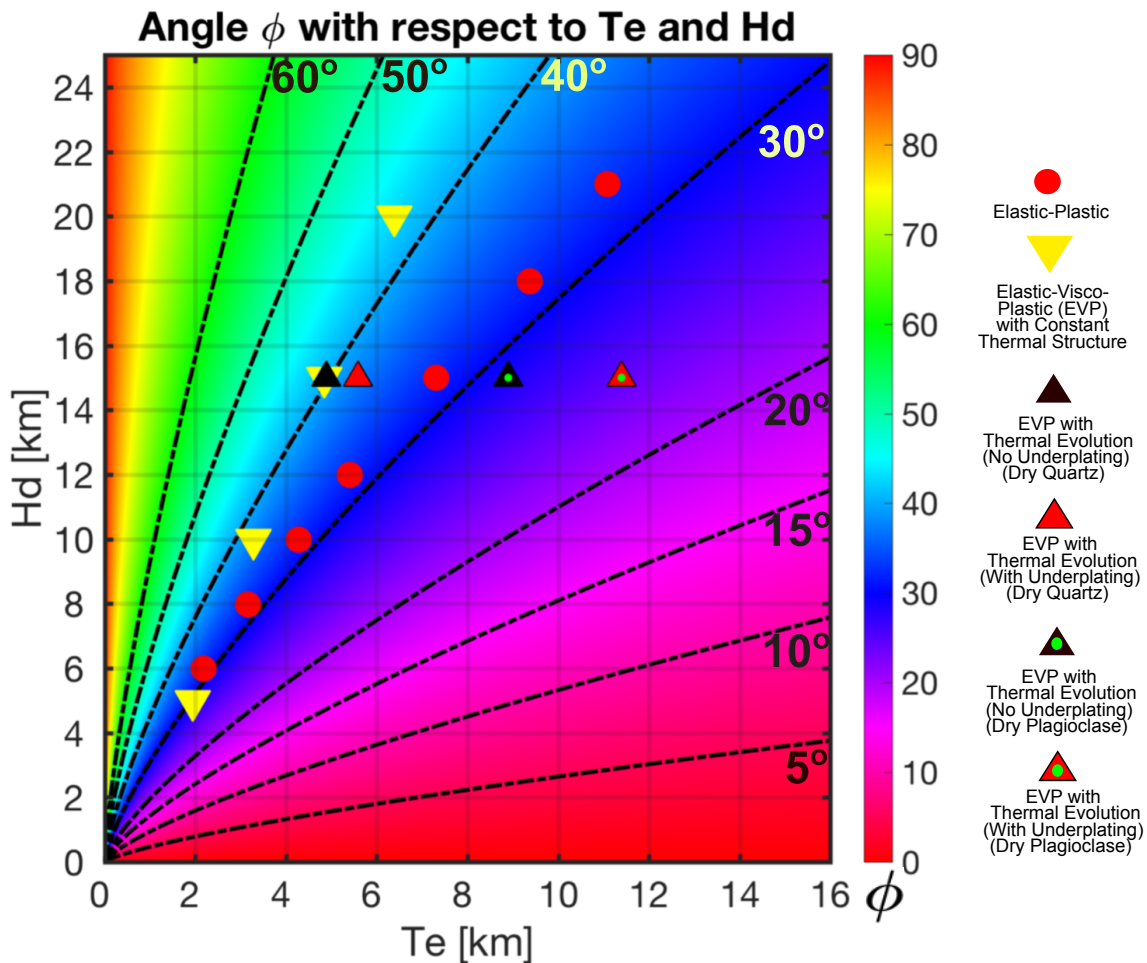


Figure S2. The angle between the tip of each SDR and dike-SDR interface ϕ as a function of h_d and T_e from analytic models. Black dashed lines are contours of ϕ . For pure elastic case with $H_d = T_e$, the model predicts ϕ ranges from 10 to 20 degrees as T_e increases from 1 to 16 km. Different symbols are from 2D FLAC model results.

A1-2. Numerical Thin plate (NTP) description

For spatially restricted lava infill (i.e. fill only up to where the plate deflects beneath the original surface) we numerically solve the fourth order flexure equation and with the implicit finite difference method described below:

Following Turcotte & Schubert, (2002), the 4th-order flexural equation for deflection $w(x)$ of a thin elastic plate under horizontal force P , vertical load $q(x)$, vertical shear stress $V(x)$ and bending moment M is:

$$D \frac{d^4 w(x)}{dx^4} = q(x) - P \frac{d^2 w(x)}{dx^2} \quad (8)$$

Where D is flexural rigidity and $D = Eh/12(1 - \mu^2)$. E is Young's modulus, h is effective elastic thickness and μ is Poisson's ratio. $q(x) = -\delta\rho_s(x)gw(x)$ (negative sign due to downward as positive direction), where g is gravitational acceleration, $\delta\rho_s(x)$ is the density difference between the densities of the substrate or the compensating layer ρ_c (either density of the mantle or the flowing lower crust) and the infilled materials ρ_{in} (either density of the volcanic infill (ρ_i) or the air (ρ_{air})). This general flexural equation for thin elastic plate is achieved by load balance:

$$q(x)dx + dV = 0 \quad (9)$$

along with torque balance:

$$P \frac{dw(x)}{2} \cdot 2 - dM + V \cdot \frac{dx}{2} \cdot 2 = 0 \quad (10)$$

and moment curvature relationship:

$$M = -D \frac{d^2 w(x)}{dx^2} \quad (11)$$

with constitutive equations assuming “thin plate” that $\sigma_{yy} = \varepsilon_{zz} = 0$:

$$\varepsilon_{xx} = -y \frac{d^2 w(x)}{dx^2} \quad (12)$$

$$M = \int_{-\frac{h}{2}}^{\frac{h}{2}} \sigma_{xx} y dy \quad (13)$$

$$\varepsilon_{xx} = \frac{1 - \mu^2}{E} \sigma_{xx} \quad (14)$$

Let's further assume there is no horizontal force ($P = 0$), the general flexural equation reduces to:

$$D \frac{d^4 w(x)}{dx^4} = q(x) \quad (15)$$

Then, further discretize the above equation using finite difference method at point i where $i = 1, 2, 3, \dots, N$ and N is the total number of points, Δx is the grid size of the model and w_n is the discretized counterpart of $w(x)$:

$$D \frac{1}{\Delta x^4} (w_n(i+2) - 4w_n(i+1) + 6w_n(i) - 4w_n(i-1) + w_n(i-2)) + \delta\rho_s(x) g w_n(i) = 0 \quad (16)$$

with distributed load assuming at where $w(x)$ has a downward deflection:

$$\delta\rho_s(x) = \rho_c - \rho_i \quad (17)$$

and when $w(x)$ has an upward or zero deflection (assuming $\rho_{air} = 0$):

$$\delta\rho_s(x) = \rho_c - \rho_{air} = \rho_c \quad (18)$$

In addition, we assume either broken plate boundary conditions (BCs):

BC1:

$$w(\infty) = 0 \leftrightarrow w_n(N) = 0 \quad (19)$$

BC2:

$$w'(\infty) = 0 \leftrightarrow w_n(N-1) = w_n(N) \quad (20)$$

BC3:

$$\begin{aligned} M(0) &= -D \frac{d^2 w(x)}{dx^2}(0) = 0 \\ \leftrightarrow \quad (w_n(i+1) - 2w_n(i) + w_n(i-1)) / \Delta x^2 &= 0 \end{aligned} \quad (21)$$

BC4:

$$V(0) = \frac{dM}{dx}(0) = -D \frac{d^3 w(x)}{dx^3} = \delta \rho_d g h \quad (22)$$

Where $i = 3$ to reach the leftmost grid point and because $\frac{d^3 w_n}{\Delta x^3}(i-0.5) = \left\{ \frac{d^2 w_n}{\Delta x^2}(i) - \frac{d^2 w_n}{\Delta x^2}(i-1) \right\} \frac{1}{\Delta x} = \{w_n(i+1) - 3w_n(i) + 3w_n(i-1) - w_n(i-2)\} / \Delta x^3$ and where $\delta \rho_d$ is the density difference between fluid (ρ_f) and solidified (ρ_d) dike and h is the height of the dike and is assumed to be the same as the effective elastic thickness.

Otherwise, for continuous plate boundary conditions BC1, BC2 and BC4 are exactly the same as broken plate boundary condition, BC3 differs in:

$$\frac{dw}{dx}(0) = 0 \leftrightarrow w_n(1) = w_n(2) \quad (23)$$

Based on the above discretization, an inverse problem of:

$$\mathbf{Gm} = \mathbf{d} \quad (24)$$

is set up. Where \mathbf{G} is an N by N matrix of the coefficients of deflections w_n , \mathbf{m} is the N by 1 vector for N points of deflections w_n and \mathbf{d} is the N by 1 vector of the right-hand side. Applying the finite difference method with discretization described above, the coefficients matrix can be found for $w_n(i+2), w_n(i+1), w_n(i), w_n(i-1), w_n(i-2)$ as following:

when j (row index for \mathbf{G}) varies from 1 to $N - 4$, the remaining four rows are padded with the four BCs:

for ($i = j$):

$$\mathbf{G}(j, i) = 1 \quad (25)$$

for ($i = j + 1$):

$$\mathbf{G}(j, i) = -4 \quad (26)$$

for ($i = j + 2; w_n(i) < 0$):

$$\mathbf{G}(j, i) = 6 + \delta\rho_s g \frac{\Delta x^4}{D} \quad (27)$$

for ($i = j + 2; w_n(i) \geq 0$):

$$\mathbf{G}(j, i) = 6 + \rho_c g \frac{\Delta x^4}{D} \quad (28)$$

for ($i = j + 3$):

$$\mathbf{G}(j, i) = -4 \quad (29)$$

for ($i = j + 4$):

$$\mathbf{G}(j, i) = 1 \quad (30)$$

The remaining four rows when j varies from $N - 3$ to N are used to apply the four BCs mentioned above. The other entries of the G matrix are all zeros. The vector \mathbf{d} is all zero except for either one of the last four rows (say $i = N$) is used to apply BC4 where $d(N) = \delta\rho_d g h$.

Solution to deflection w_n is obtained by solving:

$$\mathbf{m} = \mathbf{G}^{-1} \mathbf{d} \quad (31)$$

In addition, we allow couple iterations with updated distributed $q(x)$ based on the calculated $w(x)$ until the solution converges to a stable profile. Once it reaches the stable solution of $w(x)$, we numerically integrate $w(x)$ following steps of (Buck, 2017) or equations 1-

3 to get the dike-SDR interface and SDRs experience different amount of extension and loading.

The NTP results and its quantitative comparison with ATP models are shown in Figure 3.

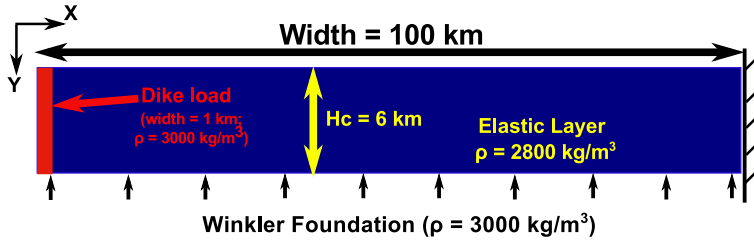
A1-3. Tracer implementation in FLAC

The 2D numerical models are calculated using a rectangular grid with a grid spacing of 1 km. In order to obtain an accurate estimate of the SDR geometry we deploy 600 tracers every million year (a line of constant infill age) at the surface of the first half of the model domain so as to track the temporal evolution of the tops of particular model lava flows. To do this we wrote two new subroutines to the original version of FLAC: particle_seed.f90 that initiates and deploy the tracers at the onset of model running and particle_move.f90 that describes how the tracers should move along with 7 other files being modified accordingly.

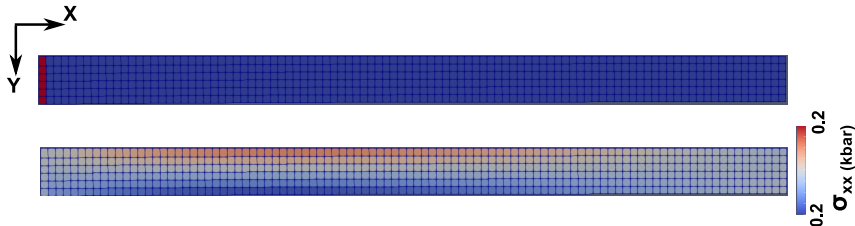
The location of each tracer is recorded as a function of time. During each model time step, we first find which quadrilateral grid element the tracer belongs to. Each grid element is subdivided into four triangular regions. We then find the region that the tracer is in. We then apply barycentric interpolation to calculate the velocity of the tracer from the node points of the triangles it belongs to. Finally, we update the tracer's location by integrating the tracer's velocity with model time step. Iteratively doing so, we could update all the tracers' location with time (e.g. Figure 7a).

A1-4. Benchmark between FLAC models and NTP models

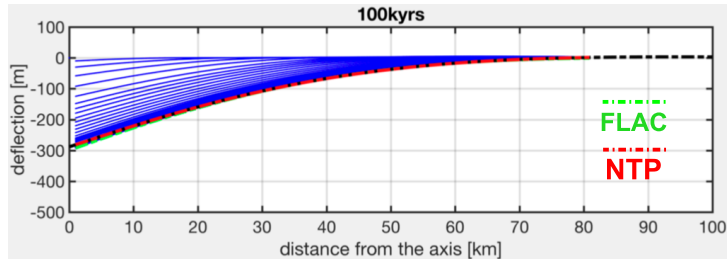
a. Model Setup



b. Elastic Thick Plate Benchmark model results



c. Model surface deflection



d. Model Convergence:

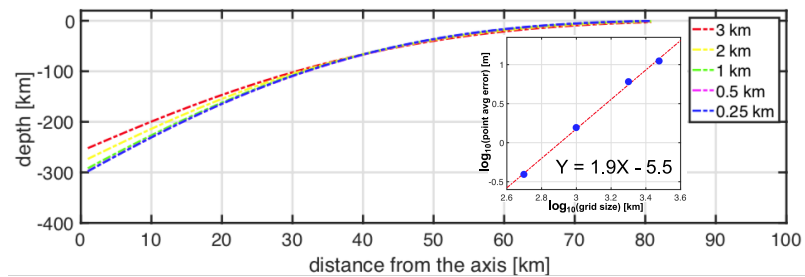
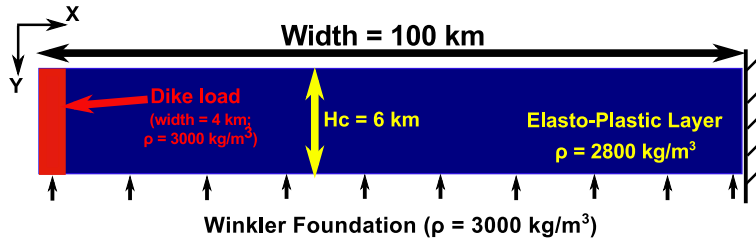


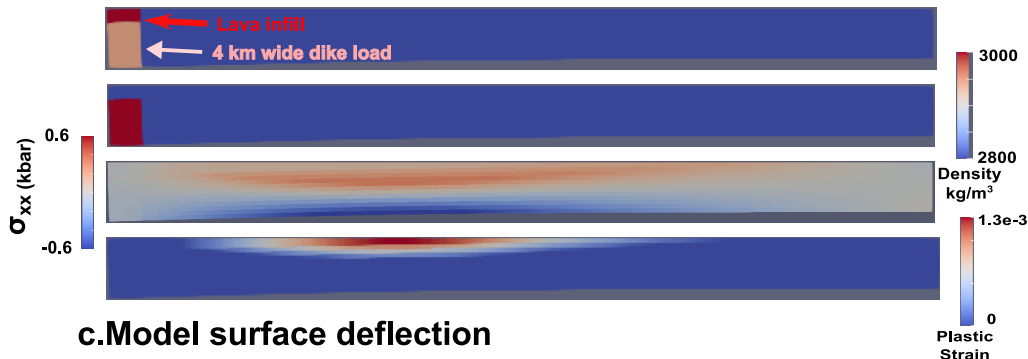
Figure S3. Elastic thick plate model benchmark. a. Model setup: Elastic thick plate benchmark with restricted lava infill. Model domain is 6 km thick and 100 km wide. Supported by Winkler foundation of density 3000 kg/m^3 . The left boundary can freely move and the right boundary is fixed. The layer is elastic with density of 2800 kg/m^3 . The dike has a density of 3000 kg/m^3 and provide a downward load at the rift axis. b. Elastic thick plate benchmark results: The phase and horizontal deviatoric stress at 100 kyr of model time. Positive stress means extensional. c. The locations of the SDR tracers are plotted on top of the numerical thin plate solution. The blue lines are SDR tracers with different model times with an interval of 1 kyr. The green line is the final steady state SDR reached at ~20 kyr. The

red line is the result from numerical thin plate solution. d. Model convergence shows that 1 km of grid size is optimized when considering both accuracy and computation time. Steady state deflection with different grid sizes. Inset shows the point averaged difference compared to the model with the highest resolution of 0.25 km grid size.

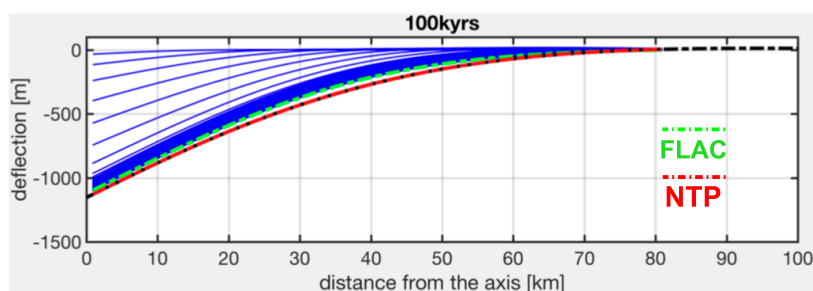
a. Model Setup



b. Elasto-Plastic Thick Plate Benchmark Results



c. Model surface deflection



d. Model Convergence:

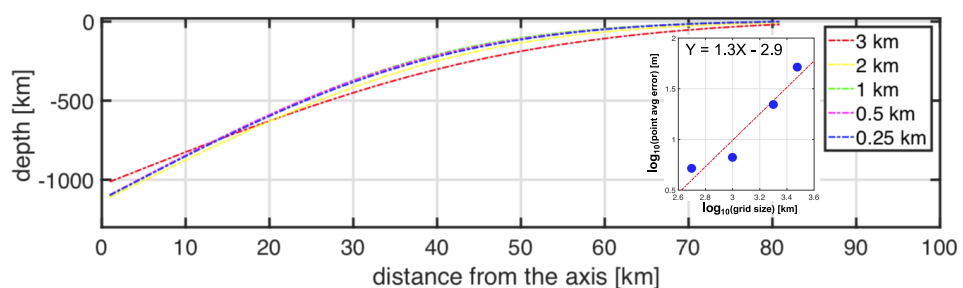


Figure S4. The same as Figure S3 except for the Elasto-Plastic rheology.

Parameter names	Value	Unit
Model Width	100	km
Model Thickness	6	km
Dike height	6	km
Dike width	1	km
Lamé constant (λ)	30	GPa
Lamé constant (μ)	30	GPa
Crustal density	2800	kg/m^3
Dike density	3000	kg/m^3
Lava infill density	2800	kg/m^3
Substrate density	3000	kg/m^3
# particles for SDR tracer	600	N/A
Gravitational acceleration (g)	10	m/s^2

Table S1. FLAC model parameters for elastic plate.

Parameter names	Value	Unit
Model Width	200	km
Number of node points	2001	N/A
Height of dike	6	km
Te	6	km
Gravitational acceleration (g)	10	m/s^2
Young's modulus	75	GPa
# iteration	10	N/A
Crustal density	2800	kg/m^3
Dike density	3000	kg/m^3
Lava infill density	2800	kg/m^3
Substrate density	3000	kg/m^3

Table S2. Numerical thin plate model parameters.

A1-5. The published MCS profiles used for calculating the Te based on the SDRs geometries

For processing the depth-converted MCS profiles from published papers, we measure the X_f , γ .

Then we can calculate the corresponding Te for each profile.

Fig.1

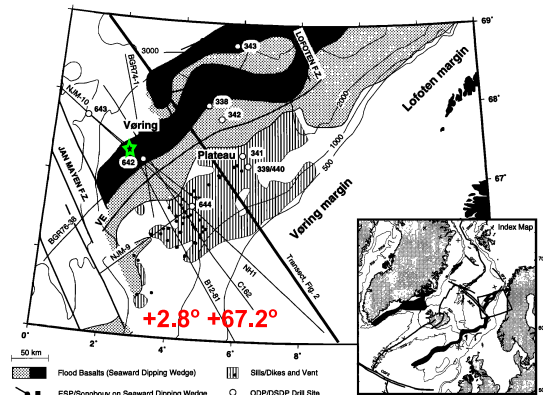


Figure 1. Early Tertiary igneous units and main structural elements on Voring margin, based on Skogseid and Eldholm [1989]. MCS profiles in the vicinity of ODP Site 642 are shown. Index map shows in black extent of the seaward dipping wedge and onshore flood basalts in the North Atlantic [Eldholm and Grue, 1994]. Bathymetry in meters. ESP, expanding spread profile; VE, Voring Escarpment; CGFZ, GFZ, JMFZ, SFZ, Charlie-Gibbs, Greenland, Jan Mayen and Senja Fracture zones, respectively.

Fig.10 VE 3

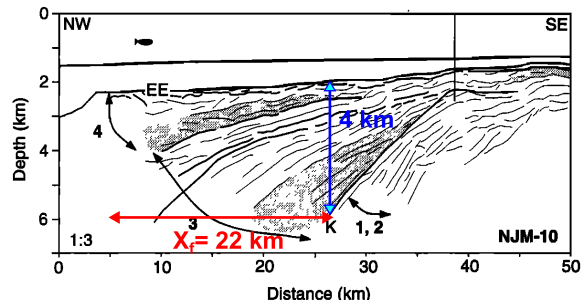
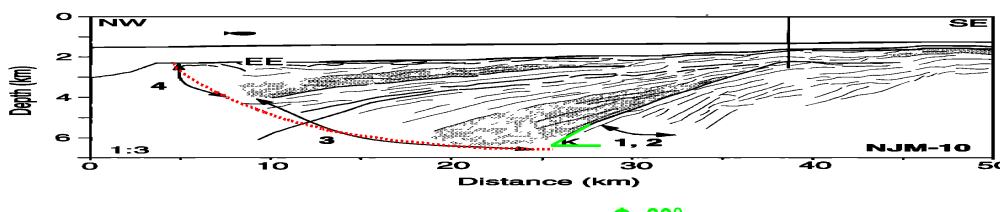


Fig. 10 VE1



$$\Phi = 29^\circ$$

Planke and Eldholm JGR 1994 fig. 10

$$+2.8^\circ +67.2^\circ$$

$$X_f = 22 \text{ km}$$

$$W_s(X_f) = 4.0 \text{ km}$$

$$\Phi = 29^\circ$$

$$T_e_{xf} = 1424 \text{ m}$$

$$\alpha_{xf} = 14006 \text{ m}$$

$$T_e_y = 1152 \text{ m}$$

$$\alpha_y = 11949 \text{ m}$$

$$T_e_{avg} = 1288 \text{ m}$$

$$\alpha_{avg} = 12977 \text{ m}$$

$$T_e_{err} = +19\%$$

$$H_d = 3600 \text{ m (from } \Phi \text{ and } T_e_{avg})$$

Figure S5. Adapted from (Planke & Eldholm, 1994).

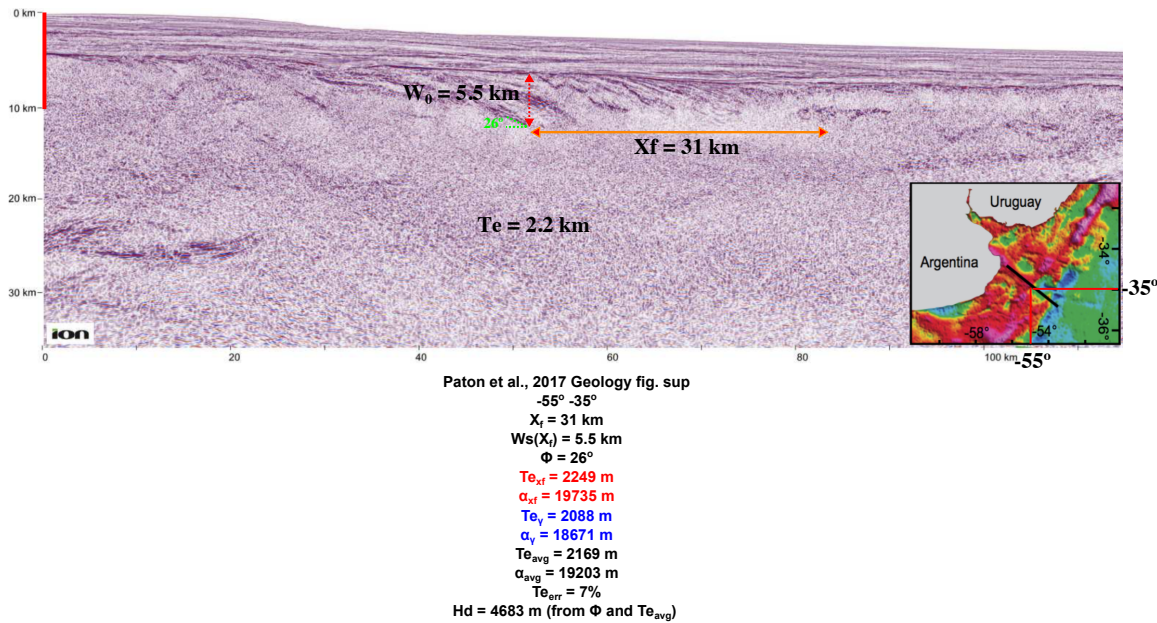


Figure S6. Adapted from (Paton et al., 2017).

A1-References:

- Bodvarsson, G., & Walker, G. P. L. (1964). Crustal Drift in Iceland. *Geophysical Journal of the Royal Astronomical Society*, 8(3), 285–300. <https://doi.org/10.1111/j.1365-246X.1964.tb06295.x>
- Buck, W. R. (2017). The role of magmatic loads and rift jumps in generating seaward dipping reflectors on volcanic rifted margins. *Earth and Planetary Science Letters*, 466, 62–69. <https://doi.org/10.1016/j.epsl.2017.02.041>
- Morgan, R., & Watts, A. (2018). Seismic and gravity constraints on flexural models for the origin of seaward dipping reflectors. *Geophysical Journal International*, 214(3), 2073–2083. <https://doi.org/10.1093/gji/ggy243>
- Paton, D. A., Pindell, J., McDermott, K., Bellingham, P., & Horn, B. (2017). Evolution of seaward-dipping reflectors at the onset of oceanic crust formation at volcanic passive margins: Insights from the South Atlantic. *Geology*, G38706.1. <https://doi.org/10.1130/G38706.1>
- Planke, S., & Eldholm, O. (1994). Seismic response and construction of seaward dipping wedges of flood basalts: Vøring volcanic margin. *Journal of Geophysical Research: Solid Earth*, 99(B5), 9263–9278. <https://doi.org/10.1029/94JB00468>
- Turcotte, D. L., & Schubert, G. (2002). *Geodynamics*. Cambridge: Cambridge University Press. <https://doi.org/10.1017/CBO9780511807442>

Watts, A. B., & Cox, K. G. (1989). The Deccan Traps: an interpretation in terms of progressive lithospheric flexure in response to a migrating load. *Earth and Planetary Science Letters*, 93(1), 85–97. [https://doi.org/10.1016/0012-821X\(89\)90186-6](https://doi.org/10.1016/0012-821X(89)90186-6)

Chapter 2: How Intrusion and Crustal Flow Control the Topography of Continental Large Igneous Provinces*

The Ethiopian and Columbia Plateaux are the surface expressions of the two youngest Large Igneous Provinces. The Ethiopian Plateau is on average ~1.5 km higher than its peripheries whereas the average elevation within the Columbia plateau is ~0.7 km lower than its surroundings. A simple semi-analytic model using the thin-channel approximations allow us to estimate the effect of lower crustal flow on expected plateau topography for a wide range of crustal rheologies and geotherms. When the crustal flow rates are smaller than a critical level a long-lived high plateau results no matter the style of intrusion. A low plateau can form as a result of moderately fast lower crustal flow, with a significant fraction of intruded material that is mechanically attached to the strong upper crust. These attached upper crustal loads pull the surface down to produce a low elevation plateau. We then employ a two-dimensional numerical thermal-mechanical model to more realistically simulate the crustal magma intrusion processes and quantify their effects on plateau topography. Intrusion is simulated by addition of materials with basaltic density and rheological properties as thickening sills. The depth of each sill intrusion is based on the evolving crustal thermal, rheological and density structures. For an initial crustal geotherm estimated for average continental crust these models predict that magma intrusions lead to thickening of the buoyant crust and plateau uplift that persists for tens of

* This chapter is in preparation for submission to the Journal of Geophysical Research.

millions of years, as seen for Ethiopia. In contrast, for hotter geotherms, the loads of denser mafic intrusions in the upper crust drive sufficient lateral lower crustal flow to accommodate surface subsidence and generate a bowl-shaped basin. Assuming that the main phase of flood basalt eruptions occurs only when the average density for the crust above the sill exceeds the density of the fluid magma, the model can reproduce the synchronous subsidence and flood basalt extrusion inferred for the Columbia Plateau.

2.1 Introduction

Large igneous provinces (LIPs) form when voluminous magma ($\sim 10^6 \text{ km}^3$) is emplaced as crustal intrusions and lava flows within a relatively short time ($<\sim 1 \text{ Myrs}$) (e.g. Bryan & Ferrari, 2013; Coffin & Eldholm, 1994). Their formation contributes to the initiation of continental rifting (Buck, 2006; Courtillot et al., 1999) and correlates with climatic excursions and mass extinctions (Courtillot & Renne, 2003; Jones et al., 2016; Wignall, 2001). LIPs span the Earth's Phanerozoic history and are of global significance (Bryan & Ernst, 2008), shaping a great portion of the Earth's surface topography and near-surface structures of nearly every continent and ocean by adding voluminous basaltic rocks either as flood basalt lava flows onto continental and oceanic regions or as mafic intrusions within the crust. Examples of continental flood basalt provinces include the Siberian plateau in Central Asia, the Deccan plateau in South Asia, the Ethiopian plateau in Africa, and the Columbia plateau in North America. There are basaltic oceanic plateaus including the Ontong Java plateau in the Pacific Ocean, the Rio Grande Rise in the Atlantic Ocean or the Kerguelen Plateau in the Indian ocean. Many rifted continental margins associated with subaerial LIPs are characterized by buried but subaerially emplaced massive volcanic lava flows seismically imaged as seaward dipping reflectors (Tian & Buck, 2019 and references therein).

As the Earth's topography is constantly being reshaped by surface erosion, the older the plateau, the stronger the modifications by surface processes. Here we focus on studying how LIP formation affects the topography of the two youngest and hence best-preserved continental flood basalt provinces: the Columbia Plateau (CP) that formed in the Miocene and the Ethiopian Plateau (EP) that formed in the Oligocene, with a main phase of flood basalt volcanism happening around 17 Ma (Kasbohm & Schoene, 2018) and around 30 Ma (Hofmann et al., 1997; Rooney et al., 2018) respectively. Despite their commonalities as the two youngest continental LIPs, they have distinctly different surface topographies: the EP has an average ~1.5 km bulge with radius of about 600 km (Figure 1a, c) whereas the CP shows a bowl-shape topography with a radius of about 200 km and a central depression of ~0.7 km (Figure 1b, d).

Local isostatic compensation of magmatic thickening of the crust should result in a high plateau, so the formation of a low plateau is harder to understand. Two ideas for the formation of low elevation magmatically intruded crust involve density anomalies in either the crust or the mantle. Perry-Houts & Humphreys (2018) propose that a phase change from lower crustal basaltic underplates to dense eclogite drives subsidence and results in the low elevation of the Columbia Plateau. Sobolev et al., (2011) call on a mantle plume with anomalous composition of dense recycled oceanic crust to explain the lack of geological evidence of pre-magmatic uplift during the formation of the Siberian Traps. A simpler idea for the subsidence of the volcanic-covered Eastern Snake River Plain was advanced by McQuarrie & Rodgers, (1998). They suggested that lower crustal flow in response to the loads of crustal intrusion results in lower surface elevation compared to the surrounding crust.

In this paper we investigate how lower crustal flow could affect the elevation of volcanic plateaux. Specifically, we study how different crustal thermal and rheological conditions at the

time of a LIP formation affect volcanic plateau elevation. Since seismic and petrologic data indicate that around 3 to 16 times more magma is intruded as is extruded during LIP formation (Coffin & Eldholm, 1994; Crisp, 1984; Ridley & Richards, 2010; Moore et al., 2018), we focus on how magma might be intruded. We first consider a semi-analytic model of magmatic loading in which we use a thin channel approximation to simplify the treatment of lower crustal flow. Then, we describe results from a fully two-dimensional model of magma intrusion and crustal deformation.

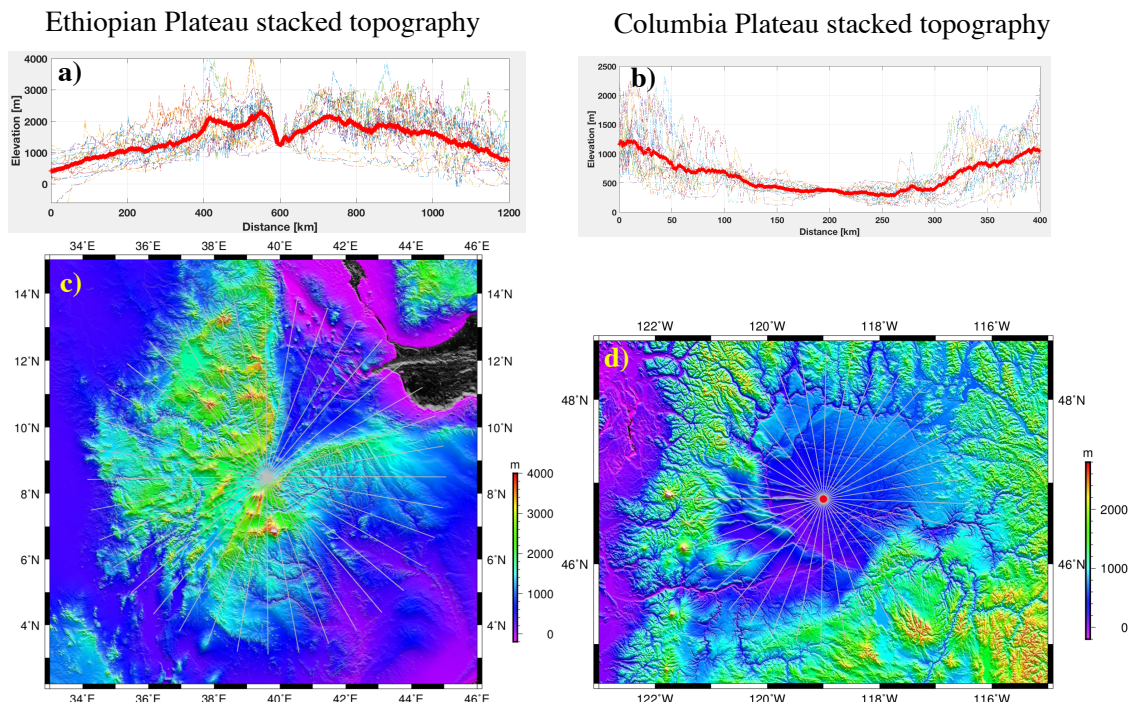


Figure 1. Digital Elevation Models (DEM) for Ethiopian Plateau (EP) (East Africa; a and c) and Columbia Plateau (CP) (West US; b and d) [Model data source: 15 arc second global relief (SRTM15+); resolution: ~500m; [url:<http://gmt.soest.hawaii.edu/doc/latest/datasets.html>](http://gmt.soest.hawaii.edu/doc/latest/datasets.html)].
Colorful dashed lines in a) and b) and grey lines in c) and d) are 36 topographic profiles centered at points 39.6E/8.5N (EP) and 119W/46.8N (CP). Each profile is 1200 km (EP) and 400 km (CP) long, spaced with 10 degrees clockwise rotation and sampled every ~200 meters along the profile. Bold red lines in a) and b) are the mean of all stacked profiles. c) Topography map for Ethiopian Plateau from the DEM models. d) Topography map for Columbia Plateau from the DEM models.

2.2 Models and Results:

We describe here a sequence of models starting from a simple qualitative and schematic model to a quantitative two-dimensional thermo-mechanical model with a limited number of assumptions. From the simple schematic model, we consider how strength of the lower crust might control volcanic plateau topography resulting from crustal magma emplacement. We then formulate a semi-analytic model to quantify the effects of variable thermal-rheological conditions on lower crustal flow and the development of volcanic plateau topographies. Finally, based on a narrower parameter space constrained by the semi-analytic models, we employ a fully 2D thermo-mechanical model to more realistically simulate the process of intrusion, crustal flow and topography development.

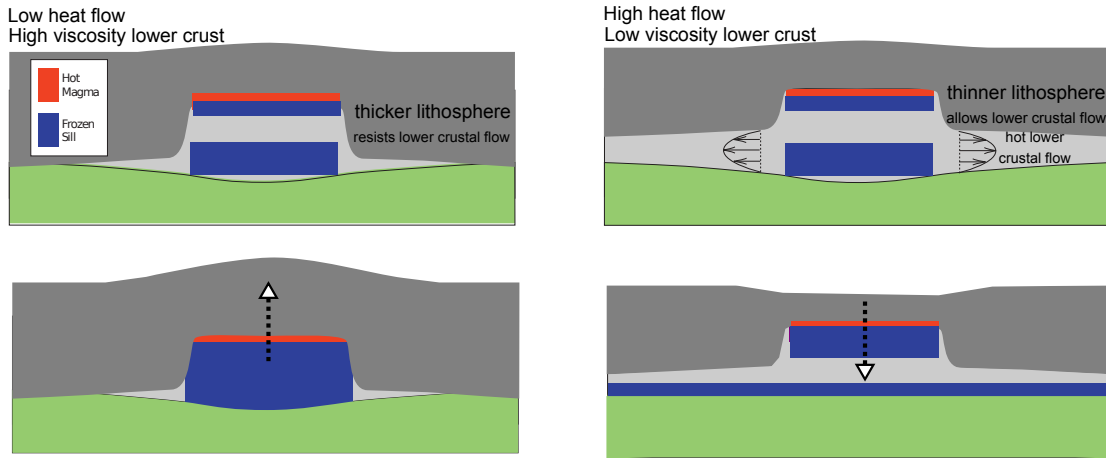
It should be noted that, in addition to crustal magma emplacement, the presence of hot, low-density mantle beneath the plateau crust could also contribute significantly to the high topography of the Ethiopian Plateau (Ebinger et al., 1989). However, as we will show below, with sufficient lower crustal flow, high plateaux should not persist regardless of their cause.

The idea that basaltic intrusion could drive lower crustal flow was treated by McQuarrie & Rodgers (1998) to explain the subsidence of the East Snake River plain. Their model assumes that lower crustal flow has reached a steady-state lower crustal configuration (i.e. lateral pressure gradients in the lower crust are zero) and considers the flexure response given certain rectangular intrusive loads. For our purpose of quantifying effects of crustal thermo-rheological conditions on the evolution of topography, however, it is important to include temporal evolution in the lower crustal flow calculations and we do so below.

2.2.1 Schematic model

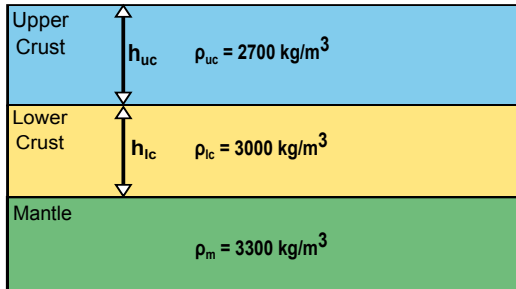
Our schematic model illustrates the importance of thermally controlled crustal viscosity structure and lower crustal flow during the development of volcanic plateau topography (Figure 2a). By considering extreme cases, we can estimate whether reasonable volumes of basalt intruded into continental crust could produce the observed magnitudes of high and low plateau elevations. We assume only part of all intruded basaltic magma attaches mechanically to the upper crust that is too strong to flow significantly on any timescale of interest. The fact that basaltic material is less dense than the underlying mantle means that addition of basaltic intrusive to the crust can generate a high plateau as long as the lower crust is too cold and strong to flow laterally (Figure 2a left). However, if the lower crust can flow significantly on a timescale that is short compared to the age of the plateau then a low plateau can result (Figure 2a right). This low plateau requires that the mechanically-attached intrusions are denser than the upper crust at the level of intrusions.

a. Schematic model concept:

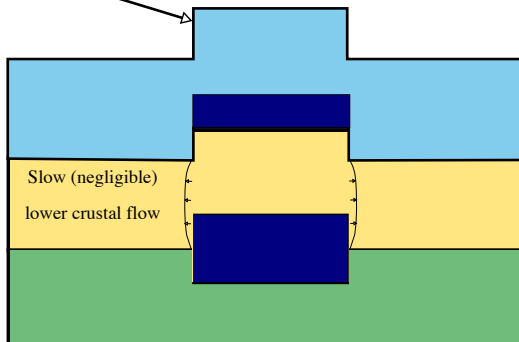


b. Schematic model end-member cases results:

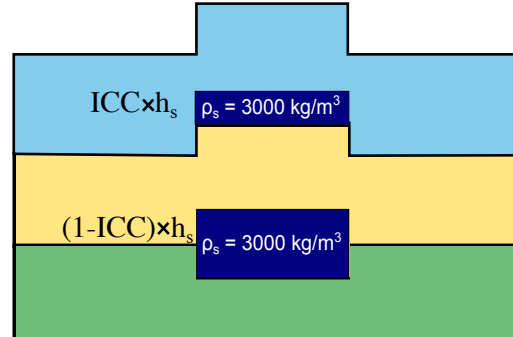
Original Crust and Mantle:



For $\Delta w = 1.5 \text{ km}$; $h_s = 16.5 \text{ km}$



Thickened Crust After Initial Intrusion:



For $\Delta w = -0.7 \text{ km}$; $ICCxh_s = 7.0 \text{ km}$

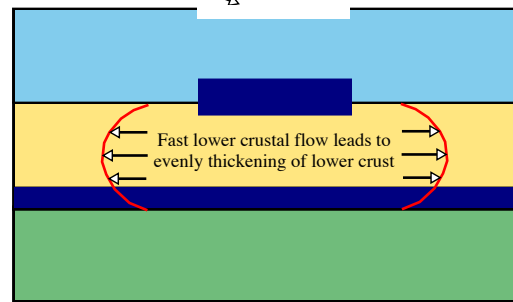


Figure 2. Schematic models. a): Intrusions of dense mafic magma into felsic crust can produce high versus low elevation plateaus depending on the initial thermal and viscosity states of the crust. The dark grey color represents mechanically strong lithosphere. The light grey color represents a low viscosity region that allows fast lateral crustal flow. The green color represents the mantle. **b):** Steady-state results for end-member cases. h_{uc} , h_{lc} , h_s are the thickness of the upper, lower crust and sill intrusions, ICC is the intrusion coupling coefficient (the percentage of the total sill thickness that is able to attach to the upper crust), and Δw is the topographic offset.

To quantify the possible plateau topography, we need to assume crust, mantle and intrusive densities. Here we assume local isostasy and consider a simple initial layered density structure with upper and lower crustal densities $\rho_{uc} = 2700 \text{ kg/m}^3$, $\rho_{lc} = 2700 \text{ kg/m}^3$ mantle density $\rho_m = 3300 \text{ kg/m}^3$ and intrusive density $\rho_s = 3000 \text{ kg/m}^3$ (Figure 2b). For cold and high viscosity crust with negligible crustal flow, sill intrusions of total thickness h_s would cause thickening of the buoyant crust and a sustained surface uplift of $\Delta w = h_s (1 - \frac{\rho_s}{\rho_m})$. Thus, to produce 1.0 km of positive elevation requires that $h_s = 11 \text{ km}$ (Figure 2b left). However, for hot and low viscosity lower crust with ‘complete’ lower crustal flow that results in a flat Moho, sill intrusions would result in surface depression of $\Delta w = -\text{ICC} \times h_s (1 - \frac{\rho_c}{\rho_s})$. In this case, to cause subsidence of the surface with $\Delta w = -0.7 \text{ km}$ requires that $\text{ICC} \times h_s = 7.0 \text{ km}$ (Figure 2b right).

2.2.2 Semi-analytic model

Two things are likely to complicate the simple end-member cases described above: (1) partial attachment of dense intrusives to the strong upper crust; and (2) lateral flow of lower crust. The first of these is particularly complex and depends on the mechanics that control the depth at which intrusion occurs. We address this problem in the next section using thermo-mechanical models. Here, we assume that only a fraction ICC of intrusions fully attach to strong upper crust above a low viscosity lower crust. Intrusions in the upper crust provide a downward load which results in a local increase of pressure in the lower crust. The resulting pressure gradients drive lateral flow of the lower crust. To quantify the effects of variable initial thermal and rheological conditions on lower crustal flow and a range of volcanic plateau sizes, we use a one-dimensional (1D) thin-channel approximation to model the lower crustal flow, similar to that

used in numerous previous studies (e.g. Bird, 1991; Buck, 1991; Clark & Royden, 2000; Husson & Sempere, 2003).

A mafic sill intruding felsic crust is likely to alter the crustal compositional and density structure in a complex way. The crust can be partially melted and thus altered, and the intruded material may fractionate, with denser minerals separating from the liquid residue and possibly flowing downward into the deeper crust. For simplicity we assume a two-layer density structure of the crust with upper crustal density ρ_{uc} being less than the density of solidified sill ρ_s and the lower crust having a density ρ_{lc} equal to that of the solid sill (Figure 2b). A fraction ICC of the total thickness of intrusion alters the upper crust to give it a density equal to the sill density.

For sills that densify the upper crust and thicken the crust, the intrusion thickening of the crust results in a lateral lower crustal pressure gradient:

$$\frac{\partial P}{\partial x} = g\Delta\rho^* \frac{\partial h}{\partial x} \quad (1)$$

Where h is the total crustal thickness including the intruded material of thickness h_s , and $\Delta\rho^* = \frac{\rho_{lc}(\rho_m - \rho_{lc})}{\rho_m}$. To simulate the effects of lower crustal flow in response to this pressure gradient we first consider the standard cartesian derivation for channel flow and then modify it for the radial geometry that is more suitable to our problem. Following Buck, (1991) (see complete derivation in the Appendix), the temporal variation of crustal thickness $h(x)$ and topography is related to the flux $Q(x)$ of the lateral lower crustal flow as:

$$\frac{\partial h}{\partial t} = -\frac{\partial Q}{\partial x} \quad (2)$$

The flux $Q(x)$ is can be related to lateral pressure gradients and thermal and rheological parameters of the lower crust as:

$$Q(x) = -\frac{\partial P}{\partial x} \frac{y_0^3}{\eta_0} \quad (3)$$

where the Newtonian viscosity at the base of the crust is

$$\eta_0 = C \exp\left(\frac{E}{RT_m}\right) \quad (4)$$

C is a pre-factor determined by material properties, E is the activation energy, R is the gas constant and T_m is the temperature at the Moho. The length scale for viscosity changes is:

$$y_0 = \frac{RT_m^2}{E \partial T / \partial y} \quad (5)$$

where $\partial T / \partial y$ is an assumed linear thermal gradient near the base of the crust. Combining equations 1-5 we get a simple diffusion equation for the evolution of crustal thickness:

$$\frac{\partial h}{\partial t} = \kappa_f \frac{\partial^2 h}{\partial x^2} \quad (6)$$

where the effective channel flow diffusivity for the lower crust is $\kappa_f = \frac{\Delta\rho^* g y_0^3}{\eta_0}$.

Derivation of equation 6 is based on a two-dimensional cartesian cross-section of the crust. It is natural to consider that sills intrude as axis-symmetrical thin but wide pancake-shaped bodies. We then assume radial symmetry in pressure and flow fields. This implies that there is no pressure gradient or flux in the cross-radial direction (i.e. tangential to the circumference). All fluxes are parallel to the radius. Given this new assumption, equation (2) changes to:

$$Q(r) = -\frac{\partial P}{\partial r} \frac{y_0^3}{\eta_0} \times 2\pi r \quad (7)$$

where r is the distance from the center of symmetry.

Relating radial channel flow to topography in a ring from r to $r + dr$ using mass conservation, equation 1 becomes:

$$\frac{\partial h}{\partial t} = -\frac{\partial Q}{\partial r} \frac{1}{2\pi r} \quad (8)$$

Because the cartesian horizontal pressure gradient plays the same role as the radial pressure gradient we can write the radial version of equation 6:

$$\frac{\partial h}{\partial t} = \kappa_f \left(\frac{\partial^2 h}{\partial r^2} + \frac{1}{r} \frac{\partial h}{\partial r} \right) \quad (9)$$

Solving equation 9 with a numerical finite difference method yields temporal evolution of crustal thickness h . Assuming local isostasy, surface topography change $w(x)$ can be calculated from crustal thickness $h(x)$ and sill thickness in the upper crust $ICC \times h_s(x)$ as:

$$w(x) = \frac{\rho_m - \rho_{lc}}{\rho_m} [h(x) - h_0] - \frac{\rho_s - \rho_{uc}}{\rho_{uc}} ICC \times h_s(x) \quad (10)$$

where h_0 is the initial uniform crustal thickness before intrusion and h_s is the total amount of intruded sill thickness.

Equation 9 shows that the effective diffusivity for lower crustal flow, κ_f , is a key parameter that represents the combined effects of crustal density and rheology. These effects should govern the rate of lower crustal flow and therefore how plateau topography develops in time. Meanwhile, equation 4 and 5 show that Moho temperature T_m and temperature gradients control both y_0 and η_0 , which determine κ_f . Hence, here we only vary Moho temperature T_m and geometric parameters (e.g. the crustal thickness, the model domain length L and the sill width W_s) while keeping other parameters fixed for all the cases considered. We assume upper and lower crustal densities $\rho_{uc} = 2700 \text{ kg/m}^3$, $\rho_{lc} = 3000 \text{ kg/m}^3$ a mantle density $\rho_m = 3300 \text{ kg/m}^3$ and an intrusive density $\rho_s = 3000 \text{ kg/m}^3$. The temperature gradient is set to be 30 K/km at the Moho. The crustal rheological parameters are those experimentally determined

for wet quartzite (Kronenberg & Tullis, 1984) with activation energy $E = 134 \text{ kJ/mol}$, pre-factor $C = 3.1 \times 10^{11} \text{ Pa}\cdot\text{s}$ and gas constant $R = 8.31 \text{ J}/[\text{mol}\cdot\text{K}]$ in equation 3.

By easily calculating topographic profiles with many different combinations of variables the semi-analytic models allowed us to effectively narrow the parameter space for generating the observed plateau topography. We found model length $L=200\text{km}$, sill radius $W_s = 130 \text{ km}$ and intrusion flux of 3.2 cm/yr lasting for 1 Myr best describes the CP system while $L=700 \text{ km}$, $W_s = 480 \text{ km}$ and intrusion thickening rate of 3.2 cm/yr lasting for 1 Myrs works best for the EP system. We assume $\text{ICC} = 0.2$ for all model cases. We use elevation difference (Δw) between the center and the edge of the plateau as the main model output to compare to the observations. Figure 3e shows the final Δw at 5 Myrs for model cases with different values of the Moho temperature T_m and fixed model length L and sill radius W_s . For both CP and EP model widths, the model results share similar trends. For low values of Moho temperature T_m , lower crustal flow is restricted and hence high plateau topography can be maintained for tens of million years. Low plateaux (or basins) form as for $T_m > 1037 \text{ }^\circ\text{C}$ for the CP system and $T_m > 1169 \text{ }^\circ\text{C}$ for the EP system. EP model setups with wider sills require hotter and lower viscosity lower crust to accommodate the more voluminous crustal addition from intrusion in order to produce a low elevation plateau (i.e. a basin).

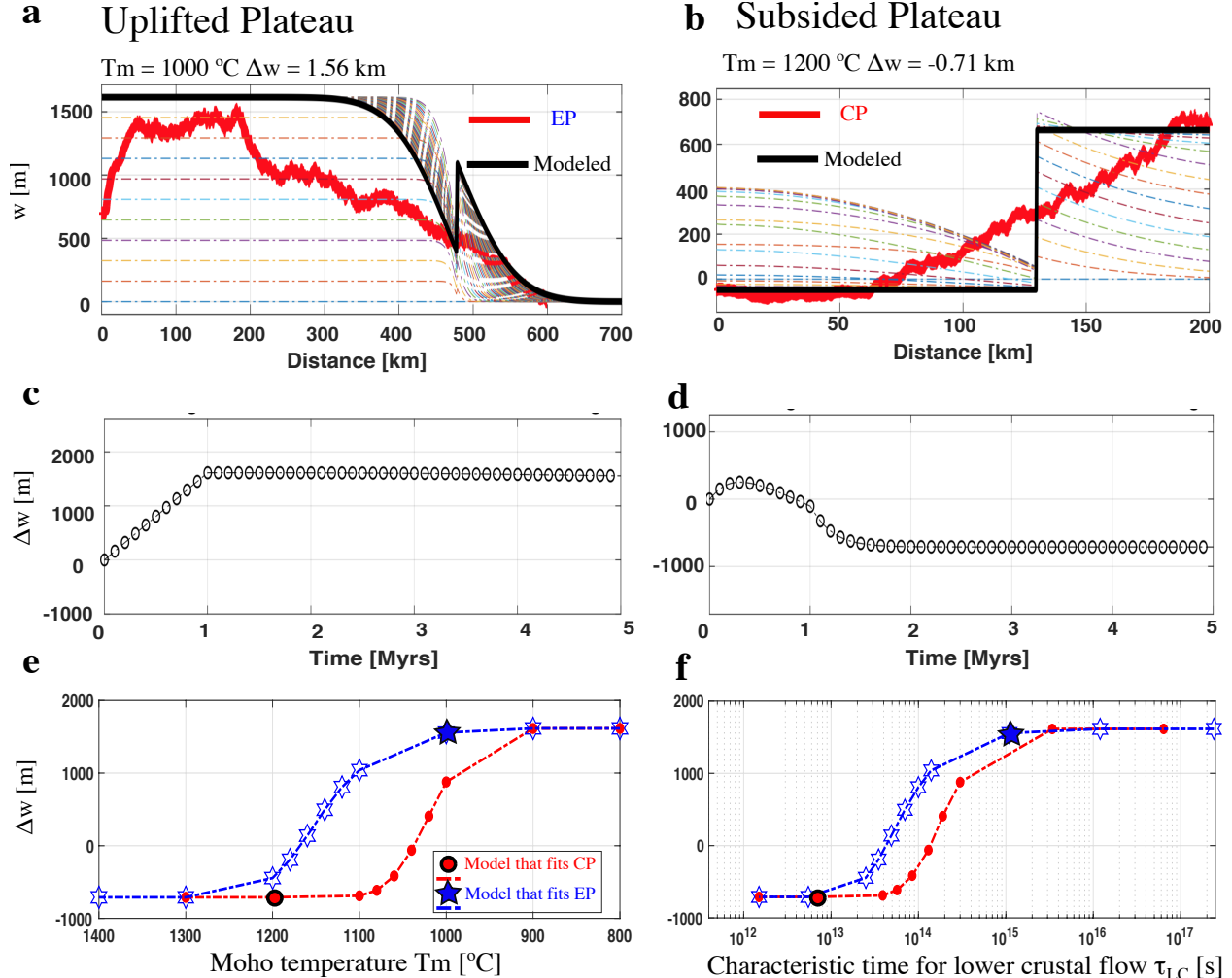


Figure 3. Semi-analytic radially symmetric model results. a-d) Reference models that fit the topography data in Figure 1. a) and b): Bold black lines are the modeled final topography at 5 Myrs to compare with Ethiopian and Columbia Plateaux, respectively, whereas the bold red lines are for 36 stacked data profiles shown in Figure 1. Each thin line is separated in model time of 0.1 Myrs. c) and d): surface elevation offset Δw between center and edge as a function of modeled time. e) and f) summary of model results for Δw at the end of 5 Myrs model time as a function of Moho temperature T_m and characteristic time for lower crustal flow τ_{LC} . The solid blue star is for the model results that match the EP data (b) with a T_m of 1000°C , τ_{LC} of 1.1×10^{15} seconds and a final elevation offset Δw of 1.5 km, the smaller empty blue stars are from other models with different T_m and τ_{LC} . The solid red dots are for the model result in (a) that fits the CP data with a T_m of 1200°C , τ_{LC} of 6.8×10^{12} seconds and a final elevation offset of -0.7 km, the smaller red dots are from other models with different T_m and τ_{LC} . Note that the reference model that fits the CP data has model length $L=200\text{km}$, sill width $W_s = 130 \text{ km}$ and intrusion flux of 3.2cm/yr lasting for 1Myr, while the reference model that fits the EP data has $L=700 \text{ km}$, $W_s = 480 \text{ km}$ with the same intrusion rate and time. Both EP and CP models with $\tau_{LC} \approx 10^{14}$ seconds produce plateaux topographic offset $\Delta w \approx 0 \text{ km}$.

When we show Δw as a function of the characteristic time for lower crustal flow:

$$\tau_{LC} = \frac{W_s H_s}{\kappa_f} = \frac{W_s H_s \eta_0}{\Delta \rho^* g y_0^3} \quad (11)$$

where H_s is the total thickness of the sill intrusions, both series of models show “S”-shaped curves, for which $\tau_{LC} \approx 10^{14}$ seconds corresponds to a plateau of $\Delta w \approx 0$ km for both EP and CP systems (Figure 3f). This indicates that the characteristic time for lower crustal flow τ_{LC} is a robust parameter for predicting topography of models with different controlling parameters. Note that $\tau_{LC} \approx 10^{14}$ seconds is of the same order of magnitude as model end times of 5 Myrs. When τ_{LC} of a model is an order of magnitude larger than the end time of interest, the intrusion induced pressure gradient within the lower crust is not fully relaxed by the lower crustal flow, resulting in an uplifted plateau at the end of modeled time. In contrast, when τ_{LC} of a model is an order of magnitude lower than the end time of interest, the intrusion induced pressure gradient within the lower crust is sufficiently relaxed by the lower crustal flow to produce a low plateau.

From a series of model cases, we find the best fitting results are obtained with $T_m = 1000$ °C, $\tau_{LC} = 1.1 \times 10^{15}$ s and $\Delta w = +1557$ m for the EP system (Figure 3a) and with $T_m = 1200$ °C, $\tau_{LC} = 6.8 \times 10^{12}$ s and $\Delta w = -710$ m for the CP system (Figure 3b). Note that our semi-analytic model doesn’t include flexure and mass wasting, which can significantly smooth the topography to better fit observations. This limitation is addressed in the next section.

2.2.3 Two-dimensional thermo-mechanical model

To reduce the number of assumptions inherent in the semi-analytic model such as local isostasy, the thin channel approximation, a constant thermal structure, and a fixed fraction of intrusions attaching to the upper crust, we developed a fully 2D thermo-mechanical model that can account for sill intrusions and lower crustal flow. The model assumes finite strength of the lithosphere and regional isostasy. The model formulations are a combined result of recent model

developments in simulating SDRs formation (Tian & Buck, 2019) and crustal magma emplacements during LIP formation (Tian & Buck under review; chapter 3 of this thesis).

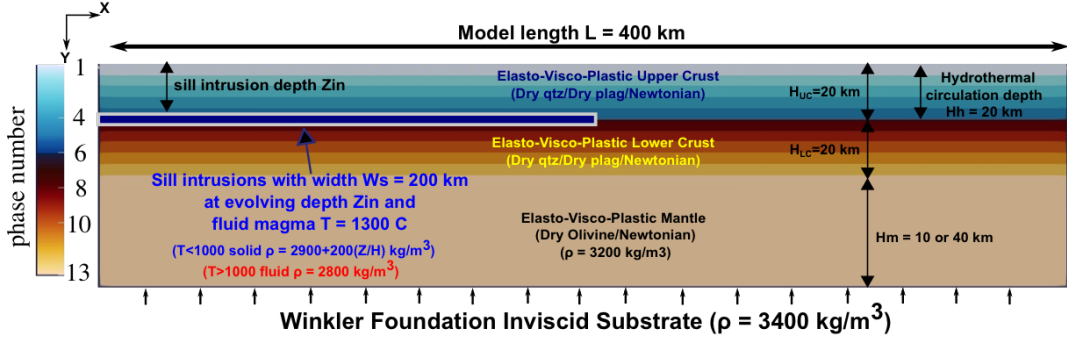
We simulate topographic evolution and deformation of finite thickness lithosphere in response to magmatic emplacement using the numerical code FLAC (Fast Lagrangian Analysis of Continua) (Cundall, 1989). This approach allows us to consider the effects of elastic and nonelastic deformation including viscous flow and brittle-plastic deformation. FLAC is a two-dimensional explicit hybrid finite element-finite difference code that solves continuity, momentum balance, and heat equations. This code has been used to model strain localization for faulting in both two and three dimensions, with and without sedimentation (Choi et al., 2008; Choi & Buck, 2012; Tian & Choi, 2017) and to track heat advection and diffusion (Behn & Ito, 2008; Lavier & Buck, 2002). Higher-resolution tracers are deployed at the surface and move according to the velocity field. These tracers allow more precise quantification of the surface topography.

We simulate the right half of a symmetric LIP (Figure 4a). The top boundary is shear and normal stress free. The bottom boundary is shear stress free and is supported by a Winkler foundation with normal stress equal to the pressure in the underlying inviscid asthenosphere calculated as the lithospheric pressure at the bottom-right corner of the model domain. We assume a density of 3400 kg/m^3 for the inviscid substrate. Both the right and left boundaries are shear stress free with zero horizontal velocities.

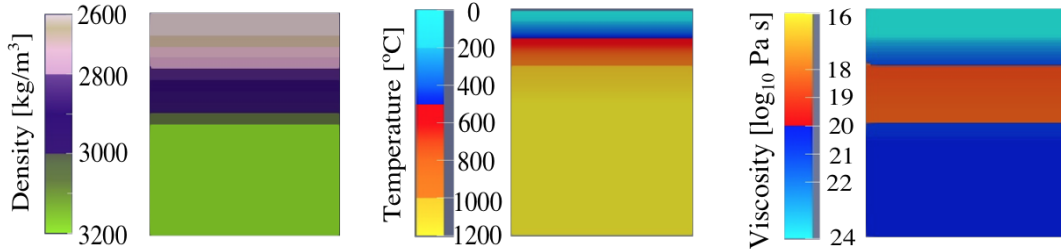
Brittle deformation is calculated with a Mohr-Coulomb failure criterion with a plastic-strain dependent friction angle. As plastic strain increases from 0 to 0.6 the friction angle decreases from 30° to 10° and cohesion decreases from 60 MPa to 20 MPa. Ductile deformation follows either Newtonian or non-Newtonian rheologies. The viscosity η ($\text{Pa} \cdot \text{s}$) is given by $\eta =$

$\dot{\varepsilon}^{\frac{1}{n}-1} A^{-1/n} \cdot \exp [E/nR(T + 273)] \cdot 10^6$ where A ($MPa^{-n} \cdot s^{-1}$) is a pre-factor determined by material property, E (J/mol) is activation energy, $n = 1$ for Newtonian rheology, R is the universal gas constant of 8.314 ($J \cdot mol^{-1} K^{-1}$), and T is the temperature in degrees Celsius.

a. Two-Dimensional Thermo-mechanical Model Setup:



b. Thermo-mechanical Model Initial Conditions:



c. Schematic illustrations for magma overpressure P_d , resistance pressure P_r and magma breakout pressure P_{BK} for determining sill intrusion depth Z_{in} :

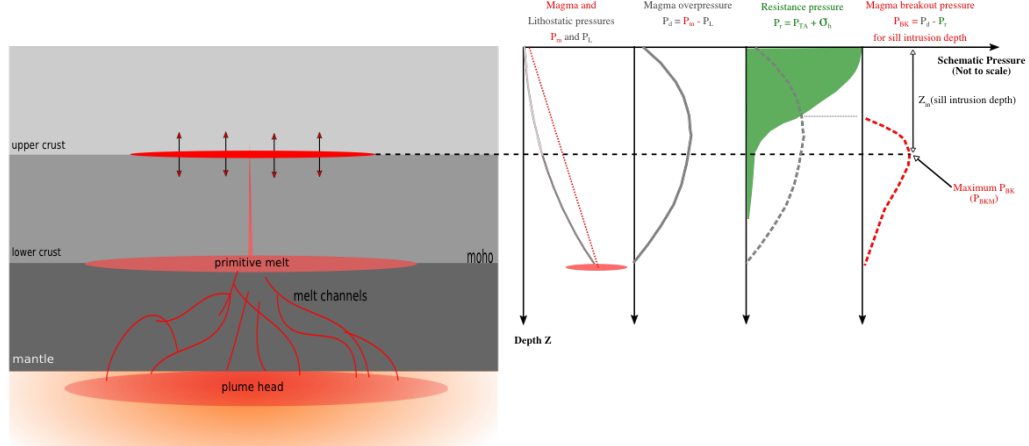


Figure 4. Two-dimensional elasto-visco-plastic thermo-mechanical model setup and schematic illustration for how to determine sill intrusion depth Z_{in} . a) model setup with color scales for phase number, density, temperature and viscosity. Upper crust 20 km thick with linear increasing density of from 2600 kg/m^3 to 2825 kg/m^3 underlying lower crust 20

km thick with a density of 2825 kg/m^3 to 3050 kg/m^3 and either 10 or 40 km thick mantle of density 3200 kg/m^3 and rheology of either Newtonian or non-Newtonian dry quartz or dry plagioclase (for crust) and dry olivine (for mantle) (Goetze & Poirier, 1978) (see supplementary table for parameter values). Model domain is $H = 50 \text{ km}$ or 80 km thick and 400 km wide. Bottom boundary is supported by Winkler foundation with a density of 3400 kg/m^3 . Both the left and right boundaries allow zero horizontal velocity and is free of shear stress. The hot and fluid sill has a density of 2800 kg/m^3 and density increases to $2900 + 200(Z/H) \text{ kg/m}^3$ as it solidified at solidus of 1000°C . b) Initial condition of density, temperature and viscosity. c) Schematic illustration for sill intrusion depth determination.

Magma intrusion is treated as thin but horizontally wide sill intrusions that thicken vertically at a spatially uniform rate. We assume a Gaussian-shaped magma flux in time:

$F_m(t) = F_m^0 \exp(-(t - t_0)^2/2c^2)$, where $F_m^0 = 15 \text{ cm/yr}$ is the maximum sill thickening rate at time $t_0 = 170 \text{ kyrs}$. $c = 210\sqrt{2/\pi} \text{ kyrs}$ and controls the width in time of the Gaussian function. This prescribed flux result in all model cases having the same total sill thickness $H_s = 26.7 \text{ km}$. Intrusion of the sill adds heat from magma at 1300°C with a latent heat of solidification of 400 kJ/kg following Behn & Ito, (2008). Meanwhile, cooling due to hydrothermal circulation is approximated by enhancing the effective thermal conductivity by a factor of Nusselt number in regions shallower than 20 km . After the magmatic flux peaks, Nusselt number is assumed to increase linearly from 20 to 26 with plastic strain increasing from 0 to 1.

The sills have fixed widths $W_s = 200 \text{ km}$ but intrude at evolving depths Z_{in} based on the crustal sill-radius averaged density and thermo-mechanical conditions. For a column of magma rising through crust with density that increases with depth, the magma overpressure (magma pressure minus lithostatic pressure is defined here as driving pressure P_d) will be greatest at the level of neutral buoyancy where density of fluid magma equals to the crustal density. However, if the rocks are cold and strong at this depth the magma should not be able to force a sill to open. We estimate the resistance to sill opening as resistance pressure (P_r). P_r depends partly on the

host rock temperature in that it controls whether magma will freeze before the sill intrusions can open. P_r also depends on the composition and temperature controlling horizontal stress ($\sigma_h(z, t)$) which acts normal to the vertical dike opening wall, because it controls where a vertical sill feeding dike is stopped due to smaller driving pressure relative to that of the horizontal compressive stress. We assume that a sill opens where the breakout pressure ($P_{BK} = P_d - P_r$), namely the difference between the driving pressure P_d and the resistance pressure P_r is as large as the maximum breakout pressure ($P_{BK}(Z_{in}) = P_{BKm}$) (Figure 4c) (see Appendix 3 for details).

As shown in the semi-analytic models, the major change of topography is predicted within a few Myrs of the cessation of intrusion and then is predicted to vary slowly. To save calculation expenses, we only simulate 800 kyr of model time. We vary the initial thermal and rheological conditions to see its effects on magma emplacement processes and topographic development. We assume different combinations of piecewise upper and lower crustal thermal gradients. Upper crustal (< 20 km) thermal gradients are varied with 20, 30, 40, 50 and 60 K/km and lower crustal (20 ~ 40 km) thermal gradients are set at either 15 or 40 K/km. Different combinations of thermal gradients result in different averaged temperatures in the lower crust \bar{T}_{LC} , which we consider as an important parameter for quantifying lower crustal flow. For initial crustal rheological parameters, we test either Newtonian rheologies or non-Newtonian rheologies of dry quartz (Brace & Kohlstedt, 1980) and the stronger dry plagioclase (Shelton & Tullis, 1981).

Two-dimensional numerical model results:

For all model cases the sill intrusion depth follows a similar pattern as illustrated in Figures 5~7. Sills intrude first in the lower crust, then gradually move to shallower depths as the magma flux increases and then downwards as the flux wanes. Changes in sill depth lag the

magma flux changes by ~ 100 kyr due to heat diffusion. Though the same amount of magma is intruded the resulting topography for different cases can be markedly different.

We categorize our model results using the values of final elevation difference Δw between the center of the intrusion and the far side of the model domain (i.e. the difference between the left and right sides of our cartesian models). Three modes of plateau topographic development are defined as: “High plateau” ($\Delta w > 200$ m), “Flat plateau” ($|\Delta w| \leq 200$ m) and “Low plateau” ($\Delta w < -200$ m). Figures 5 through 7 show the topographic development for model cases that illustrate each of the modes. Those figures also show cross-sections of model properties of density, temperature, viscosity and phase at the end of each model run. Supplementary table rows 3,1, and 12 give the input properties of the “High plateau” (Figure 5), “Low plateau” (Figure 6) and “Flat plateau” (Figure 7) models. The other rows describe the remaining 9 model cases considered. Supplementary videos show model cases in cross-sections with vertically exaggerated topography.

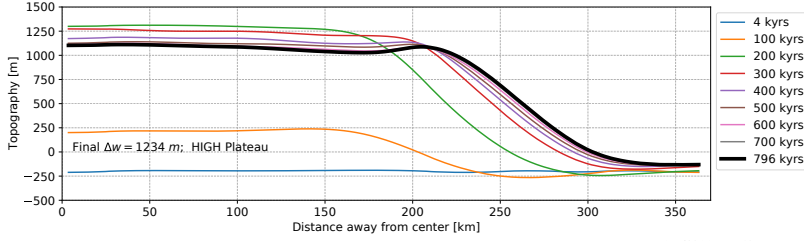
Guided by semi-analytic model results, we again expect the characteristic time for lower crustal flow $\tau_{LC} = \frac{W_s H_s}{\kappa_f}$ (equation 11) to be a major controlling parameter for the 2D model behavior. The effective diffusivity for lower crustal flow is still calculated as $\kappa_f = \frac{\Delta\rho^* g y_0^3}{\eta_0}$ but we consider the average initial crustal density of 2825 kg/m³ as ρ_c and $\rho_m = 3200$ kg/m³ which results in $\Delta\rho^* = 331$ kg/m³. The calculation of y_0 is the same as that of the semi-analytic model. The calculation of η_0 is slightly different in that we use equation $\eta = \dot{\varepsilon}^{\frac{1}{n}-1} A^{-1/n} \cdot \exp[E/nR(T + 273)] \cdot 10^6$ and assume an initial averaged lower crustal strain rate $\dot{\varepsilon} = 10^{-15}$ [s⁻¹] with $T = \bar{T}_{LC}$, the average temperature in the lower crust. Compared to the semi-analytic models, the chosen combinations of thermo-rheological parameters for the 2D numerical

models have a similar span of τ_{LC} that ranges from 10^{12} seconds (32 thousand years) to 10^{18} seconds (32 billion years).

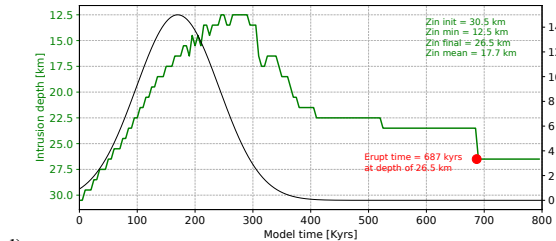
With Newtonian rheology (Figure 8 symbols with a rectangle), when τ_{LC} is larger than the boundary value of $\sim 10^{14}$ s (3.2 million years), “High plateau” mode results. For example, Figure 5 shows a model of “High plateau” mode of final topographic offset $\Delta w = 1234$ m. This model has an initial upper crustal thermal gradient of 30 K/km and lower crustal thermal gradient of 15 K/km, which results in an average lower crustal temperature $\bar{T}_{LC} = 750$ °C and characteristic relaxation time $\tau_{LC} = 4.08 \times 10^{15}$ s. In this model, the sill intrusion is blocked by the strong lithosphere with high viscosity and the lower crust cannot flow sufficiently rapidly. This crustal magma addition causes persistent uplift of the surface by thickening the crust. Note that the sill intrusion depth in this model (Figure 5) is qualitatively similar to that predicted by the 1D model presented in chapter 3 in that the sill intrusion depth first quickly becomes shallower to a minimum depth of 12.5 km as the magma flux increases, and then starts to deepen ~ 130 Kyr after the peak magma flux to a final depth of 26.5 km in the lower crust.

High plateau $\tau_{LC} = 4.08e+15$ [s]

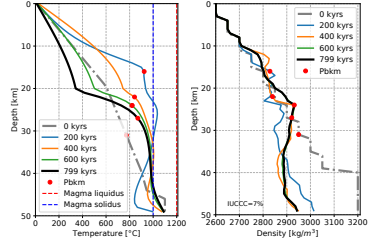
a) Topography



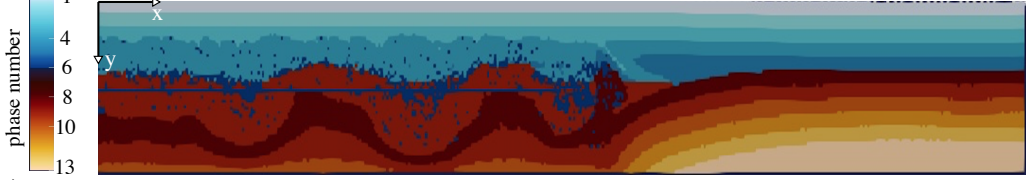
b) Sill intrusion depth and flux



c) Sill radius averaged results



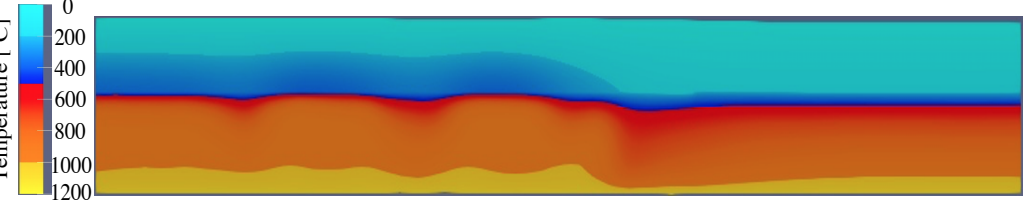
d)



e)



f)



g)

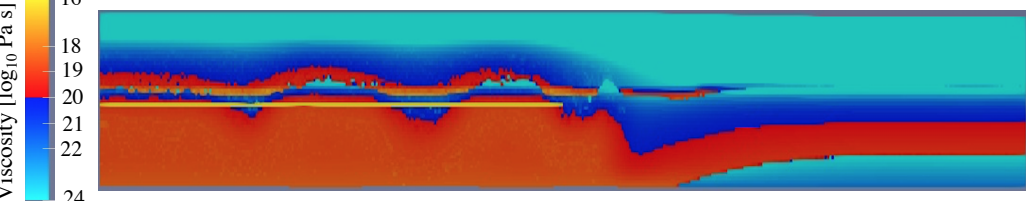


Figure 5. High plateau mode results with $\tau_{LC} = 4.08 \times 10^{15}$ s. a) Plateau topography. b) Sill intrusion depth Zin and flux as a function of model time. c) Sill radius averaged model results for temperature and density. d-g) Model results for phase, density, temperature and viscosity respectively at 796 kyrs of model time.

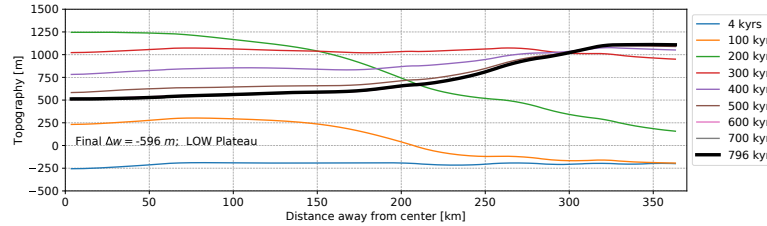
With Newtonian rheology, by increasing upper crustal thermal gradient from 30 K/km to 40 K/km, the average lower crustal temperature \bar{T}_{LC} increases from 750 °C to 950 °C and characteristic time τ_{LC} decreases from 4.08×10^{15} s to 9.75×10^{13} s. Since this is smaller than the boundary value of $\sim 10^{14}$ s a low plateau results. For example, Figure 6 shows a model of the “Low plateau” mode with a final topographic offset $\Delta w = -596$ m. In this model, during the waxing of the magma flux the surface is uplifted to ~ 1 km above the edge in the first 200 Kyr but sill intrusion drives fast lower crustal flow in the mid-to-lower crust. Once the magma flux starts to wane, hydrothermal cooling causes solidification of the intrusion and densification of the mid-to-upper crust. This denser mafic intrusion provides a load that pulls the surface down. The subsidence of the uplifted surface is accommodated by lateral lower crustal flow and the surface becomes almost flat around 300 kyr. As crustal flow continues, a basin 0.6 km deeper than the edge of the model domain is generated at ~ 700 kyr. Note that the sill intrusion depth jumps downward at around 490 Kyr and causes the average overburden density to become larger than fluid magma, causing major phase of flood basalt eruption. In this case, the predicted flood basalt eruptions are accompanied by basin subsidence.

Crustal rheologies play a stronger role in the formation of the “Flat plateau”. For example, with a strong upper crust of dry plagioclase rheology, but weak lower crust of dry quartz rheology, regardless of τ_{LC} (e.g. “Flat mode” Models in rows 7, 8, and 12 have τ_{LC} of 1.15×10^{13} s, 2.58×10^{12} s and 1.87×10^{15} s (Figure 7), most of the sill intrusion remains in the weak lower crust and spreads out quickly to be evenly distributed, so the topographic offset Δw is small. Alternatively, with weak upper crust of dry quartz rheology and strong lower crust of dry plagioclase rheology (model in row 11), few intrusions are retained in the upper crust, and so

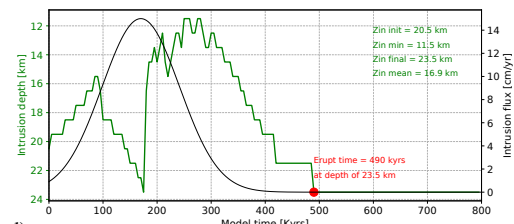
provide minimal loads for surface subsidence. In addition, the lower part of the weak upper crust allows fast lateral spreading of the intrusion and results in an even distribution of materials.

Low plateau $\tau_{LC} = 9.75e+13$ [s]

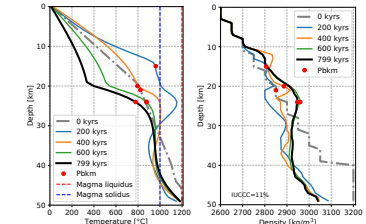
a) Topography



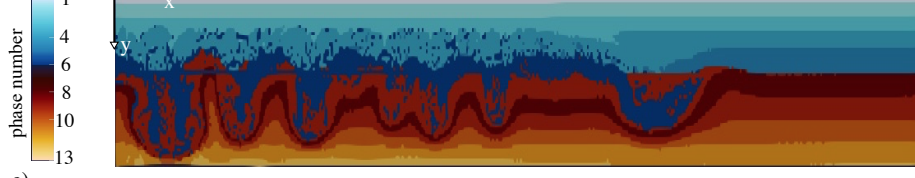
b) Sill intrusion depth and flux



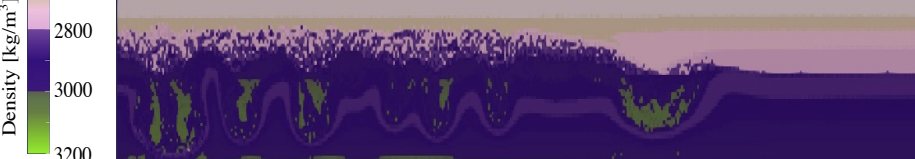
c) Sill radius averaged results



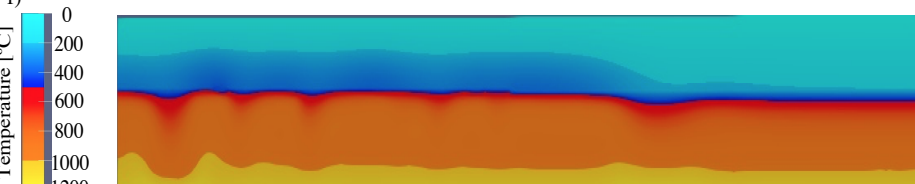
d)



e)



f)



g)

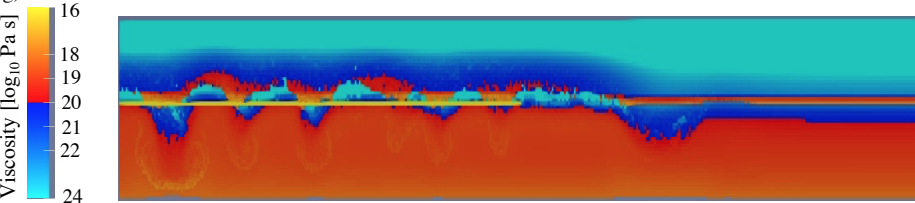
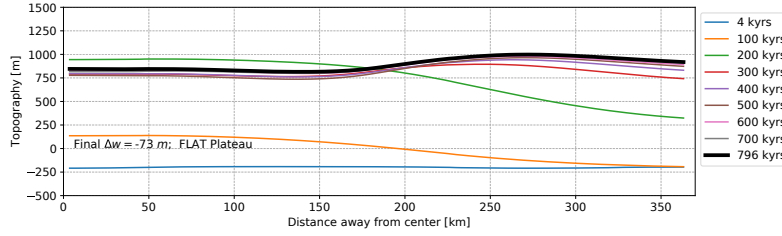


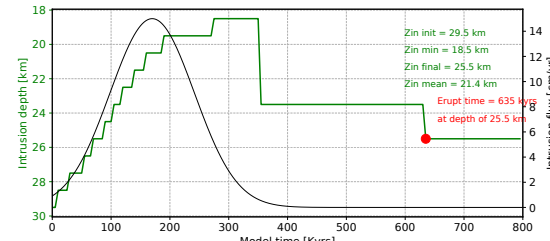
Figure 6. Low plateau mode results with $\tau_{LC} = 9.75 \times 10^{13}$ s. a) Plateau topography. b) Sill intrusion depth Zin and flux as a function of model time. c) Sill radius averaged model results for temperature and density. d-g) Model results for phase, density, temperature and viscosity respectively at 796 kyrs of model time.

Flat plateau $\tau_{LC} = 1.87e+15$ [s]

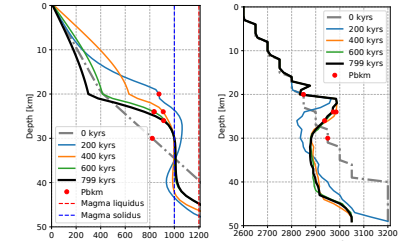
a) Topography



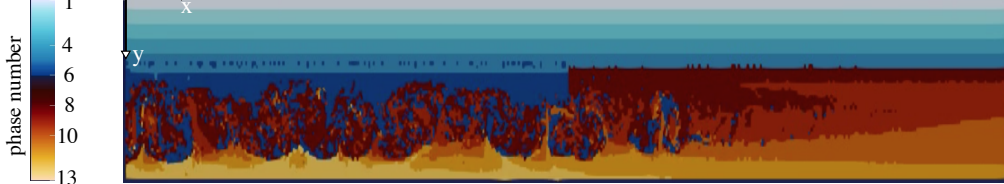
b) Sill intrusion depth and flux



c) Sill radius averaged results



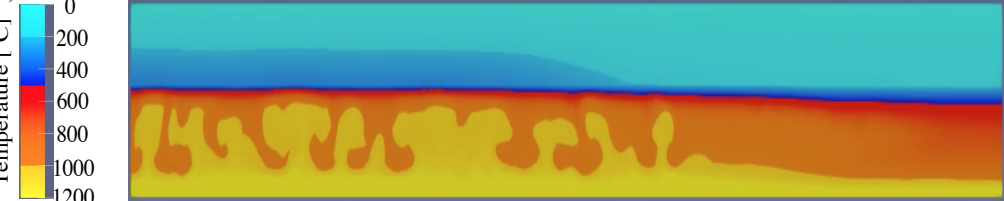
d)



e)



f)



g)

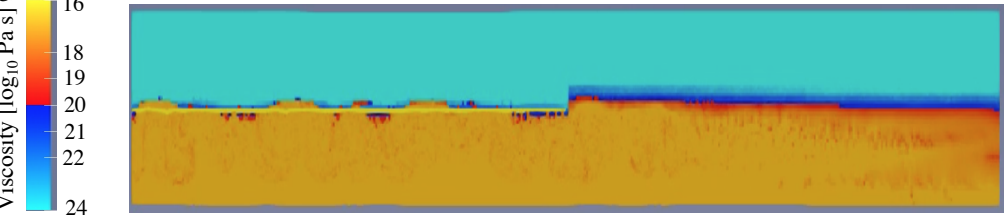


Figure 7. Flat plateau mode results with $\tau_{LC} = 1.87 \times 10^{15}$ s. a) Plateau topography. b) Sill intrusion depth Zin and flux as a function of model time. c) Sill radius averaged model results for temperature and density. d-g) Model results for phase, density, temperature and viscosity respectively at 796 kyr of model time.

2.3 Discussion and Conclusions

Figure 8 summarizes all the 2D thermo-mechanical model results according to the topographic offset Δw at the end of model calculations as a function of the characteristic time for lower crustal flow τ_{LC} . The overall behavior of the 2D models is similar to the simple results of semi-analytic models that show an “S-shaped” trend in that a high plateau results when τ_{LC} is large while a low plateau usually results for small values of τ_{LC} (Figure 3h and Figure 8). The characteristic time for lower crustal flow τ_{LC} is the single most important parameter for predicting model behavior by quantifying how important lower crustal flow can be, for accommodating the crustal magma emplacement and controlling surface subsidence. A boundary value of $\tau_{LC} \approx 10^{14} s$ (3.2 million years) separates all “low plateau” versus “high plateau” models, similar to the results of the semi-analytic models. When τ_{LC} is larger than the boundary value, within the time scale of interest, lower crustal flow is too slow to fully accommodate the crustal addition and a persistent “high plateau” results. In contrast, when τ_{LC} is smaller than the boundary value, any input that could cause surface uplift, due to either a thermal anomaly in the mantle or to crustal magma emplacement, will be relaxed by lower crustal flow and results in formation of a flat or low plateau.

The key for the model to generate a low plateau rather than a flat plateau lies in how much magma intrusion can attach to and remain in the upper crust, and so pull the surface down. The more realistic 2D model results show several complications in the formation of low vs. flat plateau modes. First, the initial crustal thermal condition is important. If the crust is hot, the average sill intrusion depth is shallower and more magma is emplaced into the upper crust. However, this hotter thermal condition also causes a mechanically weaker crust. This makes sill intrusion attachment to the crust less probable. Instead intruded materials are more prone to

undergo density-driven foundering via a Rayleigh-Taylor instability. In contrast, if the crust is initially cold and mechanically strong, this allows better coupling between the sill intrusion and the upper crust. In this case, the average sill intrusion depth is deeper, with less upper crustal intrusion. Sill intrusion is more likely to focus in the lower crust, which flows laterally, resulting in a flat plateau without loading the upper crust. Secondly, the 2D results indicate that the amount of dense sill material attaching to the upper crust controls whether a flat or a low plateau develops. We quantify the attachment by calculating the intrusion coupling coefficient (ICC) where $ICC = (\overline{\rho_{uc2}} - \overline{\rho_{uc1}})/(\overline{\rho_{ucfc}} - \overline{\rho_{uc1}})$, where $\overline{\rho_{uc1}}$, $\overline{\rho_{uc2}}$ and $\overline{\rho_{ucfc}}$ are average density of the initial upper crust, average density of the upper crust at the end of model run, and average density of the upper crust if half of the sill intrusion material are able to attach to the bottom of the upper crust. For the cases considered here the maximum value of the ICC is ~ 0.2 . In other words, at most 20% of the upper crust is replaced by sill materials. Our model results show that, when in low plateau mode, the higher the ICC, the larger the absolute value of the negative topographic offset Δw (when comparing models in rows 5 and 6 or 9 and 11 where only upper crustal rheology parameters are changed). The control of ICC is complicated and warrants further investigation. Several factors are important, including the evolving sill depth which depends on the strength of the upper and lower crust, the density of intruded liquid magma, and the density of solidified basalt. For example, if the average sill intrusion depth is larger than 20 km in the lower crust, a very low value of ICC results (e.g. models in rows 10 and 12 have ICC of 2% and 4%, and average sill intrusion depths of 25.2 km and 21.4 km). Higher ICC correlates in general with higher averaged crustal temperature as more magma is able to intrude the upper crust and retain at shallower depths.

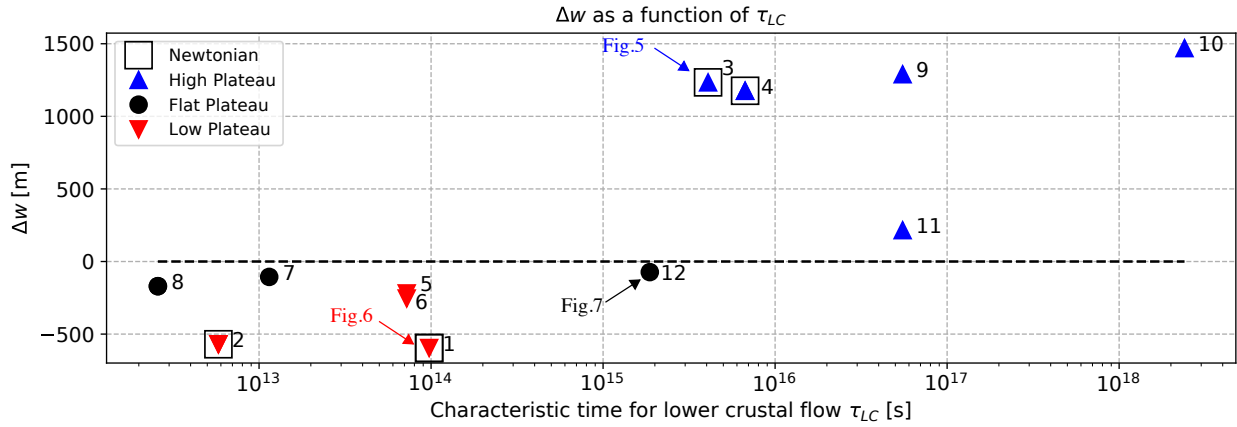


Figure 8. Summary of thermo-mechanical model results for modes of volcanic plateau topographic development as a function of the characteristic time for lower crustal flow τ_{LC} . $\tau_{LC} \approx 10^{14}$ s corresponds to the regime boundary between low and high plateaux, as constrained by the semi-analytic models. The reference models of ‘High’, ‘Low’ and ‘Flat’ modes are annotated with ‘Fig.5’, ‘Fig. 6’ and ‘Fig. 7’. Models with Newtonian rheologies are annotated with an empty rectangle. Row numbers in the table are annotated to the right of each symbol.

In light of detailed stratigraphy of the Columbia flood basalts, Reidel et al., 2013 concluded that the flood basalts were emplaced during basin subsidence. Perry-Houts & Humphreys, (2018) propose that the low topography of the plateau results from a phase change in the lower crust. They argue that lava flows load the crust and increase pressure, which in turn drives gabbroic lower crust to change to dense eclogite . The dense eclogite then drives subsidence of the plateau. However, it is hard to see why this process would not drive subsidence of other LIP-related volcanic plateaus like the Ethiopian plateau. Also, the high heat flow of the Basin and Range region adjacent to the Columbia Plateau may indicate that the lower crust there may be too weak to transmit vertical stresses. In that case, the dense eclogite at the base of the crust would not load the surface and cause subsidence. Instead, our model shows that intrusion of mafic material into less dense upper crust can drive subsidence.

Our relatively simple model is consistent with several other observations. First, it explains why geophysical and geochemical data for a number of LIP provinces indicate that 3-16

times as much mafic magma is apparently intruded than is extruded (Coffin and Eldholm, 1994; Crisp, 1984; Ridley and Richards, 2010). As discussed further in Chapter 3, our model considers that magma cannot be erupted unless the density of the material overlying a magmatic sill is denser than the fluid magma. The lower density of felsic continental crust relative to mafic magma then may mean that only when enough magma is intruded to heat and densify the crust via the accumulation of large, shallow intrusions can flood basalts erupt. In contrast andesitic magmas are lower in density than typical continental upper crust and so can extrude without significant accumulation of dense intrusions in the upper crust.

Second, for the Columbia Plateau Basalts, the model explains why the bulk of the erupted lavas filled a subsiding basin. As noted in the previous paragraph, in order to lead to surface extrusion, the model requires that a modest fraction of the intrusives attach to and replace part of the strong upper crust. If the lower crust is hot and weak enough to flow laterally on the time scale of intrusion, then the surface will subside before extrusion can begin.

Finally, the present model may explain a recently identified time lag between global warming events and extrusion of LIP magmas. A correlation between LIP events, climatic excursions, and major extinction events has long been noted. Recent high-resolution dating of the age of LIP extrusives indicates that, for at least two LIP-climatic events, global warming began several hundred thousand years before the onset of the bulk of volcanism. For one of the largest LIPs, the Deccan traps, new data suggests that 75% of the flood basalts were emplaced after the Cretaceous-Paleogene (K/Pg) boundary (Sprain et al., 2019). Global temperature proxy data suggests an average 2 °C global warming began ~360 Kyrs before the K/Pg boundary (Hull et al., 2020). CO₂ release from the youngest LIP, the Columbia River Basalts (CRB), is the most obvious trigger for the rapid global warming and ice sheet melting during the mid-Miocene

climate optimum (MCO; 17-14.7 Ma) (Holbourn et al., 2015). However, recent basalt chronology data indicates that 95% of the CRB was erupted after 16.7 Ma, ~300 kyrs after the onset of MCO (Kasbohm & Schoene, 2018). Thus, the new data for both the Deccan Traps and the CRB are inconsistent with the hypothetical causal link between LIP volcanism and global warming. Our models show that major eruptions of continental flood basalts may require densification of the crust by earlier intrusion of larger volumes of magma, compared to smaller volumes of lava during later eruption. Simple models in Chapter 3 show that magma crystallization and release of CO₂ from such intrusions could produce global warming hundreds of thousands of years before the main phase of flood basalt eruptions. Consistent with many geological, geophysical, geochemical and paleoclimate data, our models suggest that the evolving crustal density has a first order control on timing of the major phase of continental flood basalt volcanism while underground degassing of CO₂ during crystallization of earlier, larger volume of mafic intrusions plays a significant role in controlling the Earth's climate and habitability.

Several things can be done in the future to improve models of intrusion and extrusion for LIPs and other volcanic systems. For example, in the next stage of plateau models, the load of surface flows would be included just as in Chapter 1 where lava flow thickness and density are included to simulate the shape formations of seaward dipping reflectors. Magma emplacement could also be treated in a more self-consistent way: both the location and geometry of magma emplacement could be physically simulated based on the interactions between crustal thermo-mechanical conditions and the magma supply rate, rather than being specified.

References:

- Behn, M. D., & Ito, G. (2008). Magmatic and tectonic extension at mid-ocean ridges: 1. Controls on fault characteristics. *Geochemistry, Geophysics, Geosystems*, 9(8), n/a-n/a. <https://doi.org/10.1029/2008GC001965>
- Bird, P. (1991). Lateral extrusion of lower crust from under high topography in the isostatic limit. *Journal of Geophysical Research: Solid Earth*, 96(B6), 10275. <https://doi.org/10.1029/91JB00370>
- Brace, W. F., & Kohlstedt, D. L. (1980). Limits on lithospheric stress imposed by laboratory experiments. *Journal of Geophysical Research: Solid Earth*, 85(B11), 6248–6252. <https://doi.org/10.1029/JB085iB11p06248>
- Bryan, S. E., & Ernst, R. E. (2008). Revised definition of Large Igneous Provinces (LIPs). *Earth-Science Reviews*, 86(1–4), 175–202. <https://doi.org/10.1016/j.earscirev.2007.08.008>
- Bryan, S. E., & Ferrari, L. (2013). Large igneous provinces and silicic large igneous provinces: Progress in our understanding over the last 25 years. *Geological Society of America Bulletin*, 125(7–8), 1053–1078. <https://doi.org/10.1130/B30820.1>
- Buck, W. R. (2006). The role of magma in the development of the Afro-Arabian Rift System. *Geological Society, London, Special Publications*, 259(1), 43–54. <https://doi.org/10.1144/GSL.SP.2006.259.01.05>
- Buck, W. Roger. (1991). Modes of continental lithospheric extension. *Journal of Geophysical Research: Solid Earth*, 96(B12), 20161–20178. <https://doi.org/10.1029/91JB01485>
- Buck, W. Roger, Lavier, L. L., & Poliakov, A. N. B. (2005). Modes of faulting at mid-ocean ridges. *Nature*, 434(7034), 719–723. <https://doi.org/10.1038/nature03358>
- Choi, Eun-seo, Lavier, L., & Gurnis, M. (2008). Thermomechanics of mid-ocean ridge segmentation. *Physics of the Earth and Planetary Interiors*, 171(1–4), 374–386. <https://doi.org/10.1016/j.pepi.2008.08.010>
- Choi, Eunseo, & Buck, W. R. (2012). Constraints on the strength of faults from the geometry of rider blocks in continental and oceanic core complexes. *Journal of Geophysical Research: Solid Earth*, 117(4), 1–14. <https://doi.org/10.1029/2011JB008741>
- Clark, M. K., & Royden, L. H. (2000). Topographic ooze: Building the eastern margin of Tibet by lower crustal flow. *Geology*, 28(8), 703. [https://doi.org/10.1130/0091-7613\(2000\)28<703:TOBTEM>2.0.CO;2](https://doi.org/10.1130/0091-7613(2000)28<703:TOBTEM>2.0.CO;2)
- Coffin, M. F., & Eldholm, O. (1994). Large igneous provinces: Crustal structure, dimensions, and external consequences. *Reviews of Geophysics*, 32(1), 1. <https://doi.org/10.1029/93RG02508>

- Courtillot, V., Jaupart, C., Manighetti, I., Tappognier, P., & Besse, J. (1999). On causal links between flood basalts and continental breakup. *Earth and Planetary Science Letters*, 166(3–4), 177–195. [https://doi.org/10.1016/S0012-821X\(98\)00282-9](https://doi.org/10.1016/S0012-821X(98)00282-9)
- Courtillot, V. E., & Renne, P. R. (2003). On the ages of flood basalt events. *Comptes Rendus Geoscience*, 335(1), 113–140. [https://doi.org/10.1016/S1631-0713\(03\)00006-3](https://doi.org/10.1016/S1631-0713(03)00006-3)
- Crisp, J. A. (1984). Rates of magma emplacement and volcanic output. *Journal of Volcanology and Geothermal Research*, 20(3–4), 177–211. [https://doi.org/10.1016/0377-0273\(84\)90039-8](https://doi.org/10.1016/0377-0273(84)90039-8)
- Cundall, P. A. (1989). Numerical experiments on localization in frictional materials. *Ingenieur-Archiv*, 59(2), 148–159. <https://doi.org/10.1007/BF00538368>
- Davis, J. K., & Lavier, L. L. (2017). Influences on the development of volcanic and magma-poor morphologies during passive continental rifting. *Geosphere*, 13(5), 1524–1540. <https://doi.org/10.1130/GES01538.1>
- Ebinger, C. J., Bechtel, T. D., Forsyth, D. W., & Bowin, C. O. (1989). Effective elastic plate thickness beneath the East African and Afar plateaus and dynamic compensation of the uplifts. *Journal of Geophysical Research*, 94(B3), 2883–2901. <https://doi.org/10.1029/JB094iB03p02883>
- Goetze, C., & Poirier, J. P. (1978). The Mechanisms of Creep in Olivine [and Discussion]. *Philosophical Transactions of the Royal Society A: Mathematical, Physical and Engineering Sciences*, 288(1350), 99–119. <https://doi.org/10.1098/rsta.1978.0008>
- Hofmann, C., Courtillot, V., Féraud, G., Rochette, P., Yirgu, G., Ketefo, E., & Pik, R. (1997). Timing of the Ethiopian flood basalt event and implications for plume birth and global change. *Nature*, 389(6653), 838–841. <https://doi.org/10.1038/39853>
- Holbourn, A., Kuhnt, W., Kochhann, K. G. D., Andersen, N., & Sebastian Meier, K. J. (2015). Global perturbation of the carbon cycle at the onset of the Miocene Climatic Optimum. *Geology*, 43(2), 123–126. <https://doi.org/10.1130/G36317.1>
- Hull, P. M., Bornemann, A., Penman, D. E., Henehan, M. J., Norris, R. D., Wilson, P. A., et al. (2020). On impact and volcanism across the Cretaceous-Paleogene boundary. *Science*, 367(6475), 266–272. <https://doi.org/10.1126/science.aay5055>
- Husson, L., & Sempere, T. (2003). Thickening the Altiplano crust by gravity-driven crustal channel flow. *Geophysical Research Letters*, 30(5), 1–4. <https://doi.org/10.1029/2002gl016877>
- Jones, M. T., Jerram, D. A., Svensen, H. H., & Grove, C. (2016). The effects of large igneous provinces on the global carbon and sulphur cycles. *Palaeogeography, Palaeoclimatology, Palaeoecology*, 441, 4–21. <https://doi.org/10.1016/j.palaeo.2015.06.042>

- Kasbohm, J., & Schoene, B. (2018). Rapid eruption of the Columbia River flood basalt and correlation with the mid-Miocene climate optimum. *Science Advances*, 4(9), eaat8223. <https://doi.org/10.1126/sciadv.aat8223>
- Kronenberg, A. K., & Tullis, J. (1984). Flow strengths of quartz aggregates: Grain size and pressure effects due to hydrolytic weakening. *Journal of Geophysical Research: Solid Earth*, 89(B6), 4281–4297. <https://doi.org/10.1029/JB089iB06p04281>
- Lavier, L. L., & Buck, W. R. (2002). Half graben versus large-offset low-angle normal fault: Importance of keeping cool during normal faulting, 107, 1–16.
- Leveque, R. J. (2007). *Finite Difference Methods for Ordinary and Partial Differential Equations - Steady-State and Time-Dependent Problems*. SIAM.
- McQuarrie, N., & Rodgers, D. W. (1998). Subsidence of a volcanic basin by flexure and lower crustal flow: The eastern Snake River Plain, Idaho. *Tectonics*, 17(2), 203–220. <https://doi.org/10.1029/97TC03762>
- Reidel, S. P., Camp, V. E., Tolan, T. L., Kauffman, J. D., & Garwood, D. L. (2013a). Tectonic evolution of the Columbia River flood basalt province. In *The Columbia River Flood Basalt Province* (Vol. 46, pp. 651–654). Geological Society of America. [https://doi.org/10.1130/2013.2497\(12\)](https://doi.org/10.1130/2013.2497(12))
- Reidel, S. P., Camp, V. E., Tolan, T. L., Kauffman, J. D., & Garwood, D. L. (2013b). Tectonic evolution of the Columbia River flood basalt province. *The Columbia River Flood Basalt Province*, 497(12), 293–324. [https://doi.org/10.1130/2013.2497\(12\)](https://doi.org/10.1130/2013.2497(12))
- Ridley, V. A., & Richards, M. A. (2010). Deep crustal structure beneath large igneous provinces and the petrologic evolution of flood basalts. *Geochemistry, Geophysics, Geosystems*, 11(9), Q09006. <https://doi.org/10.1029/2009GC002935>
- Rooney, T. O., Krans, S. R., Mège, D., Arnaud, N., Korme, T., Kappelman, J., & Yirgu, G. (2018). Constraining the Magmatic Plumbing System in a Zoned Continental Flood Basalt Province. *Geochemistry, Geophysics, Geosystems*, 19(10), 3917–3944. <https://doi.org/10.1029/2018GC007724>
- Shelton, G. L., & Tullis, J. (1981). Experimental flow laws for crustal rocks. In *EOS Trans. Am. Geophys. Union* (Vol. 62, p. 396). Retrieved from <http://ci.nii.ac.jp/naid/10010125720/en/>
- Sobolev, S. V., Sobolev, A. V., Kuzmin, D. V., Krivolutskaya, N. A., Petrunin, A. G., Arndt, N. T., et al. (2011). Linking mantle plumes, large igneous provinces and environmental catastrophes. *Nature*, 477(7364), 312–316. <https://doi.org/10.1038/nature10385>

Sprain, C. J., Renne, P. R., Vanderkluysen, L., Pande, K., Self, S., & Mittal, T. (2019). The eruptive tempo of Deccan volcanism in relation to the Cretaceous-Paleogene boundary. *Science*, 363(6429), 866–870. <https://doi.org/10.1126/science.aav1446>

Tian, X., & Buck, W. R. (2019). Lithospheric Thickness of Volcanic Rifting Margins: Constraints From Seaward Dipping Reflectors. *Journal of Geophysical Research: Solid Earth*, 124(4), 3254–3270. <https://doi.org/10.1029/2018JB016733>

Tian, X., & Choi, E. (2017). Effects of axially variable diking rates on faulting at slow spreading mid-ocean ridges. *Earth and Planetary Science Letters*, 458, 14–21. <https://doi.org/10.1016/j.epsl.2016.10.033>

Turcotte, D. L., & Schubert, G. (2002). *Geodynamics*. Cambridge: Cambridge University Press. <https://doi.org/10.1017/CBO9780511807442>

Wignall, P. B. (2001). Large igneous provinces and mass extinctions. *Earth-Science Reviews*, 53(1–2), 1–33. [https://doi.org/10.1016/S0012-8252\(00\)00037-4](https://doi.org/10.1016/S0012-8252(00)00037-4)

Chapter 3: Intrusion Induced Global Warming Preceding

Continental Flood Basalt Volcanism*

Temporal correlations between continental flood basalt eruptions and mass extinctions are well known¹. Massive carbon degassing from volcanism of Large Igneous Provinces can cause catastrophic global climatic and biotic perturbations^{1–3}. However, recent more accurate dating of the Deccan Traps⁴ and Columbia River Basalts⁵ challenges this causal link by showing that global warming preceded the major phase of flood basalts eruptions by several hundred thousand years. Here, we argue that major eruptions of continental flood basalts may require densification of the crust by intrusion of larger volumes of magma than are extruded. Simple models show that magma crystallization and release of CO₂ from such intrusions could produce global warming before the main phase of flood basalt eruptions on the observed timescale. Being consistent with many geological, geophysical, geochemical and paleoclimate data, our model suggests that the evolving crustal density has a first order control on timing of the major phase of continental flood basalt volcanism while the preceding intrusion induced underground degassing of CO₂ plays a significant role in controlling the Earth's climate and habitability.

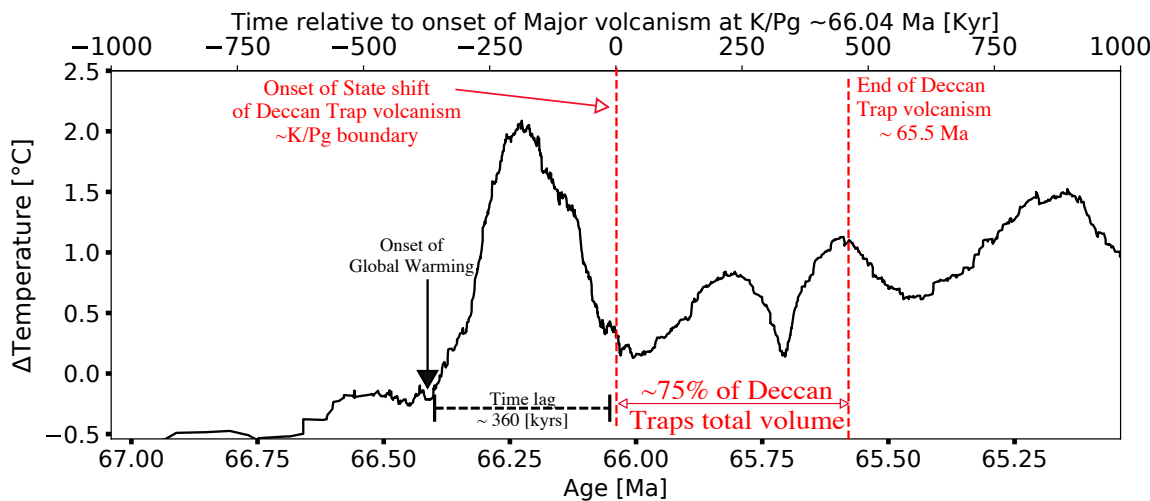
* This chapter is under review at the journal Nature Geoscience.

3.1 Main Text

By far the largest volcanic eruptions occur during the formation of continental flood basalts that define the surface extent of Large Igneous Provinces (LIPs). Major LIPs typically extrude more than 10^6 km³ of magma within 1 million years ². Estimates of carbon dioxide (CO₂) concentrations in primitive LIP magma vary from 0.1 to ~2 weight percent ⁶, so that an LIP could release as much as 6×10^{16} Kg of CO₂. Such fluxes are enough to significantly warm the Earth's climate ⁷. The emplacement of LIPs are widely recognized to be coeval with climate changes and mass extinctions events ¹. These temporal correlations support the idea that flood basalt eruptions releasing massive amounts of greenhouse gases may cause climatic excursions and biotic crises.

Recent data indicate that for at least two LIP-climatic events global warming began several hundred thousand years before the onset of the bulk of volcanism. For one of the largest LIPs, the Deccan traps, new data suggests that 75% of the flood basalts were emplaced after the Cretaceous-Paleogene (K/Pg) boundary ⁴. Global temperature proxy data suggests an average 2 °C global warming began ~360 Kyr before the K/Pg boundary ⁷ (Fig. 1a). CO₂ release from the youngest LIP, the Columbia River Basalts (CRB), is the most obvious trigger for the rapid global warming and ice sheet melting during the Miocene climate optimum (MCO; 17-14.7 Ma) ⁸. However, recent basalt chronology data indicates that 95% of the CRB was erupted after 16.7 Ma, ~300 kyr after the onset of MCO ⁵ (Fig. 1b). The new data for both the Deccan Traps and the CRB is inconsistent with the hypothetical causal link between LIP volcanism and global warming.

a



b

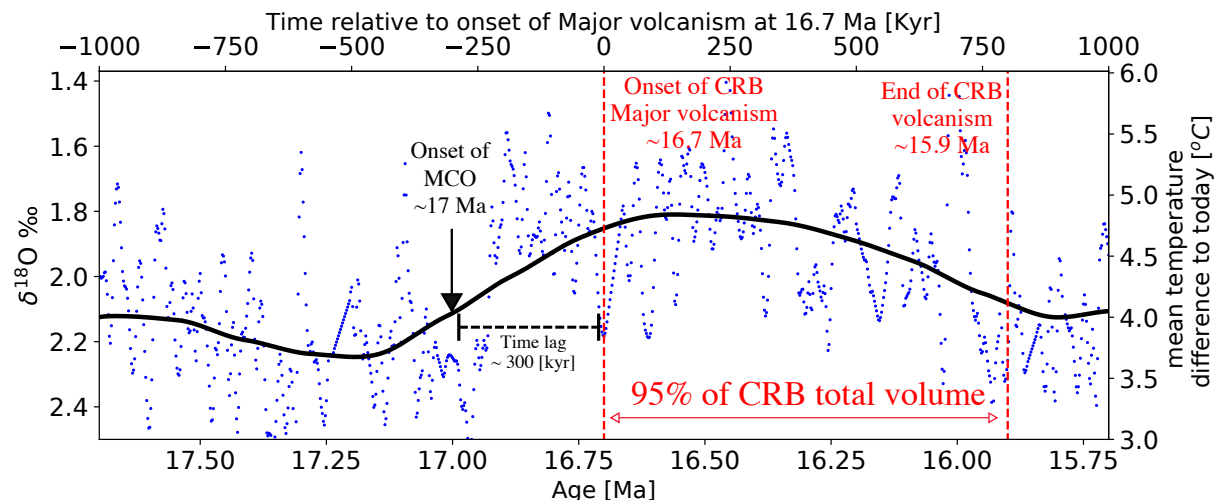


Fig. 1 | Decoupled global temperature change and major phase of flood basalt eruptions. a, across the Cretaceous-Paleogene (K/Pg) boundary at ~66.04 Ma, the onset of global warming predates the major phase of Deccan Trap volcanism (75% of total volume) by ~360 kyrs. b, Onset of Miocene Climate Optimum (MCO) predates the major phase of Columbia River Basalts (95% of total volume) by ~300 kyrs. Global temperature change across K/Pg is from Ref ⁷ and temperature proxy benthic $\delta^{18}\text{O}$ during Miocene Climate Optimum is from Ref ⁹.

Volcanoes are pathways for magma to reach the Earth's surface, but for many volcanoes more magma is intruded than is erupted ^{10–12}. For continental LIPs, geophysical data indicates that from 3 to 16 times more magma is intruded as is extruded ^{2,13,14}. For example, below the Deccan Traps and the CRB higher-than-normal seismic velocities indicate voluminous mafic

crustal intrusions^{15–17}. Geochemical studies of the CRB also indicate up to 85% of total magma volume are emplaced within the crust¹⁸.

Crystallization releases nearly all carbon dioxide dissolved in basaltic magma^{19,20}. Gas released from solidifying intruded magma should traverse the overlying crust through fractures, faults and hydrothermal vents²¹, as is seen at Yellowstone²² or the East African Rift²³. Thus, the intrusion and solidification of millions of cubic kilometers of basaltic LIP magma would release far more CO₂ than released by extrusion. If the intrusion precedes extrusion it would explain the recent results showing global warming preceding LIP surface flows.

Geochemical studies indicate that mantle-derived magma resides for thousands of years in crustal magma chambers or sills at various depths before it extrudes²⁴. For extrusion, the pressure in such magma reservoirs must be greater than the hydrostatic pressure at the base of a column of magma from the surface to the reservoirs. The long-term average pressure in a magma reservoir should equal the lithostatic pressure (the average density of the overlying crust times the acceleration of gravity and the depth below the surface). Magma reservoirs can be ‘overpressured’ relative to lithostatic pressure, but it is difficult to maintain overpressure if magma reservoirs are large and/or are surrounded by low viscosity crust^{25,26}. For many LIPs crustal intrusions are thought to be very large, with lateral dimensions up to ~10³ kilometers^{14,17,27} so that overpressures should be negligible. Thus, large flood basalt extrusions may only happen when the average overburden density is greater than the magma density.

Particularly clear evidence for the importance of crustal density in controlling eruptions comes from plate spreading centers. Constraints on the depth of axial magma chambers (AMCs) and the crustal density structure at oceanic spreading centers are superior to those for continental magma bodies due to the greater resolving power of marine seismic methods. AMCs are fairly

small (~1 km wide) and are seen to lie at or below the depth where the average overburden density equals magma density, a depth that is termed the ‘level of eruptibility’^{28,29}.

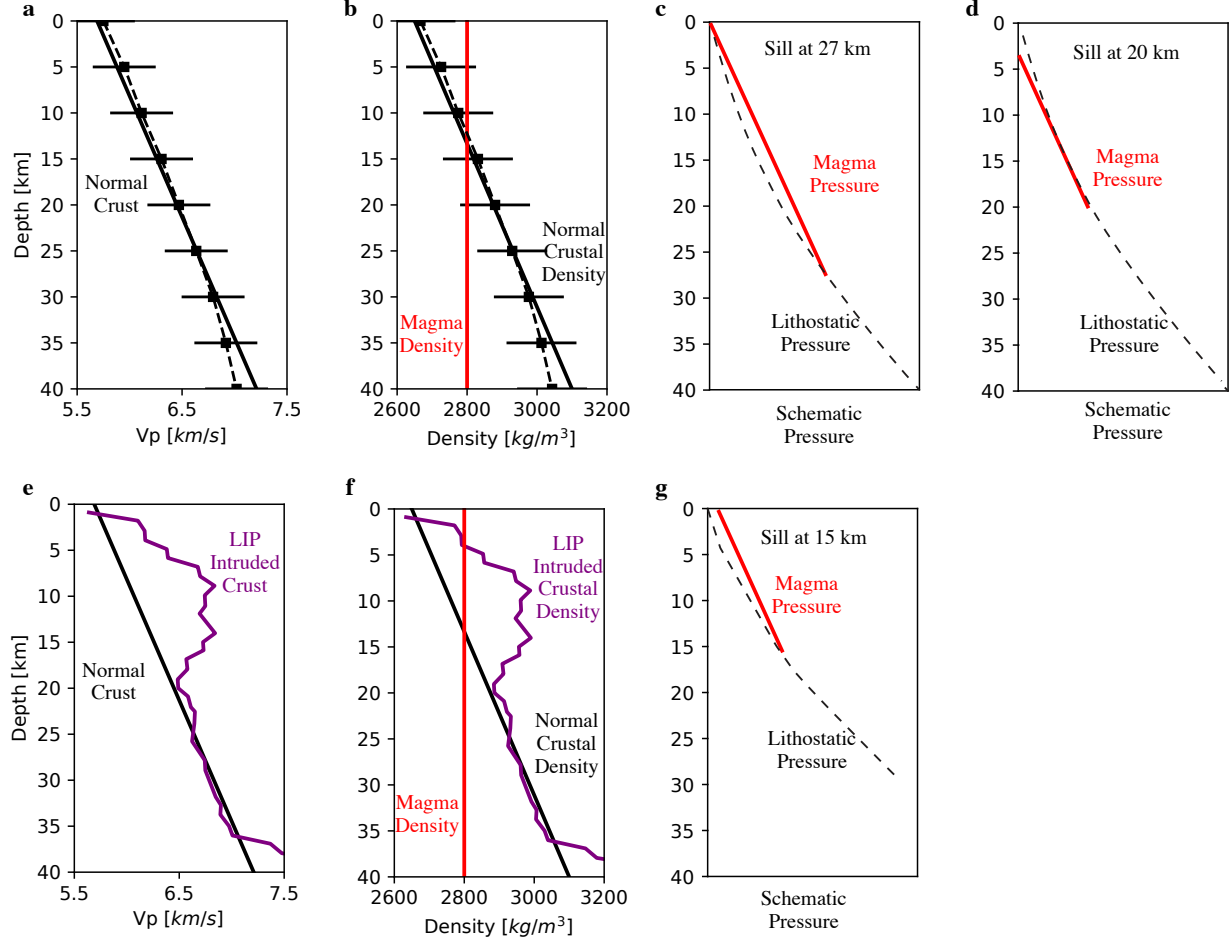


Fig. 2 | Illustrations of relations between seismic velocities, densities and pressures in typical continental crust (a-d) and the crust under the Deccan LIP (e-g). a, shows average continental P-wave velocity (dashed) from ref. ³⁰ with linear fit (solid) and b, density estimated assuming a linear relation between velocity and density. Magma density is from ref. ³¹. P-wave velocity e and density f profiles beneath Deccan Traps are converted from refs. ^{15,16} using a Vs to Vp relationship (ref. ³²). Schematic pressure is shown without a scale to allow the difference between lithostatic (dashed) and ‘magmastic’ to be visible.

Continental crustal density generally increases with depth and so the average density of overburden also increases with depth. Figure 2a shows the average seismic compressional wave velocities in continental crust with depth based on global seismic experiments ³⁰. Their comprehensive analysis yields a linear regression fit between seismic velocity and density for

crustal rocks at different depths and Fig. 2b shows the density structure based on the seismic velocities assuming such a linear relationship. Upper continental crust is composed of ‘felsic’ rocks rich in low density minerals like quartz and feldspar while the lowermost crust is less felsic and so denser. Assuming a typical basaltic magma density of 2800 kg m^{-3} and a crustal density structure shown in Fig. 2b there should be enough pressure for eruptions only if the magma is sourced from reservoirs like sills that are deeper than the ‘level of eruptibility’ at 27 km (Fig. 2c). For sills at shallower depths (Fig. 2d) the magma should not reach the surface even with an open conduit to the surface

Seismic velocities and densities beneath several LIPs are significantly higher than for typical continental crust. Figure 2e shows estimated compressional wave velocities based on a profile of crustal shear velocities beneath Deccan Traps^{15,16,32}. Applying the same linear velocity to density conversion, we find that the densities of the upper crust are markedly greater than that of average crust (Fig. 2f). This increase in upper crustal density means that magma from relatively shallow sills should be able to erupt (i.e. the ‘level of eruptibility’ is shallower, Fig. 2g). The denser crust of LIPs is likely due to basaltic crustal intrusions^{15,16}

We suggest that crustal densification due to voluminous magma intrusion and solidification is necessary to allow extrusion of continental flood basalts. The massive magma flux for an LIP is thought to originate in active upwellings of hotter-than-normal mantle³³. Partial melting occurs as mantle rises and so pressure decreases. The short duration of LIP magmatic events indicates that the plume induced melt flux increases and then decreases on a time scale shorter than a million years. The heat from the magma enables an intruded sill to heat up the overlying crust and allows rapid decrease in the intrusion depth during the phase of flux increase. As the melt flux wanes the crust above a sill should cool and the sill intrusion depth

deepens. Through this shallowing and deepening cycle, dense solidified mafic intrusions are emplaced into the crust, shifting the level of eruptibility.

Precise controls on sill opening depths are controversial, but temperature structure is almost certain to be a critical factor. Temperature affects the strength of rocks that must be deformed to allow opening. Temperature structure also controls the rate of cooling of magma in sills. Both effects mean that the hotter the crust the shallower the minimum depth of sill opening. Analytic relations between the heat released from intrusion and the steady-state temperature structure of the crust, described in the Methods, show that reasonable magma flux variations can produce the kinds of changes in sill depth required to cause extrusion late in the emplacements of an LIP.

Because crustal thermal structure does not respond instantaneously to changes in magmatic heat input, we need a time dependent model that includes diffusion and advection of heat as well as reasonable assumptions about controls on sill depth. The key question to test is whether a model can produce a major phase of extrusion starting a few hundred thousand years after the onset of detectable global warming that are caused by the CO₂ degassed from the preceding crustal magma intrusions.

We have experimented with several numerical sill intrusion models that can produce results that are consistent with observations but here we only discuss one that builds on a recent ‘multi-sill’ approach ³⁴. The model assumes Moho level magma reservoirs ²⁵ feed crustal sill intrusions that change the thermal and compositional structure of the crust. A new feature of our model is that it explicitly determines the depth of each sill intrusion. The onset of a shift of LIP magma emplacement from mostly intrusion with high frequency, episodic and small volume eruptions to mostly low frequency, stable and large volume eruptions ³⁵ is established when two

necessary conditions are met: first, the overburden of an active sill is on average denser than melt; second, the upward migrating magma from the shallowest active sill is not intruded laterally before reaching the surface. The model also assumes that the magma flux follows a Gaussian function in time and that magma solidifies shortly after emplacement. This solidification releases most CO₂ dissolved in the magma into the atmosphere. A standard Long-term Ocean-atmosphere-Sediment CArbon cycle Reservoir Model (LOSCAR)³⁶ is used to compute the effect of this CO₂ flux on global temperatures (see Methods for details).

The crustal magma sill intrusion system develops in four stages (Fig. 3). At stage one, the first sills are intruded into the mid-crust, warming the country rock and densifying the intruded region. As the melt supply increases, sills intrude at progressively shallower depths. The average density of the overburden of the intruding sills remains less than the magma density, so there are no major eruptions. Meanwhile, CO₂ exsolves from the cooling and solidifying melt and adds to the atmosphere.

Between stages one and two, a series of sills are emplaced upwards between ‘sill 1’ and ‘sill 2’ as melt flux increases. Significant heat is added to the crust at regions with sill intrusions. Again, there is no eruption at this time as the average density of the overburden is still less than that of magma. At stage three, as a series of sills are intruded into the mid-to-upper crust, hydrothermal circulation that transports heat to the surface increases its vigor due to the higher thermal gradient and permeability resulting from fractures induced by sill intrusions. However, the magma flux begins to decrease. Sill intrusions cannot exist shallower than the depth where heat lost to the surface is sustained by heat input from sill intrusions. Still no eruptions occur because the density of magma is still greater than the depth-averaged density of crust above the intruding sill.

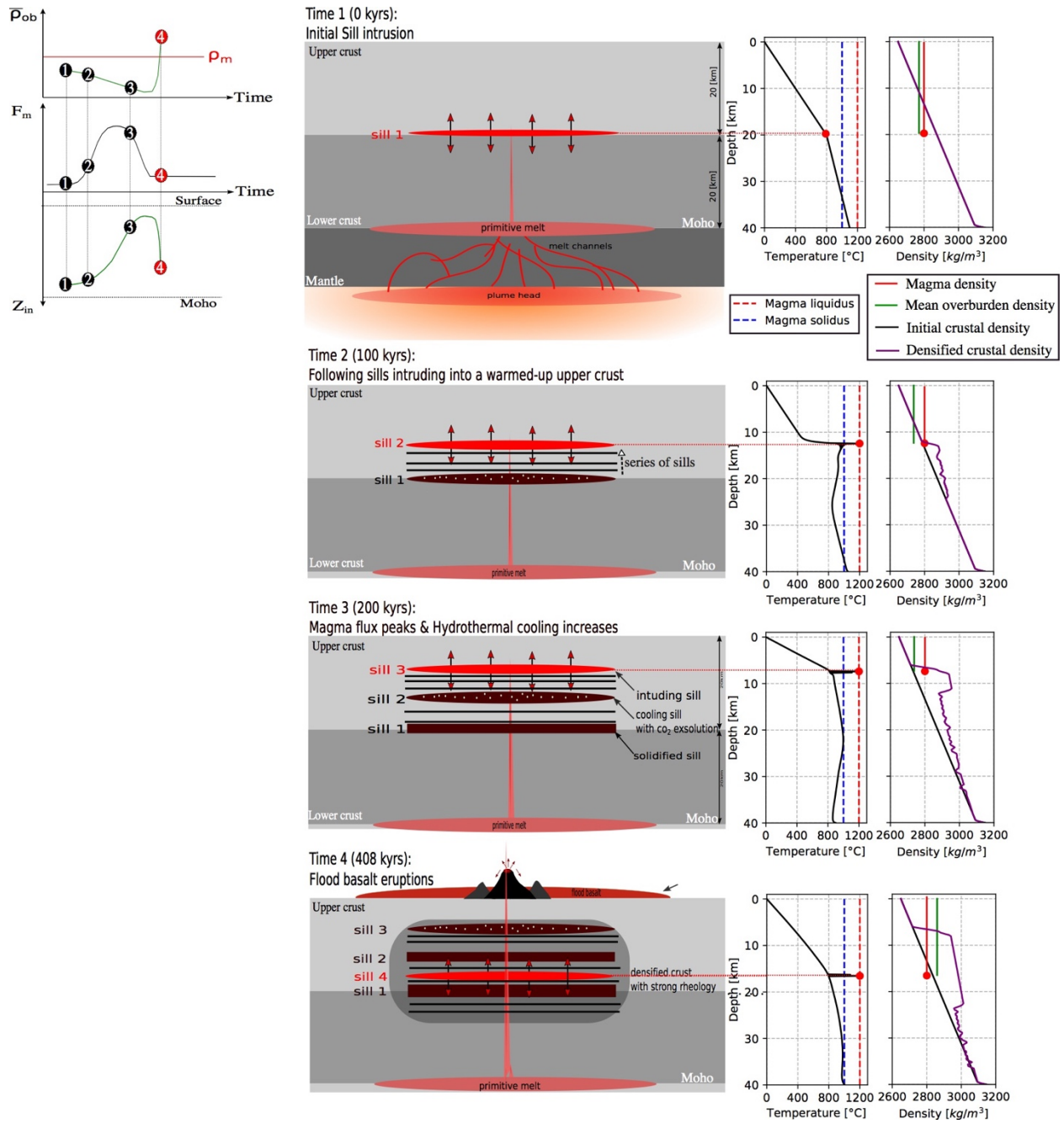


Fig. 3 | One dimensional thermo-mechanical model results showing the changes in crustal temperatures and densities due to evolving sill intrusions. Z_{in} is the intrusion depth, F_m is the magma flux, $\bar{\rho}_{ob}$ is the average density of the overburden and ρ_m is the magma density. The numbers 1 to 4 correspond to the stages of the system developments described in the text.

After several hundred thousand years of intrusion, the magma supply wanes while hydrothermal circulation is still vigorous. The intruded upper crust cools, solidifies and becomes

denser and stronger. The resistance to sill intrusion increases at shallow depths. At this point (stage four), sills intrude deeper into the hotter and weaker crust (Fig.3 ‘sill 4’). The average overburden density is now higher than that of fluid magma. With the densified and stronger crust preventing lateral intrusions above the active sill, magma from the intruding sill can directly erupt to the surface.

Figure 4 shows results from one model run that predicts a global warming signal similar to that seen for the Deccan Traps. The coupled LOSCAR model indicates that the intrusive CO₂ initiates a ~2 degrees global warming ~300 Kyr before the major phase of LIP volcanism. The time lag between the onset of predicted warming and the main extrusive phase depends on several model parameters, including: the magma flux through time; the radius of magma sills; the initial thermal, compositional and density structures of the crust and the efficiency of hydrothermal heat transport in the shallow crust. Without assuming vigorous effective hydrothermal cooling of the shallow crust, the modeled time lag between intrusive and extrusive onsets is longer than observed.

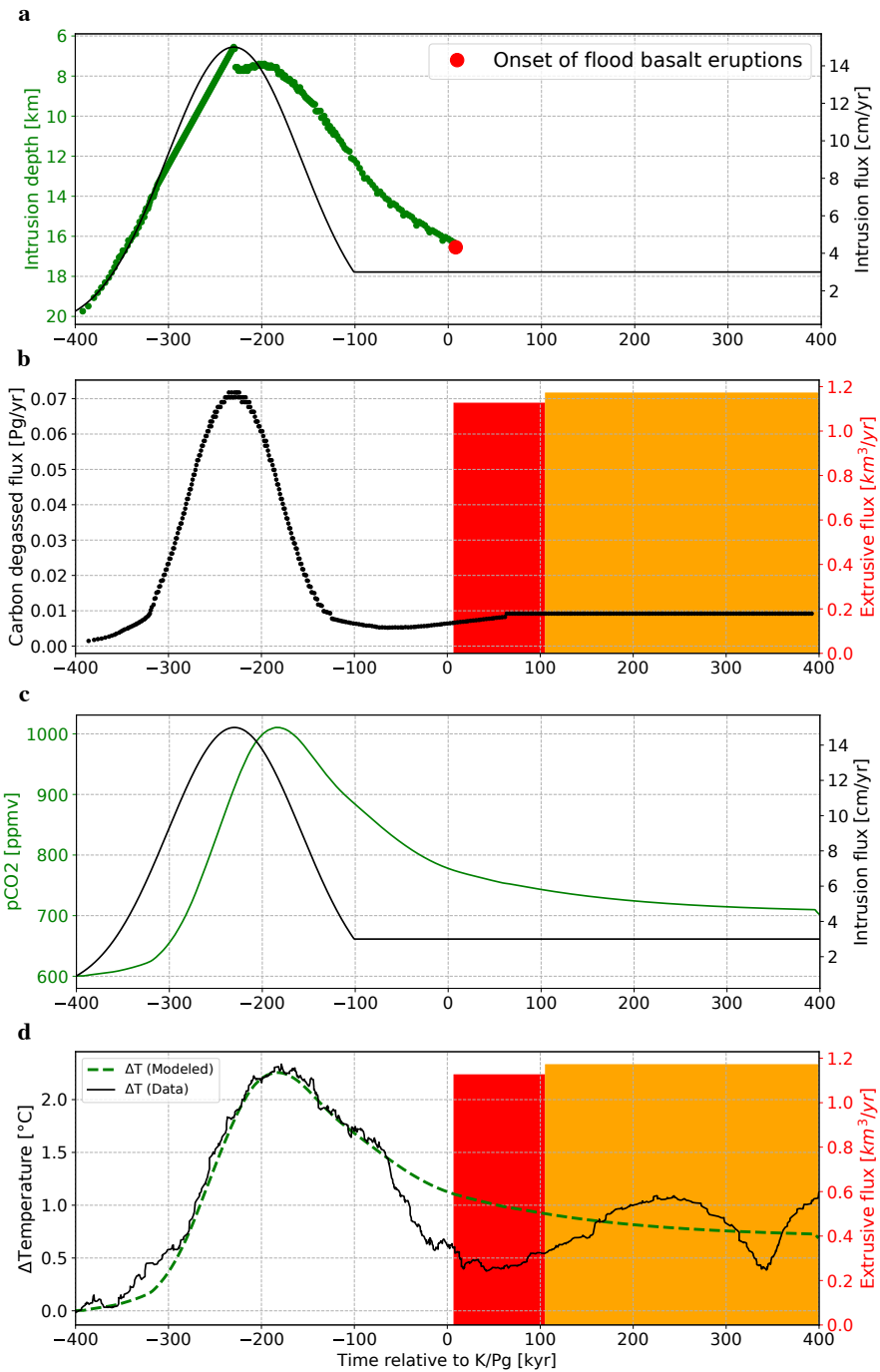


Fig. 4 | Time series of modeled global temperature and erupted flux of flood basalts. **a**, sill intrusion depth and the timing of transition from mostly intrusion to major phase of extrusion, predicted by the thermo-mechanical model described in the Methods, given the indicated melt flux with time. **b**, modeled CO₂ outgassing flux and the predicted extrusive flux. **c**, global averaged atmospheric CO₂ concentration with time predicted by the LOSCAR climate model. **d**, global temperature change predicted by the LOSCAR model along with the extrusive flux with time to compare with the observation in Fig. 1a.

Our model suggests that intrusion induced densification of the continental crust is necessary for large-scale flood basalt eruptions. Massive CO₂ degassing from the solidifying intrusion can cause global warming. This provides a possible explanation for the decoupled climate signal and flood basalt flux. It could also help explaining main phase of several mass extinctions predates the onset of their related LIP eruptions ³⁷.

Several observations support our model. A key assumption that CO₂ exsolves at depth as magma crystalize is supported by a recent melt inclusion study of LIP lavas which indicates mid-to-lower crustal exsolution of the bulk of CO₂ ²⁰. Another requirement of the model is that magma sill intrusions should migrate upwards and downwards within several hundred kyr to densify the crust and induce the state shift of magma emplacements. That even modest sized mantle plumes can produce shallow magma emplacement is evidenced by seismic data indicating a large volume of partially molten crust less than 10 km below Yellowstone where high heat flux up to 2000 mWm⁻² was also reported ²². Additionally, petrological studies of the Deccan Traps, the CRB and some other LIPs reveal a common trend of increasing primitiveness of the erupted magma with time ^{18,35,38}. This trend is consistent with our model in that early smaller volume extrusions should interact more with the crust while later major flood basalts do not reside for long periods in the crust.

Many previous studies assume the main climatic effect of LIPs results from the carbon liberated by surface lava flows. Because the volume of CO₂ released directly from such flood basalts may be less than is needed to produce observed increases in global temperatures, several groups invoke sources of extra carbon including ‘cryptic’ degassing ³⁹ either by sill intrusion heating of carbon-rich sedimentary strata ²¹ or by a carbon-rich plume melting releasing CO₂ deep in the mantle ⁴⁰. However, besides requiring high carbon concentrations, these authors do

not quantify the climatic response of the CO₂ release and explain the time lag between the global warming and the major eruption phase. As noted earlier, the volume of magma intruded deep in the crust during LIP formation may be an order of magnitude greater than that reaching the surface. Thus, the CO₂ released from those deep intrusions may be the main driver of the observed global warming and associated extinction events.

Magmatic processes are undeniably far more complex than the crude models considered here. However, the simple models described here show that reasonable changes in the thermal and density structures of the crust during massive magmatic events could lead to the bulk of intrusion happening before the major phase of continental flood basalt extrusions on the observed time scale of several hundred thousand years.

References:

1. Courtillot, V. E. & Renne, P. R. On the ages of flood basalt events. *Comptes Rendus Geosci.* **335**, 113–140 (2003).
2. Coffin, M. F. & Eldholm, O. Large igneous provinces: Crustal structure, dimensions, and external consequences. *Rev. Geophys.* **32**, 1 (1994).
3. Jones, M. T., Jerram, D. A., Svensen, H. H. & Grove, C. The effects of large igneous provinces on the global carbon and sulphur cycles. *Palaeogeogr. Palaeoclimatol. Palaeoecol.* **441**, 4–21 (2016).
4. Sprain, C. J. *et al.* The eruptive tempo of Deccan volcanism in relation to the Cretaceous-Paleogene boundary. *Science (80-).* **363**, 866–870 (2019).
5. Kasbohm, J. & Schoene, B. Rapid eruption of the Columbia River flood basalt and correlation with the mid-Miocene climate optimum. *Sci. Adv.* **4**, eaat8223 (2018).
6. Black, B. A. & Gibson, S. A. Deep Carbon and the Life Cycle of Large Igneous Provinces. *Elements* **15**, 319–324 (2019).
7. Hull, P. M. *et al.* On impact and volcanism across the Cretaceous-Paleogene boundary. *Science (80-).* **367**, 266–272 (2020).
8. Holbourn, A., Kuhnt, W., Kochhann, K. G. D., Andersen, N. & Sebastian Meier, K. J. Global perturbation of the carbon cycle at the onset of the Miocene Climatic Optimum. *Geology* **43**, 123–126 (2015).
9. Westerhold, T. *et al.* An astronomically dated record of Earth's climate and its predictability over the last 66 million years. *Science (80-).* **369**, 1383–1387 (2020).
10. Townsend, M., Huber, C., Degruyter, W. & Bachmann, O. Magma Chamber Growth During Intercaldera Periods: Insights From Thermo-Mechanical Modeling With Applications to Laguna del Maule, Campi Flegrei, Santorini, and Aso. *Geochemistry, Geophys. Geosystems* **20**, 1574–1591 (2019).
11. Ward, K. M., Zandt, G., Beck, S. L., Christensen, D. H. & McFarlin, H. Seismic imaging of the magmatic underpinnings beneath the Altiplano-Puna volcanic complex from the joint inversion of surface wave dispersion and receiver functions. *Earth Planet. Sci. Lett.* **404**, 43–53 (2014).
12. White, S. M., Crisp, J. A. & Spera, F. J. Long-term volumetric eruption rates and magma budgets. *Geochemistry, Geophys. Geosystems* **7**, 1–2 (2006).
13. Crisp, J. A. Rates of magma emplacement and volcanic output. *J. Volcanol. Geotherm. Res.* **20**, 177–211 (1984).
14. Ridley, V. A. & Richards, M. A. Deep crustal structure beneath large igneous provinces and the petrologic evolution of flood basalts. *Geochemistry, Geophys. Geosystems* **11**, Q09006 (2010).
15. Sen, G. & Chandrasekharam, D. Deccan Traps Flood Basalt Province: An evaluation of the thermochemical plume model. In Topics in igneous petrology (pp. 29-53). in *Topics in Igneous Petrology* 29–53 (Springer, Dordrecht, 2011).
16. Pandey, O. P. Deccan trap volcanic eruption affected the Archaean Dharwar craton of southern India: Seismic evidences. *J. Geol. Soc. India* **72**, 510–514 (2008).
17. Catchings, R. D. & Mooney, W. D. Crustal structure of the Columbia Plateau: Evidence

- for continental rifting. *J. Geophys. Res. Solid Earth* **93**, 459–474 (1988).
18. Moore, N. E., Grunder, A. L. & Bohrson, W. A. The three-stage petrochemical evolution of the Steens Basalt (southeast Oregon, USA) compared to large igneous provinces and layered mafic intrusions. *Geosphere* **14**, 2505–2532 (2018).
 19. Rosenthal, A., Hauri, E. H. & Hirschmann, M. M. Experimental determination of C, F, and H partitioning between mantle minerals and carbonated basalt, CO₂/Ba and CO₂/Nb systematics of partial melting, and the CO₂ contents of basaltic source regions. *Earth Planet. Sci. Lett.* **412**, 77–87 (2015).
 20. Capriolo, M. *et al.* Deep CO₂ in the end-Triassic Central Atlantic Magmatic Province. *Nat. Commun.* **11**, 1670 (2020).
 21. Svensen, H. *et al.* Release of methane from a volcanic basin as a mechanism for initial Eocene global warming. *Nature* **429**, 542–545 (2004).
 22. Huang, H.-H. *et al.* The Yellowstone magmatic system from the mantle plume to the upper crust. *Science (80-.)* **348**, 773–776 (2015).
 23. Lee, H. *et al.* Massive and prolonged deep carbon emissions associated with continental rifting. *Nat. Geosci.* **9**, 145–146 (2016).
 24. Mutch, E. J. F., MacLennan, J., Holland, T. J. B. & Buisman, I. Millennial storage of near-Moho magma. *Science (80-.)* **365**, 260–264 (2019).
 25. Karlstrom, L. & Richards, M. On the evolution of large ultramafic magma chambers and timescales for flood basalt eruptions. *J. Geophys. Res. Solid Earth* **116**, B08216 (2011).
 26. Black, B. A. & Manga, M. Volatiles and the tempo of flood basalt magmatism. *Earth Planet. Sci. Lett.* **458**, 130–140 (2017).
 27. Ernst, R. E., Liikane, D. A., Jowitt, S. M., Buchan, K. L. & Blanchard, J. A. A new plumbing system framework for mantle plume-related continental Large Igneous Provinces and their mafic-ultramafic intrusions. *J. Volcanol. Geotherm. Res.* **384**, 75–84 (2019).
 28. Hooft, E. E. & Detrick, R. S. The role of density in the accumulation of basaltic melts at mid-ocean ridges. *Geophys. Res. Lett.* **20**, 423–426 (1993).
 29. Buck, W. R., Carbotte, S. M. & Mutter, C. Controls on extrusion at mid-ocean ridges. *Geology* **25**, 935 (1997).
 30. Christensen, N. I. & Mooney, W. D. Seismic velocity structure and composition of the continental crust: a global view. *J. Geophys. Res.* **100**, 9761–9788 (1995).
 31. Stolper, E. & Walker, D. Melt density and the average composition of basalt. *Contrib. to Mineral. Petrol.* **74**, 7–12 (1980).
 32. Brocher, T. M. Empirical Relations between Elastic Wavespeeds and Density in the Earth's Crust. *Bull. Seismol. Soc. Am.* **95**, 2081–2092 (2005).
 33. White, R. S. & McKenzie, D. Mantle plumes and flood basalts. *J. Geophys. Res. Solid Earth* **100**, 17543–17585 (1995).
 34. Annen, C., Blundy, J. D. & Sparks, R. S. J. The Genesis of Intermediate and Silicic Magmas in Deep Crustal Hot Zones. *J. Petrol.* **47**, 505–539 (2006).
 35. Renne, P. R. *et al.* State shift in Deccan volcanism at the Cretaceous-Paleogene boundary, possibly induced by impact. *Science (80-.)* **350**, 76–78 (2015).
 36. Zeebe, R. E., Zachos, J. C. & Dickens, G. R. Carbon dioxide forcing alone insufficient to

- explain Palaeocene–Eocene Thermal Maximum warming. *Nat. Geosci.* **2**, 576–580 (2009).
- 37. Wignall, P. B. Large igneous provinces and mass extinctions. *Earth-Science Rev.* **53**, 1–33 (2001).
 - 38. Yu, X., Lee, C. T. A., Chen, L. H. & Zeng, G. Magmatic recharge in continental flood basalts: Insights from the Chifeng igneous province in Inner Mongolia. *Geochemistry, Geophys. Geosystems* **16**, 2082–2096 (2015).
 - 39. Armstrong McKay, D. I., Tyrrell, T., Wilson, P. A. & Foster, G. L. Estimating the impact of the cryptic degassing of Large Igneous Provinces: A mid-Miocene case-study. *Earth Planet. Sci. Lett.* **403**, 254–262 (2014).
 - 40. Sobolev, S. V. *et al.* Linking mantle plumes, large igneous provinces and environmental catastrophes. *Nature* **477**, 312–316 (2011).

Appendix 3: Methods

To consider the timing between flood-basalt volcanism and global climate response due to emplacement of a Large Igneous Province (LIP), we develop two versions of a thermo-mechanical sill intrusion model. For a given variable magma flux with initial crustal thermal, density, compositional structures, these models estimate temporal changes of the density and thermal structure of continental crust. These changes govern the predicted onset of the major phase of flood basalt volcanism. The model CO₂ degassing flux is then used as an input variable to the Long-term Ocean-atmosphere-Sediment CArbon cycle Reservoir Model (LOSCAR)^{36,41} for its climatic response.

As described in the main text, a key assumption of the model is that the initiation of the major phase of flood basalt volcanism is declared when two conditions are met: first, the overburden of an active sill is on average denser than melt; second, the upward migrating magma from the shallowest active sill is not intruded laterally before reaching the surface. The first condition is determined by the crustal density structure and the depth of the intruding sill and the second condition is controlled by the thermo-mechanical state of the crust.

A sill intrusion of basaltic magma into continental crust affects both the thermo-mechanical state and density structure of the crust, which further affects where the following sill intrusions are most likely to happen and whether the two necessary conditions are met for large-scale flood basalt eruptions to occur. Here we first give details of a simplified analytic model and then a more complex multi-sill model that treat such intrusion related crustal changes. The purpose of these models is to see whether a model with reasonable assumptions and parameter values can produce significant magma intrusion followed by flood basalt eruption several hundred thousand years later. A key output is the predicted time lag between the onset of

significant global warming signal related to CO₂ release from solidifying magma intrusion and the onset of major phase of flood basalt extrusion. Before describing the simplified analytic model and the more complex multi-sill model we describe the assumptions and parameter values common to both approaches.

A3-1. Common Model Features

One-dimensional Thermal Model

We treat crustal magma emplacement as numerous discrete basaltic sill intrusions similar to previous models ^{34,42}. We assume that each magma sill is emplaced instantly at its liquidus temperature and only account for the vertical transfer of heat, mass and stress. The assumption of instant emplacement is reasonable because thermal diffusion is much slower than the propagation of a sill intrusion. Only considering the changes in vertical z-axis direction is justifiable when a sill has a lateral dimension much larger than its thickness and depth so that the lateral heat transport is negligible. This wide but thin geometry of sills also allows us to neglect flexural response due to the loads of intrusions, which is small when compared to vertical movement of isostatic adjustment. The initial crustal thickness is taken to be close to the global average of 40 km ³⁰. The surface is always kept at 0 °C. Convection of water through pore spaces in the shallow crust is considered to enhance heat transfer and we follow other workers (refs. ^{43,44}) who approximate this effect by taking the effective conductivity of the crust to be multiplied by a factor Nu (after the Nusselt number for steady-state convection).

The evolution of temperatures with depth and time t are described by the one-dimensional heat equation:

$$\frac{\partial T(z, t)}{\partial t} = Nu(z, t)\kappa \frac{\partial^2 T}{\partial z^2} - v(t) \frac{\partial T}{\partial z} + \frac{H_m}{\rho(z)C_p} \quad (1)$$

where $T(z, t)$ is temperature as a function of depth z (positive downward) and time t , $Nu(z, t)$ is a dimensionless pre-factor describing enhanced heat transfer efficiency as a function of depth z and time t , thermal diffusivity $\kappa = 10^{-6} [m^2/s]$, $v(t)$ is the downward advection velocity of crust beneath the intruding sill and is equal to the sill thickening rate $F_m(t)$ which is also the magma supply flux per unit area. H_m with a unit of $[W/m^3]$ is the heat liberation or storage rate which accounts for heat liberated on cooling and solidification of basaltic melt and heat stored on melting of solid basalt. $\rho(z)$ is density and $C_p = 1400 [J/(kg \cdot K)]$ is specific heat. The magma in sills is assumed to solidify shortly after emplacement as the time scale for thermal diffusion of a hundred-meters-thick sill is two orders of magnitude shorter than the observed time lag between onsets of warming and eruption. Here, for simplicity, we ignore the crustal radiogenic heat production.

Assumed Magma Flux

The flux of magma added to the crust is taken to vary in time according to a Gaussian function with a constant tail:

$$F_m(t) = \begin{cases} F_m^0 \exp(-(t - t_0)^2/2c^2), & t < t_1 \\ F_m^1, & t \geq t_1 \end{cases} \quad (2)$$

where F_m^0 is the maximum flux at time t_0 and F_m^1 is the constant flux after time t_1 when $t > t_0$ and $F_m^0 \exp(-(t_1 - t_0)^2/2c^2) = F_m^1$, c controls the width in time of the Gaussian function. $F_m^0 \exp(-(t - t_0)^2/2c^2)$ represents the crustal magma intrusion flux being generated by a mantle plume head and F_m^1 represents a plume tail induced magma flux. In our one-dimensional treatment the flux has units of volume flux/area ($[m/s]$).

Assuming a radius R of the circular disk-like sill intrusions, the volume flux of magma intrusion is then easily calculated as $V_m(t) = F_m(t)\pi R^2$. R is assumed to be 1000 times of the thickness of the sills emplaced during one modeled intrusion episode. Studies on concentrations

of Ba and Nb in picrites suggest a 0.1~2 weight percent (wt%) of CO₂ concentration in the original mantle derived magma ^{45,46} and we here assume this concentration to be 1.5 wt% for the multi-sill model and 1.2 wt% for the analytic model, with degassing efficiencies of 55% for intrusion and 70% for extrusion ^{6,47}, depending on the timing of declaration of main phase of flood basalt eruptions, the model results in a time series of CO₂ outgassing flux (Fig. 4b). The modeled CO₂ outgassing flux is then used as an input into a multi-box long-term carbon cycle and climatic response model described below.

The initial density structure of continental crust $\rho_c(z, t = 0)$ is simplified according to ref. ³⁰ with a linear fit that increases from 2650 kg/m³ at the surface to 3100 kg/m³ at the Moho at $L_M = 40$ km (Fig. 2b). The crustal density structure $\rho_c(z, t)$ changes with intrusions of fluid magma of 2800 kg/m³ which increases to a depth dependent density $\rho_s(z) = 2900 + 200 \times (\frac{z}{L_M})$ kg/m³ for solidified basalt (Fig. 3).

A3-2. LOSCAR climate model

We use the Long-term Ocean-Sediment CArbon Reservoir model (LOSCAR), v 2.0.4.3 ^{36,41} to simulate the global temperature response to the CO₂ outgassing during an LIP emplacement. Our model setup and parameters follows that of refs. ^{7,48}. Specifically, we set [Mg2+] = 42 mmol/kg and [Ca2+] = 21 mmol/kg as equilibrium constants for carbonate chemistry calculations for K/Pg seawater. Sediment depth resolution was divided with the standard 500 m interval rather than the previously used more finely subdivided 100 m depth intervals because both show similar results but the models with a finer resolution take more than twenty times longer in our cases. The exponential constant (n_{si}) used in the silicate weathering feedback equation was 0.6 following refs. ^{7,48}. A pre-event baseline pCO₂ of 600 ppm was used after refs. ^{7,48} by restarting the model with pre-calculated steady state model parameters. The

calculated global temperature response due to CO₂ outgassing from the LIP emplacement is presented in Fig. 4d of the main text. Note that exact curve fitting of the global temperature could be possible but is not the point of this study, rather, we here try to demonstrate quantitatively with reasonable and well-studied controlling parameters that our coupled sill intrusion and LOSCAR models are capable of predicting similar patterns of climate and LIP behaviors when compared to the observations.

A3-3. Analytic sill intrusion model

To demonstrate the plausibility of our conceptual model for significant intrusion before continental flood basalt extrusion we first consider a simplified analytic version based on a balance of thermal energy. The temperature structure of the crust above intruding sills is assumed to reach steady state ($\partial T(z, t)/\partial t = 0$) immediately with the changes of magma supply flux. This is purely for the sake of analytic simplification and induces inaccuracy in time for temperature changes, which is treated more realistically in the multi-sill model described later. For this approach the domain of interest is between the surface and the top of an intruding sill so we neglect effects of downward crustal advection beneath the intruding sill ($v = 0$). Over this domain, we only consider the liberation of heat ($H_m/(\rho(z)C_p)$) from the sill as a bottom heat flux boundary condition and temperature correlates linearly with depth. The thermal equation 1 is then simplified to:

$$Nu(z, t)\kappa \frac{\partial^2 T}{\partial z^2} = 0 \quad (3)$$

Integrating equation 3 with respect to depth z and assuming that at the bottom boundary the heat flux (Q_{sill}) is sourced from the cooled and solidified sill with a constant Nu yields:

$$Nu \times k \frac{\partial T}{\partial z} = Q_{sill} \quad (4)$$

Where $k = \kappa\rho_f C_p = 3.3$ [W/mK] is the constant thermal conductivity of crustal rocks. The heat flux coming from the sill is taken to be:

$$Q_{sill} = F_m(t) \times \rho_f (L + (T_l - T_s)C_p) \quad (5)$$

where $\rho_f = 2800$ [kg/m³] is the density of the fluid magma and $L = 4 \times 10^5$ [J/kg] is the latent heat of solidification, $T_s = 1000$ °C is the magma solidus and $T_l = 1200$ °C is the magma liquidus. Applying a top boundary condition of $T(0, t) = 0$ °C and a moving bottom boundary condition of $T(Z_{in}, t) = T_s$ where Z_{in} is the evolving sill intrusion depth, we have a thermal gradient of $\partial T / \partial z = (T_s - T(0, t)) / Z_{in}$, which is plugged into equation 4 and 5 to determine the intrusion depth as:

$$Z_{in} = \frac{Nu \times k \times T_s}{F_m \rho_f (L + (T_l - T_s)C_p)} \quad (6)$$

For the example used here we assume the plume head is controlled by $F_m^0 = 15$ cm/yr, $t_0 = 170$ kyrs and $c = 210\sqrt{2/\pi}$ kyrs followed by a plume tail of constant $F_m^1 = 6$ cm/yr thickening rate. Extended Data Fig. 1a shows this example flux-time curve and Extended Data Fig. 1b shows the resulting variation of the intrusion depth given by equation 6. This sill intrusion depth along with the density structure and an assumed critical overpressure for initiation of eruptions $\Delta P_c = 10$ MPa^{10,49,50}, determines whether magma can extrude subaerially or is intruded within the crust. We also assume that deepening of sill intrusions is taken to imply replacement of felsic continental crust with denser basaltic rocks. This densification of the crust then affects the depth where magma in a sill can be erupted which is termed as ‘level of eruptibility’ (see main text). For extrusion to occur there has to be enough pressure in the magma sill to drive the magma to the surface. We assume that the pressure in the magma sill is just the overburden pressure:

$$P_{OB}(Z_{in}, t) = \int_0^{Z_{in}} \rho_c(z, t) g \, dz \quad (7)$$

where $\rho_c(z, t)$ is the crustal density profile. We determine the magma eruptibility by whether the magma pressure head $P_h(z, t)$ at the surface ($z = 0$) is larger than ΔP_c when sourced from the intruding sill at depth Z_{in} , where

$$P_h(0, t) = P_{OB}(Z_{in}, t) - \rho_f g Z_{in} \quad (8)$$

and this is equivalent to whether the overburden of the intruding sill is on average denser than fluid magma to an extent that:

$$\bar{\rho}_{ob} > \rho_f + \Delta P_c / g Z_{in} \quad (9)$$

Where $\bar{\rho}_{ob}$ is the average overburden density.

Flood basalt eruptions then could happen in two ways. If the initial sills are deeper than the level of eruptibility then the condition is met so extrusion could occur. This might only happen when the initial magma flux is low and the intrusion is deep. Alternatively, a sill can move up to a depth much shallower than the level of eruptibility and then move downward as mafic magma in the sill cools and crystallizes. The sill intrusion moves downward as the flux of magma wanes and so the heat released by the magma decreases (as indicated in Extended Data Fig. 1b). We assume that as the sill moves down it leaves behind intrusions with the density of solid basalt ($\rho_s(z)$). Now the overburden will be a mix of initial low-density felsic crust and higher density solidified basalt. For a linear increase of initial crustal density with depth (Fig. 2a) eruption can happen if:

$$Z_{in} \geq \frac{[\rho_s(Z_{inm}) + \rho_s(Z_{in}) - \rho_c(0) - \rho_c(Z_{inm})] \times Z_{inm} + 2\Delta P_c / g}{\rho_s(Z_{inm}) + \rho_s(Z_{in}) - 2\rho_f} \quad (10)$$

where $Z_{inm} = \frac{Nu \times k \times T_s}{F_m^0 \rho_f (L + (T_l - T_s) C_p)}$ is the minimum depth of the sill intrusions. When this condition is met the magma pressure head at the surface is greater than ΔP_c , the critical pressure

for initiating an eruption. Extended Data Fig. 1c shows how magma pressure head varies in time. Once the timing of the onset of eruptions is determined, the model predicts a CO₂ degassing flux given the assumed magma concentration and degassing efficiencies. Using the CO₂ degassing flux as an input for the LOSCAR model we can calculate the global averaged atmospheric CO₂ concentration (Extended Data Fig. 1d) and temperature changes (Extended Data Fig. 1e) with time relative the K/Pg boundary.

A3-4. Multi-sill intrusion model

Our multi-sill intrusion model builds upon previous numerical studies on the genesis and evolution of evolved crustal magmas ^{34,42}. By accounting for heat transfer and mass advection during repetitive sill intrusions, such models can quantify changes in melt fraction and chemical compositions of the mantle plume induced magma that intrudes into the crust and mixes with crustal melts. As we are concerned with magma eruptibility rather than the chemical evolution of the system, our approach neglects chemical reactions of the magma and country rock. We focus on how changes in crustal temperature and composition structures control the depth of sill intrusions and the density structure of the crust.

We argue in the main text that the depth of sill intrusion is important for determining whether magma emplaces as intrusions or eruptions. Some studies assume an initial intrusion depth and that subsequent sills are emplaced over, under or within the earlier sills ^{34,42}. Other studies treat sill intrusion depths through time as stochastic processes ^{51,52}. As noted below, there is considerable evidence that the thermal structure of the crust has a large influence on the depth of sill intrusion. It is also clear that sill intrusion alters the crustal temperature structure and so can lead to an evolution of sill intrusion depths. Because crustal thermal structure does not respond instantaneously to changes in magmatic heat input, we derive a time dependent model

that includes diffusion and advection of heat as described by equation 1. Before describing that model, we briefly review some recent studies for sill intrusion.

One of the most discussed ideas about sill opening depth is that magmatic sills form at the ‘level of neutral buoyancy’ (LNB)⁵³. This model assumes that crustal density increases with depth and that magma pools at the LNB where the country rock density equals the magma density. This works in analog laboratory models only if the ‘crustal’ material has negligible strength. However, many observations are at odds with the LNB concept (see^{54,55} and references therein). For example, this idea was tested by Hooft and Detrick²⁸ at mid-ocean ridges where seismic observations are of sufficient quality to determine the density structure above the magma filled sills. They showed that the sills were located deeper than the LNB and they suggested that the strength of cold crust may be important. Some other studies imaged sill intrusions within lower density sedimentary basins which situate shallower than the LNB (e.g.⁵⁶ and references therein).

Some previous workers focus on the effects of mechanical strength changes across layers which deflect a dike into sills and hence the sill intrusion depth is determined by the location of the layer boundary^{54,57}. A recent analogue model study summarizes that buoyancy pressure from density contrast between host rock and the injecting fluid, rigidity contrast and lateral compression are the major controls on formation of sills⁵⁸. Menand⁵⁴ reviewed existing models for sill emplacement depths as controlled by four major factors: (1) the buoyancy pressure due to the density contrast between host rock and injecting fluid, (2) the rigidity contrast between strata, (3) the rheology control between warm ductile material and cold brittle material, and (4) rotation of deviatoric stress. These four factors can be further grouped into two major effects: either from buoyancy driving pressure controlled by density structures or effective resistant strength

structure controlled by rigidity, rheology or stress state. All these factors are functions of temperature which makes sill intrusion depth strongly dependent on thermal structures.

Morgan and Chen⁵⁹ were the first to suggest that temperature was critical in controlling the depth of magma lens at mid-ocean ridges. A recent three-dimensional numerical modeling study of magma intrusion into the continental crust indicates that rheology and temperature of the host rocks are the key controls of how magma is emplaced⁶⁰. Parsons et al.⁶¹ first suggested that at large rheology contrasts where lower viscosity ductile layers are adjacent to higher viscosity elastic layer, the least principal stress can be rotated vertically due to horizontal dike opening. This rotation of the least principal stress can arrest upward dike propagation and induce lateral sill intrusions. Similar behavior of dike arrest is described by⁶² for rifts where lithosphere-cutting dikes stop when the ‘driving pressure’ (magma pressure minus lithospheric stress normal to the dike wall) is too small. This idea has also been used to explain analogue model results showing that horizontal compressive stress can modify the path of fluid crack from vertical to horizontal⁶³.

Here, we assume that sill intrusion depth evolves with the thermo-mechanical state and density structure following previous studies of effects of thermal and stress states on sill formations^{59,61}. For a column of magma rising through crust with density that increases with depth, the magma overpressure (magma pressure minus lithostatic pressure define here as driving pressure P_d) will be greatest at the level of neutral buoyancy. However, if the rocks are cold and strong at this depth the magma should not be able to force a sill to open. We estimate the resistance to sill opening as resistance pressure (P_r). P_r depends partly on the host rock temperature in that it controls whether magma will freeze before the sill intrusions can be open. P_r depends also on the composition and temperature controlling horizontal stress ($\sigma_h(z, t)$)

which acts normal to the vertical dike opening wall, because it controls where a vertical sill feeding dike is stopped due to smaller driving pressure relative to that of the horizontal compressive stress. We assume that a sill opens where the breakout pressure ($P_{BK} = P_d - P_r$), namely the difference between the driving pressure P_d and the resistance pressure P_r is the largest as the maximum breakout pressure ($P_{BK}(Z_{in}) = P_{BKm}$) (Extended Data Fig. 2).

The driving pressure for sill intrusion is computed by integrating density difference between the fluid magma ρ_f and the country rock ρ_c along a vertical melt migration conduit upward from the Moho level reservoir:

$$P_d(z) = \int_{Z_{moho}}^z (\rho_c - \rho_f) g \, dz \quad (11)$$

This neglects any viscous pressure changes due to flow of the low viscosity primitive magma. For the driving pressure P_d , although the density difference between fluid magma and mantle country rock can be large, we assume the magma generated from the mantle plume gains negligible pressure head as it percolates through the low permeability melt channels in the upper mantle. Magma is assumed to then accumulate in the Moho-level magma reservoirs similar to that of previous studies of continental intrusions^{25,26,55}.

The resistance pressure P_r comes from two parts, namely, the thermal arrest pressure P_{TA} and the remained (un-relaxed) dike opening induced horizontal compressive stress σ_h . P_{TA} is the required magma pressure for sustaining a thin but laterally wide sill intrusion. We estimate this pressure following previous ‘thermal entry’ length calculations^{64,65}, which consider the pressure needed to drive magma to flow a long distance before freezing. Here, we assume a sill of thickness $w = 1$ meter and a flow distance $R_{fz} = 200$ km before the magma fully freezes. The magma propagation in such a sill is assumed to be simplified as a thin channel flow with an average velocity of:

$$\bar{u} = \frac{w^2}{12\eta_m} \frac{dP}{dx} \quad (12)$$

where pressure gradient $dP/dx = P_{TA}/R_{fz}$, assuming stable source pressure of P_{TA} ⁶⁶ and $\eta_m = 100 \text{ Pa} \cdot \text{s}$ is the assumed viscosity for fluid magma following⁶⁷. Then the thermal arrest pressure P_{TA} to drive a high aspect ratio thin channel sill intrusion before it freezes is:

$$P_{TA} = \frac{192 \times \kappa \times \eta_m \times R_{fz}^2 \times \lambda^2}{w^4} \quad (13)$$

where κ is the thermal diffusivity. The freezing distance $R_{fz} = \bar{u}t_{fz}$ is calculated assuming a freezing time $t_{fz} = w^2/(16\kappa\lambda^2)$, which is the approximate time for a thin channel fluid magma flow with thickness of w to freeze and λ is a dimensionless parameter determined by temperature of the country rock at the sill intrusion depth $T(Z_{in})$ ^{65,68} and is expressed in an implicit function only solved numerically:

$$\lambda = \frac{\exp(-\lambda^2)}{\pi^{\frac{1}{2}} S} \left[\frac{\theta}{erfc(-\lambda)} - \frac{1-\theta}{erfc(\lambda)} \right] \quad (14)$$

Where dimensionless solidus temperature $\theta = [T_s - T(Z_{in})]/[T_l - T(Z_{in})]$, and the Stefan number $S = L/[C_p(T_l - T(Z_{in}))]$, where T_s is the solidus temperature and T_l is the liquidus temperature, here taken to be the intrusion temperature.

A vertical dike is assumed to propagate quasi-periodically upward to feed sill intrusions from the magma reservoir at the base of the crust. As the dike opens it induces an instant elastic increase in the lateral compressive stress. If the dike freezes in cold and strong crust that behaves mainly elastically, the compressive stress increase can remain for a long period of time and this should inhibit vertical propagations of later dikes. If the dike intrudes and freezes in hotter and lower viscosity crust, the initial increase in lateral compressive stress can be effectively relaxed between dike events. Following the model of Parsons et al.,⁶¹ that a sill can

form at brittle-ductile transitions, we calculate the second part of the model resistant pressure as the temporally variable horizontal stress $\sigma_h(z, t)$ induced by a dike opening. Assuming the crust behaves as a Maxwell viscoelastic material⁶⁶ with laboratory constrained properties^{69,70} we can estimate the amount of stress relaxation between intrusion events as functions of temperature and assumed composition. When a dike propagates vertically and opens laterally with pressure distribution of magma driving pressure $P_d(z)$, it induces a compressive horizontal stress $\sigma_h(z, t = 0) = P_d(z)$, which relaxes quickly at low viscosity regions. During the quasi-periodic intersessions of Δt (on the order of a few thousand years depending on the magma flux) between intrusions, this initial dike induced horizontal compressive stress $\sigma_h(z, t = 0)$ relaxed to $\sigma_h(z, t = \Delta t)$ following a Maxwell relaxation stress relation⁶⁶:

$$\sigma_h(z, t = \Delta t) = \sigma_h(z, t = 0) \exp\left(-\frac{E\Delta t}{2\mu}\right) \quad (15)$$

where the assumed Young's modulus $E = 30 \text{ GPa}$ ⁴⁴, and the strain rate independent viscosity of the country rock μ is calculated according to⁴³ with the power $n = 1$:

$$\mu = (3A)^{-1} \times \exp\left(\frac{Q}{nRT(Z_{in})}\right) \quad (16)$$

where A is an empirical lab-determined viscosity pre-factor, Q is the activation energy, R = 8.314 [J/(mol · K)] is the gas constant. For upper crust, we use lab constrained equivalent Newtonian flow rule with $A = 0.0052 \text{ [MPa}^{-1}\text{s}^{-1}\text{]}$ (calculated from $2/3 \times 1.57 \times (1e-3) \times 50^{0.41}$) and $Q = 131500 \text{ [J/mol]}$ ⁶⁹. For the lower crust, for simplicity, A is scaled from the upper crust value to be 5 orders of magnitude smaller and hence the resulting viscosity is 5 orders of magnitude higher given the same temperature. For the 2 km of upper mantle, we apply lab-constrained Newtonian rheology from ref.⁷⁰ where the equivalent $A = 0.0006 \text{ [MPa}^{-1}\text{s}^{-1}\text{]}$ (calculated from $2/3 \times 1e6 \times (1e4)^{-3} \times 1000$) and $Q = 339000 \text{ [J/mol]}$. For solidified magma,

we assume its A value to be 5 orders of magnitude larger and hence the resulting viscosity is 5 orders of magnitude lower than the mantle given the same temperature. To prevent numerical localizations of sill intrusion at a specific grid, $T(Z_{in})$ is approximated with an average temperature of the country rocks near Z_{in} within a thermal diffusion length during one numerical time step of 1 Kyr.

The initial vertical crustal temperature profile is taken to be piece-wise linear with the initial upper crustal thermal gradient $dT/dZ(0\sim 20 \text{ km}) = 40 [\text{K}/\text{km}]$ and lower crustal thermal gradient $dT/dZ(20\sim 40 \text{ km}) = 15 [\text{K}/\text{km}]$ (Fig. 3). The magma supply flux (Fig. 4a) is assumed with $F_m^0 = 15 [\text{cm}/\text{yr}]$, $t_0 = 170 [\text{kyrs}]$ and $c = 90\sqrt{2/\pi} [\text{kyrs}]$, $F_m^1 = 3 [\text{cm}/\text{yr}]$. Numerically, the heat equation 1 is discretized into a one-dimensional array of grids, and is solved by forward finite difference methods. We apply a semi-Lagrangian Crank-Nicolson algorithm⁷¹, which is coupled with one-half backward implicit step⁷² to damp the Crank-Nicolson error oscillations introduced by sharp temperature corners from sill intrusions. As noted above, the average effect of hydrothermal circulation is simulated by increasing the thermal diffusivity κ by a factor of Nu . The efficiency of hydrothermal circulation should scale with crustal permeability and thermal gradient. Hence it should depend on the existence of interconnected cracks as well as the crustal thermal condition. Upper crustal thermal gradient and fracture events should peak around the time when the magma flux $F_m(t)$ maximizes at t_0 . Hence, we assume $Nu = 25$ from the surface to 20 km when $t \geq t_0$ and $Nu = 1$ otherwise. Note that measurements from Yellowstone indicate up to 2000 mWm^{-2} of surface heat flux²², which is nearly 30 times of that of normal continental crust of 65 mWm^{-2} ⁶⁶.

We determine the magma eruptibility by whether the magma pressure head at the surface ($P_h(0) = \int_{Z_{in}}^0 (\rho_c - \rho_f)g dz$) is larger than the critical pressure (ΔP_c) for initiating an eruption when sourced from the intruding sill at depth Z_{in} :

$$P_h(0) > \Delta P_c \quad (17)$$

This is equivalent to considering whether the average density of the overburden of an intruding sill is larger than the density of fluid magma to an extent of equation 9. During the initial phases when the sill is deep or when the crust densifies due to sill intrusions, magma driving pressure at the surface $P_d(0)$ can be positive, which means magma from the Moho reservoir has the potential to erupt. However, we do not count major phase of flood basalts eruptibility when magma is sourced from the Moho reservoir during the early phase of an LIP emplacement because the pressure head should be consumed by lateral sill intrusions into the initial weaker and lower density crust before magma can reach the surface. We do not consider viscous resistances for sill or dike intrusions as they are negligible compared to the thermal arrest resistance from sill intrusions⁶⁷. We also neglect temporal variations in elastic overpressure from the magma reservoir which can be responsible for finer time scale hiatuses in magma eruptions^{25,26}.

We also include in the supplementary information with four videos of the multi-sill intrusion model that illustrate in detailed the changes in crustal density, temperature, pressures, viscosity and sill intrusion depths due to 420 Kyr (about half of the total model time) of sill intrusions. The model determined onset of major phase of flood basalt eruptions is at 408 Kyr. Video 1 shows the crustal densification process for comparison to the data in Fig. 2F. Video 2 presents the crustal temperature and pressures evolution. Note that for the assumed rheology parameters the thermal arrest resistance pressure has the dominate effect on controlling sill

intrusion depths when the sills are moving upwards into weak lower part of the upper crust, but the dike related stress change becomes important during the sill-deepening phase (starting ~175 Kyrs) as the sills open into stronger mafic intrusives. Video 3 shows the variations in temperature and viscosity structure resulted from the assumed lab-constrained rheological parameters. Video 4 includes changes in sill intrusion depth, temperature, magma overpressure, magma breakout pressure and magma overpressure if sourced from the intruding sill. With our model formulation, the intruding depth is determined by considering both the density structure and the thermo-mechanical conditions and hence is not always at the level of neutral buoyancy.

Data availability: For Fig. 1, global temperature change data are from ref. ⁷ (DOI: 10.1126/science.aay5055) and Deccan Trap extrusive flux data are converted from ref. ⁴ (DOI: 10.1126/science.aav1446). For Fig. 2, Seismic velocity data are converted from refs. ^{16,30}.

Code availability: All codes for our numerical calculations are available from X.T. upon request.

Appendix 3 References:

41. Zeebe, R. E. LOSCAR: Long-term Ocean-atmosphere-Sediment CArbon cycle Reservoir Model v2.0.4. *Geosci. Model Dev.* **5**, 149–166 (2012).
42. Solano, J. M. S., Jackson, M. D., Sparks, R. S. J., Blundy, J. D. & Annen, C. Melt Segregation in Deep Crustal Hot Zones: a Mechanism for Chemical Differentiation, Crustal Assimilation and the Formation of Evolved Magmas. *J. Petrol.* **53**, 1999–2026 (2012).
43. Chen, Y. & Morgan, W. J. A nonlinear rheology model for mid-ocean ridge axis topography. *J. Geophys. Res.* **95**, 17583 (1990).
44. Behn, M. D. & Ito, G. Magmatic and tectonic extension at mid-ocean ridges: 1. Controls on fault characteristics. *Geochemistry, Geophys. Geosystems* **9**, n/a-n/a (2008).
45. Kent, A. J. R. *et al.* Mantle heterogeneity during the formation of the North Atlantic Igneous Province: Constraints from trace element and Sr-Nd-Os-O isotope systematics of Baffin Island picrites. *Geochemistry, Geophys. Geosystems* **5**, n/a-n/a (2004).
46. Sobolev, A. V., Krivolutskaya, N. A. & Kuzmin, D. V. Petrology of the parental melts and mantle sources of Siberian trap magmatism. *Petrology* **17**, 253–286 (2009).
47. Hartley, M. E., MacLennan, J., Edmonds, M. & Thordarson, T. Reconstructing the deep CO₂ degassing behaviour of large basaltic fissure eruptions. *Earth Planet. Sci. Lett.* **393**, 120–131 (2014).
48. Henehan, M. J., Hull, P. M., Penman, D. E., Rae, J. W. B. & Schmidt, D. N. Biogeochemical significance of pelagic ecosystem function: an end-Cretaceous case study. *Philos. Trans. R. Soc. B Biol. Sci.* **371**, 20150510 (2016).
49. Rubin, A. M. Getting granite dikes out of the source region. *J. Geophys. Res. Solid Earth* **100**, 5911–5929 (1995).
50. Jellinek, A. M. & DePaolo, D. J. A model for the origin of large silicic magma chambers: Precursors of caldera-forming eruptions. *Bull. Volcanol.* **65**, 363–381 (2003).
51. Karakas, O., Degruyter, W., Bachmann, O. & Dufek, J. Lifetime and size of shallow magma bodies controlled by crustal-scale magmatism. *Nat. Geosci.* **10**, 446–450 (2017).
52. Dufek, J. & Bergantz, G. W. Lower Crustal Magma Genesis and Preservation: a Stochastic Framework for the Evaluation of Basalt–Crust Interaction. *J. Petrol.* **46**, 2167–2195 (2005).
53. Ryan, M. P. Neutral buoyancy and the mechanical evolution of magmatic system. *Magmat. Process Physicochem. Princ.* 259–287 (1987).
54. Menand, T. Physical controls and depth of emplacement of igneous bodies: A review.

Tectonophysics **500**, 11–19 (2011).

55. Rohrman, M. Intrusive large igneous provinces below sedimentary basins: An example from the Exmouth Plateau (NW Australia). *J. Geophys. Res. Solid Earth* **118**, 4477–4487 (2013).
56. Magee, C. *et al.* Lateral magma flow in mafic sill complexes. *Geosphere* **12**, 809–841 (2016).
57. Menand, T. The mechanics and dynamics of sills in layered elastic rocks and their implications for the growth of laccoliths and other igneous complexes. *Earth Planet. Sci. Lett.* **267**, 93–99 (2008).
58. Sili, G., Urbani, S. & Acocella, V. What Controls Sill Formation: An Overview From Analogue Models. *J. Geophys. Res. Solid Earth* **124**, 8205–8222 (2019).
59. Morgan, J. P. & Chen, Y. J. The genesis of oceanic crust: Magma injection, hydrothermal circulation, and crustal flow. *J. Geophys. Res.* **98**, 6283 (1993).
60. Gorczyk, W. & Vogt, K. Intrusion of Magmatic Bodies Into the Continental Crust: 3-D Numerical Models. *Tectonics* **37**, 705–723 (2018).
61. Parsons, T., Sleep, N. H. & Thompson, G. A. Host rock rheology controls on the emplacement of tabular intrusions: Implications for underplating of extending crust. *Tectonics* **11**, 1348–1356 (1992).
62. Buck, W. R. The role of magma in the development of the Afro-Arabian Rift System. *Geol. Soc. London, Spec. Publ.* **259**, 43–54 (2006).
63. Menand, T., Daniels, K. A. & Benghiat, P. Dyke propagation and sill formation in a compressive tectonic environment. *J. Geophys. Res.* **115**, B08201 (2010).
64. Spence, D. A. & Turcotte, D. L. Magma-driven propagation of cracks. *J. Geophys. Res. Solid Earth* **90**, 575–580 (1985).
65. Fialko, Y. A. & Rubin, A. M. Thermodynamics of lateral dike propagation: Implications for crustal accretion at slow spreading mid-ocean ridges. *J. Geophys. Res. Solid Earth* **103**, 2501–2514 (1998).
66. Turcotte, D. L. & Schubert, G. *Geodynamics*. (Cambridge University Press, 2002). doi:10.1017/CBO9780511807442
67. Lister, J. R. & Kerr, R. C. Fluid-mechanical models of crack propagation and their application to magma transport in dykes. *J. Geophys. Res.* **96**, 10049 (1991).
68. Carslaw, H. S. & Jaeger, J. C. *Conduction of Heat in Solids*. (Oxford University Press, 1959).
69. Wang, J. N., Hobbs, B. E., Ord, A., Shimamoto, T. & Toriumi, M. Newtonian Dislocation Creep in Quartzites: Implications for the Rheology of the Lower Crust. *Science (80-.).* **265**, 1204–1206 (1994).
70. Hirth, G. & Kohlstedt, D. Rheology of the upper mantle and the mantle wedge: A view from the experimentalists. *Geophys. Monogr. Ser.* **138**, 83–105 (2003).
71. Spiegelman, M. & Katz, R. F. A semi-Lagrangian Crank-Nicolson algorithm for the numerical solution of advection-diffusion problems. *Geochemistry, Geophys. Geosystems* **7**, (2006).
72. Britz, D., Østerby, O. & Strutwolf, J. Damping of Crank-Nicolson error oscillations. *Comput. Biol. Chem.* **27**, 253–263 (2003).

Acknowledgments: This work greatly benefited from discussions with Eunseo Choi, Jean-Arthur Olive, William Ryan, Suzanne Carbotte, Marc Spiegelman, Ching-Yao Lai, Bar Oryan, Elizabeth Fischer, Courtney Sprain, Tushar Mittal, Jennifer Kasbohm, Hernandez Nava and Benjamin Black. We also thank Richard Zeebe for sharing the LOSCAR code. This work is supported by NSF grants OCE-1654745.

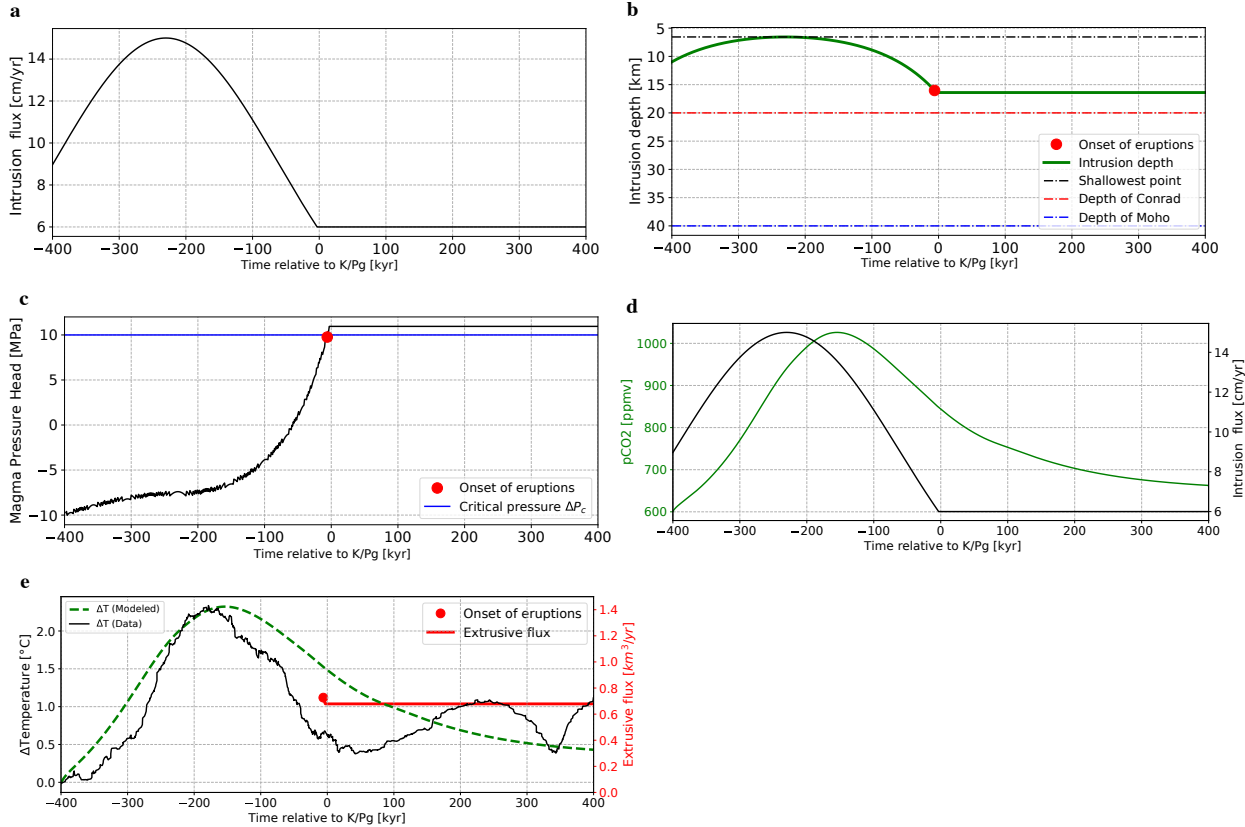
Author contributions: X.T., advised by W.R.B., conducted the model experiments and both authors wrote the manuscript.

Competing interests: Authors declare no competing interests.

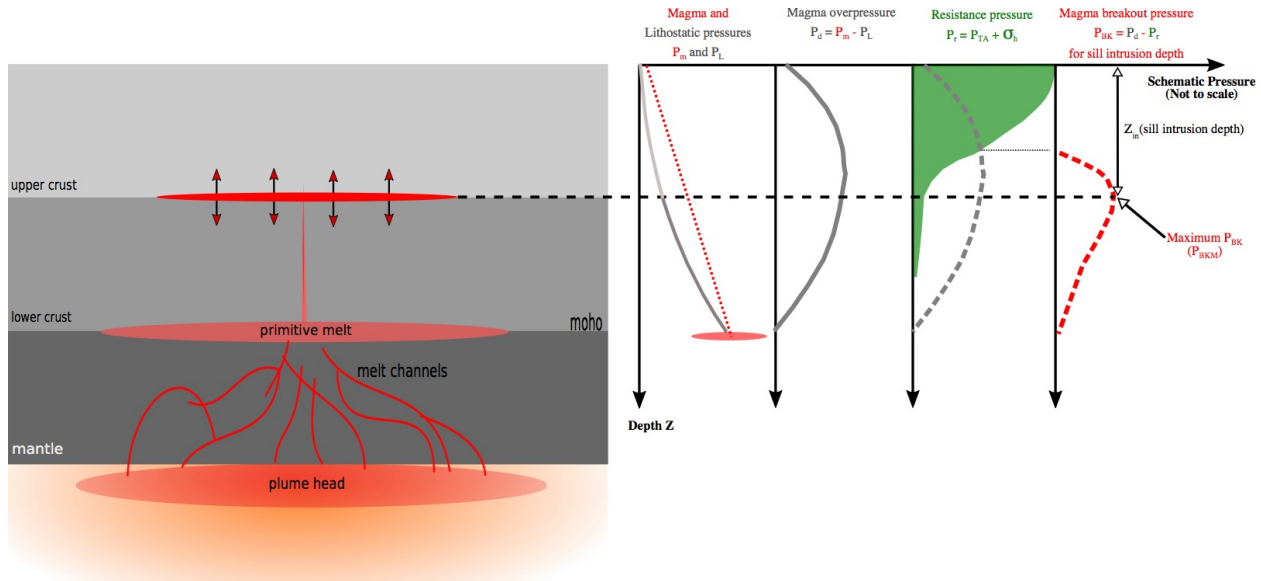
Additional information

Supplementary information of four videos is available for this paper.

Correspondence and requests for materials should be addressed to X. T. at email address: xtian@ldeo.columbia.edu.

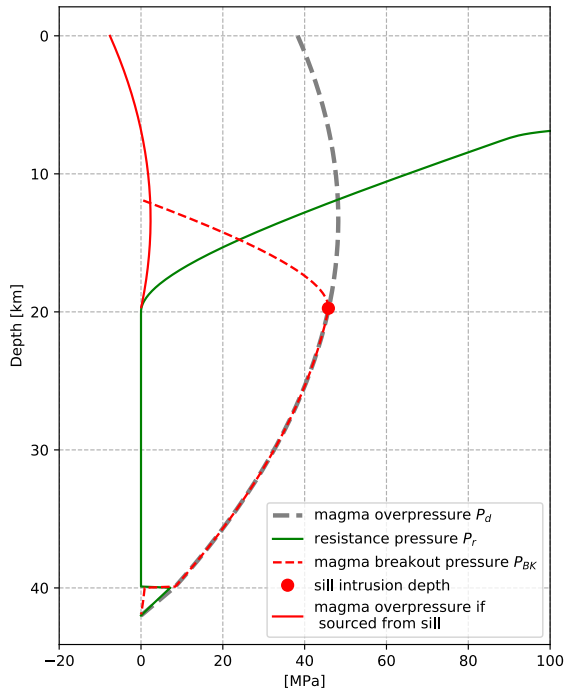


Extended Data Fig. 1 | Example of the steady-state analytic model results as functions of time relative to the Cretaceous-Paleogene (K/Pg) boundary. **a**, Assumed Gaussian sill opening flux in terms of magma volume flux per unit area of the sill. **b**, Sill intrusion depth for the melt flux of **(a)** and the thermal energy balance of equation (6). **c**, Magma pressure head at the surface sourced from the intruding sill. Magma eruption is possible when this pressure equals to the critical pressure ΔP_c at around K/Pg. For this case, magma flux from -400 kyrs to 0 kyrs is intruded. **d**, global averaged atmospheric CO₂ concentration with time predicted by the LOSCAR climate model. **e**, global temperature change predicted by the LOSCAR model along with the extrusive flux with time to compare with the observation in Fig. 1.



Extended Data Fig. 2 | Schematic illustrations for magma overpressure P_d , resistance pressure P_r and magma breakout pressure P_{BK} for determining sill intrusion depth Z_{in} .

Supplementary Information Video 1 | Video for modeled changes in crustal density due to evolving sill intrusions. Model time is shown at the upper left. Green line shows the extent and value of the averaged overburden density. Purple line shows the evolving crustal densities due to sill intrusions. The red dot indicates the sill intrusion depth and the magma density. The dashed grey line shows the initial crustal density profile.



Supplementary Information Video 2 | Video for modeled changes in temperature and pressures due to evolving sill intrusions. Model time is shown at the upper left. Left panel: temperature changes due to sill intrusions. The blue and red dashed lines indicate magma solidus and liquidus respectively. Right panel: changes in pressures due to sill intrusions (initial condition and legends are shown as the figure above: the dashed grey line is for the magma overpressure (driving pressure P_d). The green line is for the resistance pressure P_r . The dashed red line is for the magma breakout pressure P_{BK} . The solid red line is for the magma overpressure if sourced from the intruding sill. Red dots indicate depth of sill intrusions).

Supplementary Information Video 3 | Video for modeled changes in temperature and viscosity due to evolving sill intrusions. Model time is shown at the upper left. Left panel: temperature changes due to sill intrusions. The blue and red dashed lines indicate magma solidus and liquidus respectively. Right panel: the dashed grey line is for the initial viscosity. The solid line is for the evolving viscosity structure. Red dots indicate depth of sill intrusions.

Supplementary Information Video 4 | Video for modeled changes in sill depths, temperature and magma pressures due to evolving sill intrusions. Model time is shown at the lower left. Top panel: sill intrusion depth given the melt flux with time. Lower left panel: temperature changes due to sill intrusions. The blue and red dashed

lines indicate magma solidus and liquidus respectively. Lower right panel: the dashed grey line is for the magma overpressure (driving pressure P_d). The dashed red line is for the magma breakout pressure P_{BK} . The solid red line is for the magma overpressure if sourced from the intruding sill. Red dots indicate depth of sill intrusions.